AFOSR-TR- 84-1101

5

University of Illinois at Urbana-Champaign
Urbana, IL 61801

AD-A148 302

Department of Mechanical and Industrial Engineering
Technical Report UILU-ENG-84-4010

20000803179

ANALYSIS OF DEFLAGRATION TO DETONATION TRANSITION IN HIGH-ENERGY SOLID PROPELLANTS

Annual Technical Report

AFOSR Grant No. 81-0145

September 15, 1984

D

84 12 [illegible] 100

5

ANNUAL TECHNICAL REPORT

No. UILU-ENG-84-4010

For Research Supported by

AFOSR Grant No. 81-1045

-entitled-

ANALYSIS OF DEFLAGRATION TO DETONATION TRANSITION IN HIGH-ENERGY SOLID PROPELLANTS

prepared by

P. Barry Butler(1) and Herman Krier(2)

Department of Mechanical and Industrial Engineering
University of Illinois at Urbana-Champaign
144 MEB, 1206 W. Green St., Urbana, IL 61801

work supported by

Air Force Office of Scientific Research

Dr. Robert J. Barker, Program Manager

---

(1) Research Assistant

(2) Principal Investigator; Professor of Mechanical Engineering

UNCLASSIFIED

CURITY CLASSIFICATION OF THIS PAGE

REPORT DOCUMENTATION PAGE

a. REPORT SECURITY CLASSIFICATION: UNCLASSIFIED

1b. RESTRICTIVE MARKINGS: NONE

a. SECURITY CLASSIFICATION AUTHORITY:

3. DISTRIBUTION/AVAILABILITY OF REPORT: Approved for Public Release: Distribution Unlimited

b. DECLASSIFICATION/DOWNGRADING SCHEDULE:

. PERFORMING ORGANIZATION REPORT NUMBER(S): UILU-ENG-84-4010

5. MONITORING ORGANIZATION REPORT NUMBER(S): AFOSR-TR- 84-1101

a. NAME OF PERFORMING ORGANIZATION: University of Illinois

6b. OFFICE SYMBOL (If applicable): UIUC

7a. NAME OF MONITORING ORGANIZATION: Air Force Office of Scientific Research

c. ADDRESS (City, State and ZIP Code):
Department of Mechanical & Industrial Engr.
144 MEB; 1206 W. Green St.
Urbana, IL 61801

7b. ADDRESS (City, State and ZIP Code):
ATTN: Dr. R. J. Barker/NP
Bolling AFB, DC 20332

a. NAME OF FUNDING/SPONSORING ORGANIZATION: Air Force Office of Scientific Research

8b. OFFICE SYMBOL (If applicable): AFOSR

9. PROCUREMENT INSTRUMENT IDENTIFICATION NUMBER: Grant No. AFOSR-81-0145

c. ADDRESS (City, State and ZIP Code):
AFOSR/NP
Dr. Robert J. Barker
Bolling AFB, DC 20332

10. SOURCE OF FUNDING NOS.

PROGRAM ELEMENT NO.	PROJECT NO.	TASK NO.	WORK UNIT NO.
61102F	2301	A6	

1. TITLE (Include Security Classification) ANALYSIS OF DEFLAGRATION TO DETONATION TRANSITION IN HIGH-ENERGY Solid Propellants

2. PERSONAL AUTHOR(S): P. BARRY BUTLER and HERMAN KRIER

3a. TYPE OF REPORT: Interim Report

13b. TIME COVERED: FROM 8/30/82 TO 9/1/84

14. DATE OF REPORT (Yr., Mo., Day): September 1984

15. PAGE COUNT: 178

6. SUPPLEMENTARY NOTATION:

7. COSATI CODES

FIELD	GROUP	SUB. GR.

18. SUBJECT TERMS (Continue on reverse if necessary and identify by block number)
Deflagration to Detonation Transition (DDT)
Analysis of Shock Initiation
Porous Explosive DDT

9. ABSTRACT (Continue on reverse if necessary and identify by block number)

Increasing the nitramine content of solid rocket propellants increases the overall perormance of the system as well as the sensitivity to detonation by shock initiation. Under ertain circumstances Deflagration to Detonation Transition (DDT) can occur in high-energy olid propellant that has been granulated. The work presented in this report represents an ffort to analyze three distinct ways in which high-energy solid propellant can undergo a DDT. he emphasis of the research is on the transient events prior to the detonation as well as he steady state detonation conditions.

The system of partial differential equations describing one-dimensional, two-phase, eactive flow are solved by a Method of Lines (MOL) computer solution technique. Predictions or CJ properties, detonation run-up distance and detonation velocity compare favorably with xperimental data and predictions made using the TIGER chemical equilibrium computer code.

0. DISTRIBUTION/AVAILABILITY OF ABSTRACT
NCLASSIFIED/UNLIMITED ☒ SAME AS RPT. ☒ DTIC USERS ☐

21. ABSTRACT SECURITY CLASSIFICATION: UNCLASSIFIED

2a. NAME OF RESPONSIBLE INDIVIDUAL: Dr. Robert J. Barker

22b. TELEPHONE NUMBER (Include Area Code): 202-767-5011

22c. OFFICE SYMBOL: AFOSR/NP

D FORM 1473, 83 APR

EDITION OF 1 JAN 73 IS OBSOLETE.

UNCLASSIFIED

SECURITY CLASSIFICATION OF THIS PAGE

ABSTRACT

Increasing the nitramine content of solid rocket propellants increases the overall performance of the system as well as the sensitivity to detonation by shock initiation. Under certain circumstances Deflagration to Detonation Transition (DDT) can occur in high-energy solid propellant that has been granulated. The work presented in this report represents an effort to analyze three distinct ways in which high-energy solid propellant can undergo a DDT. The emphasis of the research is on the transient events prior to the detonation as well as the steady state detonation conditions.

The system of partial differential equations describing one-dimensional, two-phase, reactive flow are solved by a Method of Lines (MOL) computer solution technique. Predictions for CJ properties, detonation run-up distance and detonation velocity compare favorably with experimental data and predictions made using the TIGER chemical equilibrium computer code. [illegible]

TABLE OF CONTENTS

CHAPTER 1 page

SHOCK PHYSICS AS APPLIED TO REACTIVE SOLIDS:A REVIEW

CHAPTER 2

LITERATURE REVIEW: EXPERIMENTS AND ANALYSIS

CHAPTER 3

THE MODEL

CHAPTER 4

NUMERICAL SOLUTION TECHNIQUE

CHAPTER 5
RESULTS

CHAPTER 6
SUMMARY, CONCLUSIONS AND RECOMMENDATIONS

LIST OF SYMBOLS

$\bar{a}$	Helmholtz free energy
a'	constant in Eq. (1.1a)
a	void porosity (V_T/V_p)
A_b	surface area
b	constant in Eq. (1.1a)
$\bar{c}$	constant in Eq. (4.9)
c	sound velocity
C_v	specific heat at constant volume
d	grain diameter
D	detonation velocity
$\mathcal{D}$	interphase viscous force
e	specific internal energy
E	total energy
E_c	critical initiation energy (Fig. 2.8)
E_{ch}	chemical energy
$\bar{E}$	energy source term
$F(\bar{V})$	flux vector in conservation equations
G	solid to gas decomposition rate
$\bar{G}(v)$	Gruneisen coefficient
G'	shear modulus
G	interphase mass transfer
h	enthalpy
I_{sp}	specific impulse
kE	kinetic energy
k_g	gas thermal conductivity

L	bed total length
ℓ_{CJ}	detonation run-up distance
m	mass
n	burning rate index
n'	covolume
M	molecular weight
Pr	Prandtl number
P	pressure
p^e	equilibrium stress
q	viscous pressure
$\dot{Q}$	interphase heat transfer
$\bar{r}$	radiative heat transfer
r	density
R	gas constant
$\hat{R}$	universal gas constant
Re	Reynolds number
s	entropy
$\bar{S}$	source vector in governing equations
T	temperature
t^*	hot spot delay time
t	time
t_{CJ}	detonation run-up time
T_H	hot spot temperature
$\bar{t}$	shock duration
u	fluid velocity
U_s	shock velocity
v	specific volume

V	volume
V'	flyer-plate impact velocity (Fig. 2.8)
W	deflagration velocity
W_H	hot spot volume fraction
x	distance
$\bar{x}$	distance from interface (Fig. 1.5)
$\hat{x}$	grain dimension
Y	yield strength
γ	isentrope logarithmic slope
$\phi_i(v_i/v_T)$	porosity (i=g, gas; i=p, solid)
μ_g	gas viscosity

Subscripts

o	initial
oo	porous initial
1	gas partial phase
2	solid partial phase
CJ	Chapman Jouguet state
g	gas
i	irreversible process
p	solid
m	mixture
s	isentrope
T	total
w	piston

CHAPTER 1

SHOCK PHYSICS AS APPLIED TO REACTIVE SOLIDS: A REVIEW

1.1 Introduction

The probability of a detonation occurring in a solid propellant rocket motor greatly increases when secondary high-explosives (HE) are used as constituents in the propellant mixture. Octogen (HMX) and Cyclotrimethylene trinitramine (RDX) are the most commonly used nitramine HE in today's propellant formulations. Increasing the explosive content of solid propellant increases both the overall performance of the system and the sensitivity to detonation by shock initiation.

The work presented in this report represents an effort to analyze the transient events leading to a detonation in a region of granulated high-energy propellant. A review of pertinent literature is also included. The final results represent an important extension of research done earlier by Butler, Krier and Lembeck [1] on detonation hazards in damaged, HMX-based solid propellants. The system of coupled partial differential equations describing the one-dimensional, two-phase reactive flow in the granulated bed will be presented in Chapter 3, along with a finite difference numerical technique used to solve them. An entropy analysis will be presented in order to verify that the two-phase flow equations presented satisfy the Second Law of Thermodynamics.

In addition to the governing equations, constitutive relations are presented which describe the states of the unreacted solid and gaseous products. A Helmholtz free energy function will be introduced to define the state of the solid phase and a nonideal covolume equation of state will be used for the high density product gases.

A key contribution herein is the development of an appropriate numerical scheme needed to solve the system of nonlinear partial differential equations. Results from the computer code are presented in Chapter 5. They illustrate how the initial and boundary conditions, as well as the propellant properties, affect the detonation transition process. Whenever possible, these results are compared with experimental data. The remainder of Chapter 1 is devoted to a review of solid propellant rocket performance, shock waves, detonation waves and hazard assessment.

1.2 Performance of Solid Propellant Rocket Motors

Most of today's chemical rocket propulsion systems fall into one of two general categories, liquid or solid. Thrust is produced in the liquid system by mixing and burning liquid fuel (i.e. liquid hydrogen) and liquid oxidizer (i.e. liquid oxygen) in a high pressure combustion chamber and expanding the resulting combustion products in a converging-diverging nozzle. On the other hand, solid propellant propulsion systems contain both fuel and oxidizer in a precast solid grain which is consumed as a surface burning combustion wave propagates through it. An example of a typical composite double-base propellant is ammonium perchlorate crystals and powdered aluminum held together by a nitrocellulose- nitroglycerin double-base grain (DB/AP/Al). Here, the ammonium perchlorate (AP) acts as an oxidizer and the powdered aluminum (Al) is an energy- releasing fuel. Both fuel and oxidizer are found in each of the double-base components (DB), nitrocellulose and nitroglycerin. Since the early 1970's both the Air Force and Navy have researched and tested solid propellant formulations containing secondary explosives such as RDX and HMX in order to increase the energy content per unit mass of the propellant. Some formulations include up to 10% HE by mass. As will be discussed briefly, a detonation hazard exists when burning these high-energy propellants, which is generally not present during the combustion of less energetic composite and composite-double base propellants.

For most precast solid propellants at rocket motor pressures (1 to 7 MPa) a simplified expression for the steady-state burning rate at which the combustion wave propagates through the reactants is

$$d\hat{x}/dt = a' + bP \qquad (1.1a)$$

where 'a'', 'b' and 'n' are empirical constants. In Eq. (1.1a) the variable P represents the pressure of the product gases adjacent to the burning surface. As an example, the composite double-base DB/AP/Al propellant discussed above regresses at a constant rate of $d\hat{x}/dt = 2.00$ cm/sec at $T = 293$ K and $P = 6.8$ MPa [2]. The mass of gas generated per unit time is the product

$$dm/dt = (d\hat{x}/dt)r_p A_b \qquad (1.1b)$$

where, r_p is the propellant density and A_b is the burning surface area. Unfortunately, the local mass generation rate can be increased orders of magnitude if A_b increases as a result of propellant fragmentation. The work presented in this report will examine one of the hazards associated with solid propellant combustion. The hazard is Deflagration to Detonation Transition (DDT). The term 'Deflagration' refers to the subsonic combustion mode $(d\hat{x}/dt)$ while the term 'Detonation' refers to a self-sustaining supersonic reaction wave with peak pressures ranging from 10 GPa to 50 GPa.

The performance of a modern day solid propellant rocket motor is usually predictable. A desired thrust-time profile can be obtained by fixing the rate of product gas generation in the motor combustion chamber. One way to accomplish this is to cast the propellant grain to have a desired surface area as a function of 'burn time'. Burn time is defined as the time elapsed since complete ignition of the propellant grain. For example, by burning a stick of propellant in a rocket motor in a cigar-like fashion along the axial direction, the burning surface area and thrust are constant with time. Likewise, if the propellant is cast so that the surface area increases with burn time (i.e. annular configuration, center burning), the thrust will increase with time. Other ways to change the product gas generation rate include: changing the chemical composition of the propellant and adding burn inhibitors to the propellant surface.

One major design objective of the rocket engineer is to increase the specific impulse, I_{sp} of the system. The specific impulse represents the ratio of thrust to fuel mass flow-rate and has units of seconds. This one parameter is most representitive of the overall rocket performance. An increase in I_{sp} implies more thrust for the same mass flow rate or a reduced mass flow-rate for the same thrust. Chemical propulsion systems typically have values of specific impulse ranging from 200-400 seconds with most solid propellants in the 180-270 second range. Table 1.1, taken from the text by Sutton and Ross [2], lists specific impulse, flame temperature, propellant density and burning rate data for a few composite, double-base and composite double-base solid propellants.

To increase the specific impulse of a solid propellant rocket motor which has a fixed area-ratio nozzle, one can either increase the design operating pressure or burn more energetic propellant constituents. It is well known that there are severe penalties if one elects the first option and designs the propulsion system to allow for an increased chamber (and combustion) pressure. One of these is the necessity for a more massive motor wall, a weight increase that reduces the vehicle mass ratio. In addition, since the heat transfer to the nozzle surface increases (almost

Table 1.1. Characteristics of Some Operational Propellants [2]

Propellant Type	I_{sp} Range (sec)	Flame Temperature (°F)	Flame Temperature (°K)	Density (g/cc)	Burning Rate (cm/sec)
DB	220-230	4100	2533	1.606	1.14
DB/AP/Al	260-265	6500	3867	1.760	1.98
DB/AP-HMX/Al	265-270	6700	3978	1.760	1.40
CTPB/AP/Al	260-265	5600-5800	3367-3478	1.733	1.14
HTPB/AP/Al	260-265	5600-5800	3367-3478	1.814	1.02

Acroynms and symbols:

Al, aluminum
AP, ammonium perchlorate
CTPB, carboxy-terminated polybutadiene
DB, double base
HMX, cyclotetramethylene tetranitramine
HTPB, hydroxy-terminated polybutadiene

linearly) with the operating pressure, a more effective nozzle wall cooling system would have to be included.

By burning more energetic propellant constituents such as the secondary nitramine explosives RDX and HMX, the specific impulse and thus overall performance of a solid rocket motor can be increased. However, one disadvantage which comes with using these explosive-based propellant mixtures is the hazard of Deflagration to Shock to Detonation Transition (DSDT). As mentioned, a DSDT event occurs when a controlled subsonic deflagration wave makes a transition to a high order detonation. The result is total destruction of the motor assembly.

In the literature reviewed in the following chapter this process in more commonly referred to as Deflagration to Detonation Transition (DDT). Our research group at Illinois coined the description DSDT in order to emphasize that Shock to Detonation Transition (SDT) is the final step in the process. Both terms, DDT and DSDT, will be used interchangeably throughout the text. SDT will be discussed further in Section 1.5.

Needless to say, basic research is needed in order to better understand and mitigate the DDT hazard in high-performance solid propellant rocket motors. At the present time there is an active group in the United States, organized by the JANNAF Subcommittee on Propulsion Hazards, which attempts to standardize DSDT testing procedures used by suppliers of the high-energy propellants. One such test is the shotgun/relative quickness test where a propellant sample is shock impacted in order to determine the amount and size of the resulting fragments, two very important parameters in the study of DSDT [18]. In addition to the DSDT testing carried out by the propellant suppliers and users, several of the national laboratories (Sandia [3], Los Alamos [4,5]) and service laboratories (Naval Surface Weapons Center (NSWC) [6-8], Naval Weapons Center (NWC) [9]) are conducting related experiments on DSDT. These will be discussed in Chapter 2.

In conjunction with the experimental work mentioned, analysis and numerical modeling of DSDT was begun almost ten years ago at the University of Illinois under the direction of Professor Herman Krier [10-14]. Since then the work has been expanded on by groups at Sandia National Laboratories [15,16], NWC [17] and NSWC [18]. In the early 1970's pioneering two-phase reactive flow modeling was carried out by Kuo and Summerfield [19], Gough [20] and by Kuo et al. [21].

1.3 DSDT in Granulated Solid Propellant

In the literature cited here (and in Chapter 2), three different flow processes can be identified as being DDT (DSDT). Two are real possibilities in the rocket motor environment and the third is only possible when using high-explosive under extreme confinement. It is unlikely that a solid rocket motor would be cast with pure explosive. However, studying the third event provides basic information on detonation initiation mechanisms.

This section has been included in order to differentiate between the three cases and provide the reader with a basic understanding of the sequence of events leading to detonation in each of them.

What will be referred to as DDT-Case 1 involves a transition to detonation occurring within a bed of granulated propellent. Consider the rocket motor shown in Fig. 1.1 . For illustration purposes, a center-burning configuration is shown. It is hypothesized that the normal burning process of the cast solid propellant in the rocket motor is disturbed by an abnormality such as a crack (see Fig. 1.1) in the propellant grain [1,22], thus providing the granulated region. Figure 1.2 shows an enlargement of the granulated region. The fracture could be the result of a handling accident during shipment or nozzle failure during operation. Because of the increased surface-to-volume ratio of the resulting fragments, product gas generation increases beyond the level necessary for steady-state motor operation. Pressure gradients, developed as a result of localized burning, drive the hot product gases into the cracks developed in the propellant ahead of the ignition front. As a consequence of this unsteady flow process, convective heat transfer from the hot product gases to the unreacted solid propellant will ignite additional propellant particles. Under certain circumstances this process can accelerate. For example, as the propellant decomposes, the pressure wave strengthens, leading to the ignition of more propellant. This accelerated convective burning can eventually lead to shock compression of the upstream propellant and a possible detonation transition. This is illustrated in Fig. 1.3

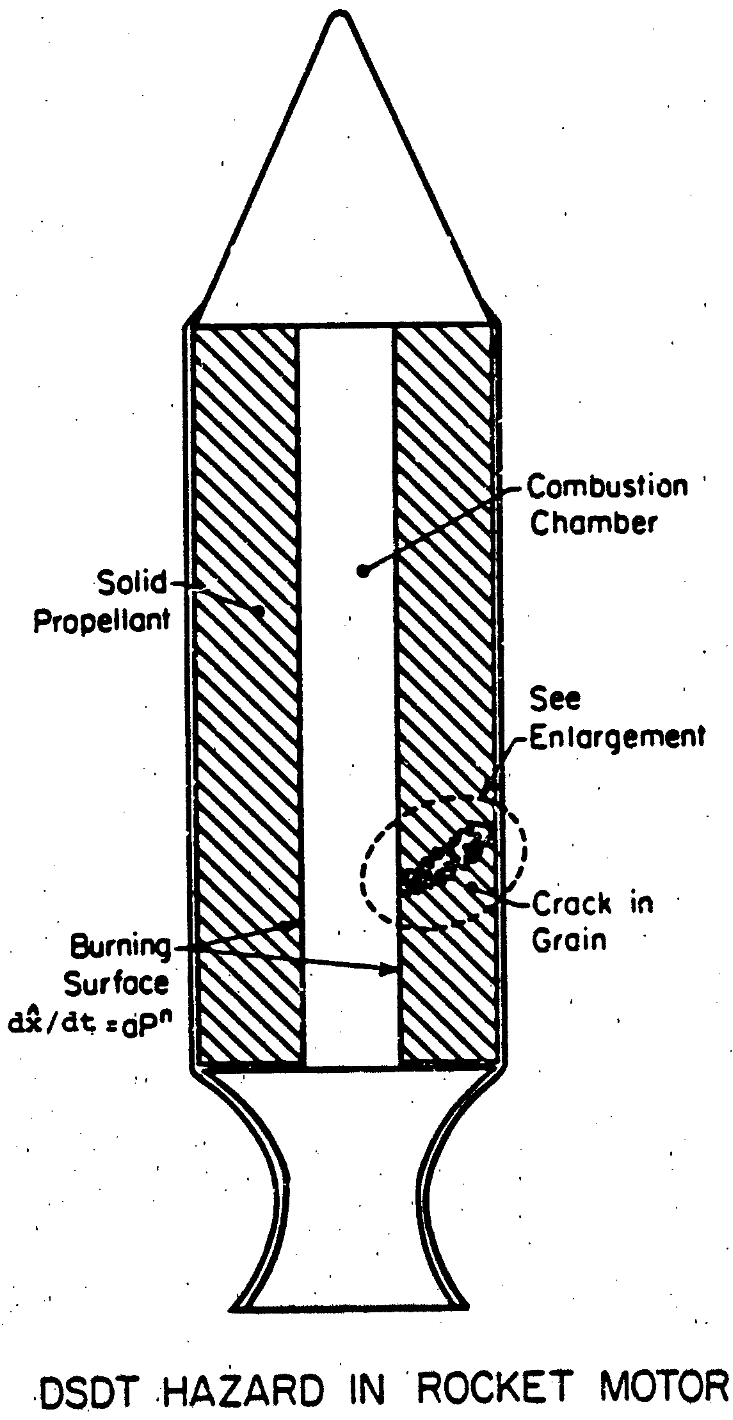

Fig. 1.1 Sketch of solid propellant rocket motor with crack in grain

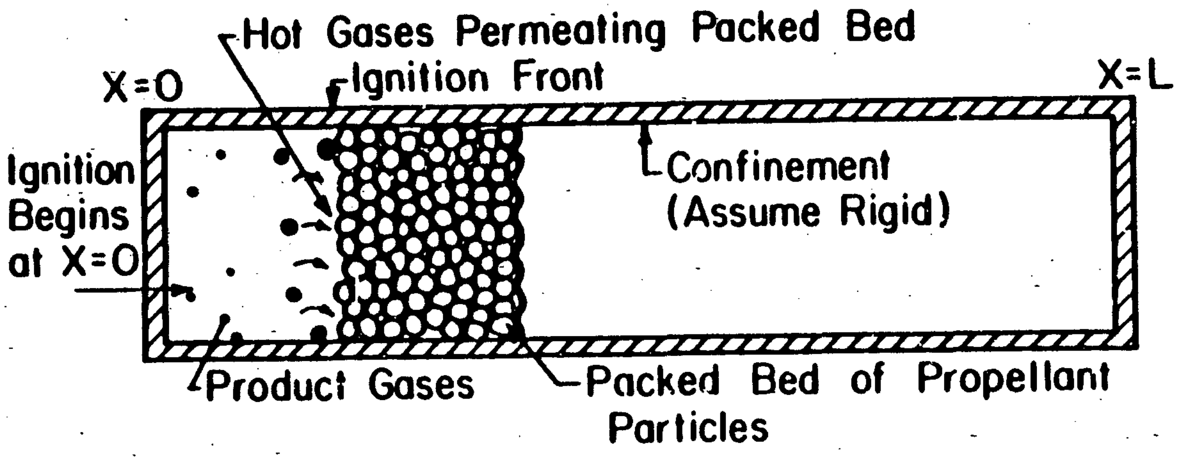

DSDT IN PACKED BED

Fig. 1.2 Enlargement of granulated bed formed in rocket motor (see Fig. 1.1) Black dots represent reacting particles.

[7], a typical x-t locus of the convective ignition front and subsequent detonation front.

Figure 1.4 illustrates the general form of a pressure profile (P,x) once the steady state detonation solution is obtained. For illustrative purposes, the profile is superimposed on a sketch of a granulated bed. The shock front is followed by a narrow reaction zone (not to scale in Fig. 1.4) which is followed by an expansion zone consisting of 100% product gases. More details of the detonation wave structure will be presented in the following sections.

A second DDT scenario, DDT-Case 2, involves a region of granulated propellant providing the impetus to shock initiate an adjacent region of cast propellant. This is illustrated in Fig. 1.5 . The cast material (Zone 1) can contain 'blind' pores, but is assumed to be impermeable to the flow of hot gases from the granular zone (Zone 2). This implies that, unlike the first DDT scenario discussed, only stress waves can be transmitted upstream of the reaction zone. A second characteristic of Case 2 is that the length of the granular bed is <u>less</u> than the detonation run-up length. The important point here is that although the granular bed is shorter than the critical detonation run-up length, the adjacent material can still detonate. DDT-Case 2 was studied in detail by Cudak, Krier and Butler [14].

In both DSDT processes described above, the transition to detonation is the result of rapid gas generation caused by

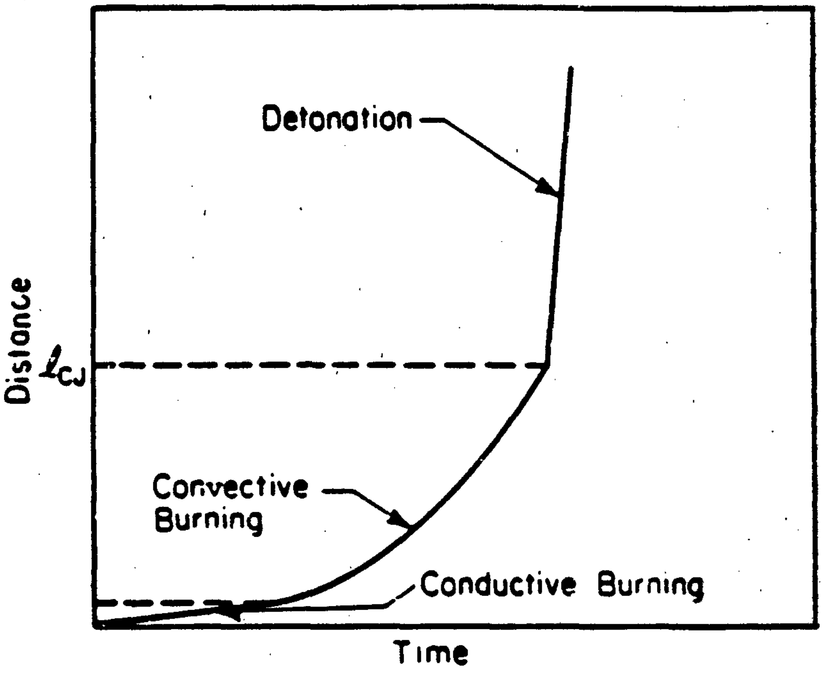

Fig. 1.3 Typical ignition front (x,t) locus showing conductive burning, convective burning and detonation regimes. 'ℓ_{CJ}' is the detonation run-up distance.

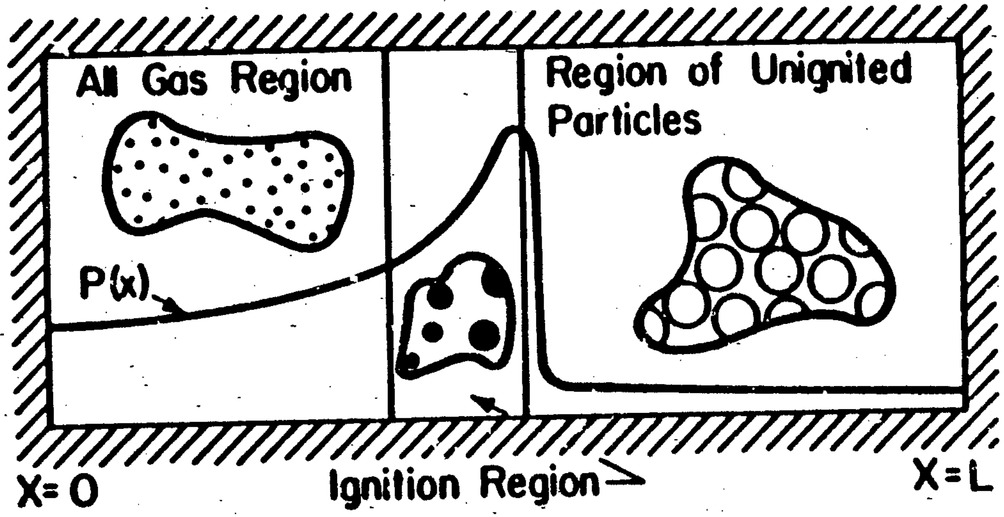

Figure 1.4 Schematic of a granular bed after making a transition to detonation. Ignition region has collapsed to a thin zone and is followed by an all-gas expansion zone.

convective burning in a packed bed of reactive particles. In Case 1 the detonation transition occurs within the granulated bed and, in Case 2, the detonation occurs in either a voidless cast material or cast material with blind pores upstream of the granulated bed. Nevertheless, in both cases the rapid pressurization rate due to the reacting, fragmented bed provides the driving force necessary to shock initiate the material upstream.

The third type of DDT discussed in the literature, DDT-Case 3, results from end-burning (conductive combustion) a confined cast explosive (Fig. 1.6) which is impermeable to the flow of hot product gases. Although the manner in which the deflagration wave traverses the explosive is different from the first two cases, the end result (steady detonation wave) is the same.

Macek [23] was the first to do experimental and analytical research on DDT in <u>cast</u> secondary explosives. He showed how the pressure rise due to the end-burning of a confined explosive propagated stress waves through the upstream solid material which eventually coalesced into a shock wave. The shock formation was predicted to occur at the approximate location of the transition to detonation observed in similar experimental work. Figure 1.6 is an illustration of the test configuration used in this type of DDT experiment. Here, the region labeled 'Zone 2' is a cast, voidless explosive and 'Zone 1' is occuppied by the product gases generated in the propellant combustion.

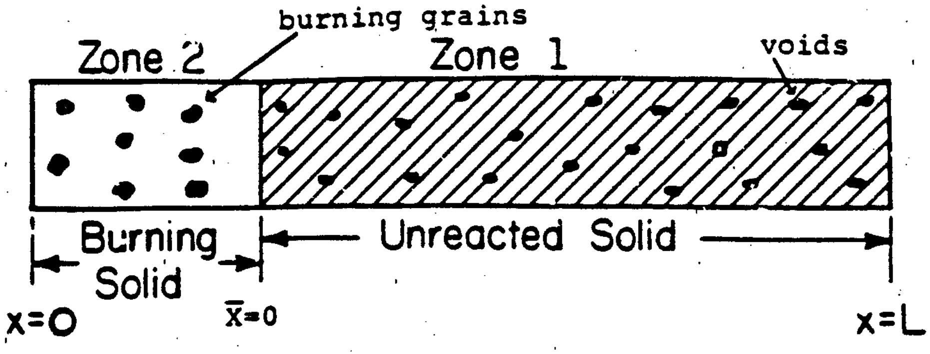

Fig. 1.5 Schematic of DDT-Case 2 configuration.

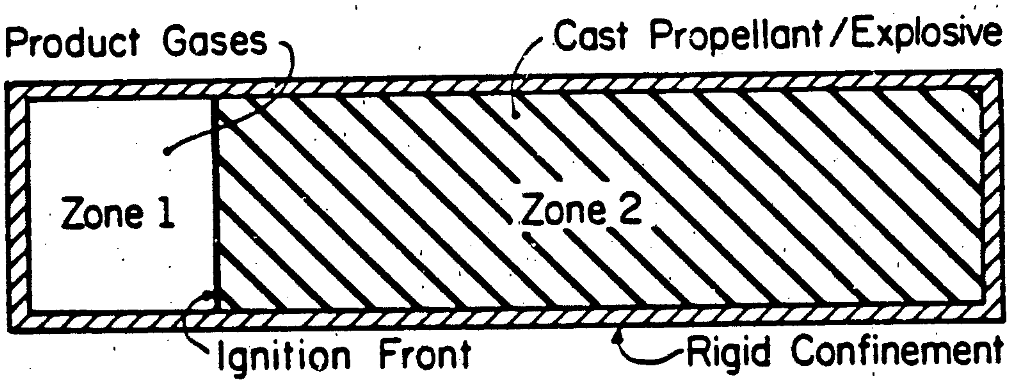

Fig. 1.6 Schematic of DDT-Case 3 configuration.

The sequence of events for this DDT process begins with the thermal ignition of the explosive at the location $\bar{x}=0$. This is then followed by the pressurization of the gas volume (Zone 1), increased regression rate ($d\hat{x}/dt$) of the burning material, stressing of the unreacted solid, shock formation ahead of the ignition front and eventual transition to detonation near the location of the upstream shock formation. The driving force provided by the confined gases in Zone 1 is analogous to a moving piston with a prescribed velocity-time profile acting on the $\bar{x}=0$ boundary, continually increasing the stress level in Zone 2. Although Case 3 has been shown to be a viable method for obtaining DDT in cast explosives , it will not cause DDT in cast propellants [22]. Very simply, conductive combustion of the propellant alone will not provide a rapid enough pressure-rise rate to shock initiate cast propellant.

1.4 Detonation Waves in Condensed Explosive (A Review) *

The material to be introduced later in this report will deal with detonation waves traveling through highly energetic granular propellants and explosives. Before one attempts to analyze this complex two-phase flow process, a review of nonreactive shock waves and detonation waves in simple homogeneous materials will be helpful. The detonation model presented in this section is one-dimensional and assumes

(1) Transport processes are neglected.

---

* See Reference 24

(2) The detonation wave is one-dimensional planar.

(3) A single irreversible reaction occurs.

(4) The reaction takes place almost instantaneously.

(5) The products of reaction are in thermochemical equilibrium.

Detonation waves should not be discussed without first introducing simple shock wave theory for nonreactive materials.

Begin by considering the classical [26,27] piston-cylinder arrangement illustrated in Fig. 1.7 . Here, a compressible substance is contained within a semi-infinite cylinder which is bounded on one end by a frictionless piston. Assume that the entire process is one-dimensional and that the motion of the piston can be modeled as small incremental velocities.

In Fig 1.7a , the piston is shown to be at rest, $u_w = 0$ at time t_o . At some later time, t_1 (Fig. 1.7b) , the piston is impulsively started and moving with a velocity, $u_w = u_1$, into the undisturbed medium. The movement of the piston in the +x direction over the time interval $t_o \rightarrow t_1$ results in compression of the material adjacent to the piston face. The conservation of mass and momentum dictate that the stress wave will propagate upstream with a velocity c_o into the undisturbed medium where c_o represents the sound velocity in the material ahead of the stress wave.

If the piston shown in Fig. 1.7c now moves with velocity $u_2 >$

u_1 over the time period $t_1 \rightarrow t_2$, a second stress wave with velocity c_1 will be propagated into the already stressed material. The value of c_1 is greater than c_o since the material we are describing is assumed to be a simple compressible substance and therefore has an increase in sound velocity with an increase in stress. Thus, the wave propagation velocity (c_i, $i = 1,2,\ldots$) increases with each successive wave when the piston is accelerating. The net result is coalescence of the stress waves into a shock wave. This is shown in Fig. 1.7c. In order for the shock wave developed by the piston to propagate through the undisturbed material at a constant shock velocity, the velocity of the piston must also remain constant. This will become evident after the conservation equations are introduced later in this section. It should be noted that dissipative effects will keep the shock front slope, dP/dx from approaching infinity in an actual shock.

Up to now we have referred to stress waves as discrete entities occurring over finite time increments. This was done in order to simplify the discussion presented on stress wave propagation and shock wave formation in the piston-cylinder arrangement. In reality, the stress-time piston input function discussed is most likely a continuous process. However, if the time increments are made small enough and enough discrete stress waves are analyzed, a thorough understanding of stress wave coalescence can be gained by graphical techniques.

As an example, Fig. 1.8a [28] shows a plot of constant stress

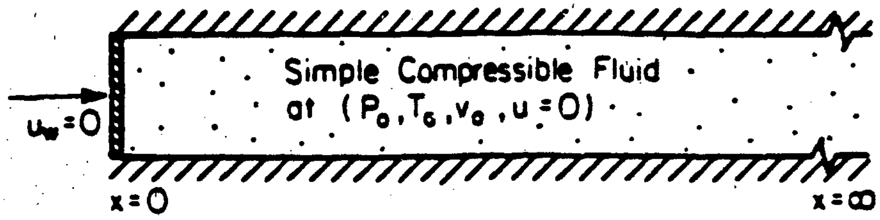

Fig. 1.7a Piston-cylinder arrangement at time t_o.

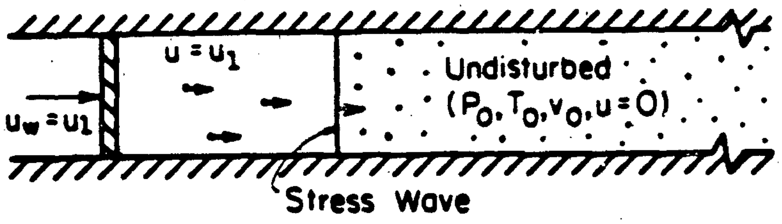

Fig. 1.7b Piston-cylinder arrangement at time t_1 illustrating stress wave propagation into undisturbed fluid.

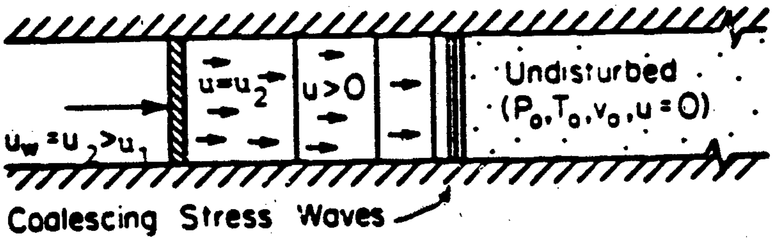

Fig. 1.7c Piston-cylinder arrangement at time t_2 illustrating stress wave coalescence into shock wave.

lines (characteristics) in x-location, time (x, t) space. The piston was accelerated in an exponential manner, beginning with $u = 0$ at $t = 0$. The material is HMX. For this particular case, the characteristics are shown to coalesce at approximately $x = 15$cm. The accompanying figure, Fig. 1.8b, shows the pressure, x-location profiles for the same times. By comparing the two figures, one can see how the coalescence of the characteristics in (x,t) space (Fig. 1.8a) corresponds to a $dP/dx \rightarrow \infty$ in (P,x) space (Fig. 1.8b).

Now consider a shock wave moving into a material at rest. This is illustrated in Fig. 1.9a. The shock wave is shown moving at a velocity D into the undisturbed material which has thermodynamic properties P_A, v_A and e_A. Here, P_A represents pressure, v_A represents specific volume and e_A the internal energy of the material at rest. The material is also shown to have a velocity, $u_A = 0$. The shocked state downstream of the shock front is described by the state variables P_B, v_B and e_B in addition to the dynamic variable, $u_B = u$. From a coordinate system fixed to the moving shock wave, an observer located at the origin would see the undisturbed material moving with velocity $u_A = D$ into the stationary reaction zone and the products of combustion exiting with velocity $u_B = (D - u)$. This is illustrated in Fig. 1.9b. The thermodynamic variables (P,v,e) are independent of the reference configuration and would therefore not be altered. Recall from the previous section that in order for the shock wave to be steady state, the downstream velocity, u_B in this case, must also be a constant with time.

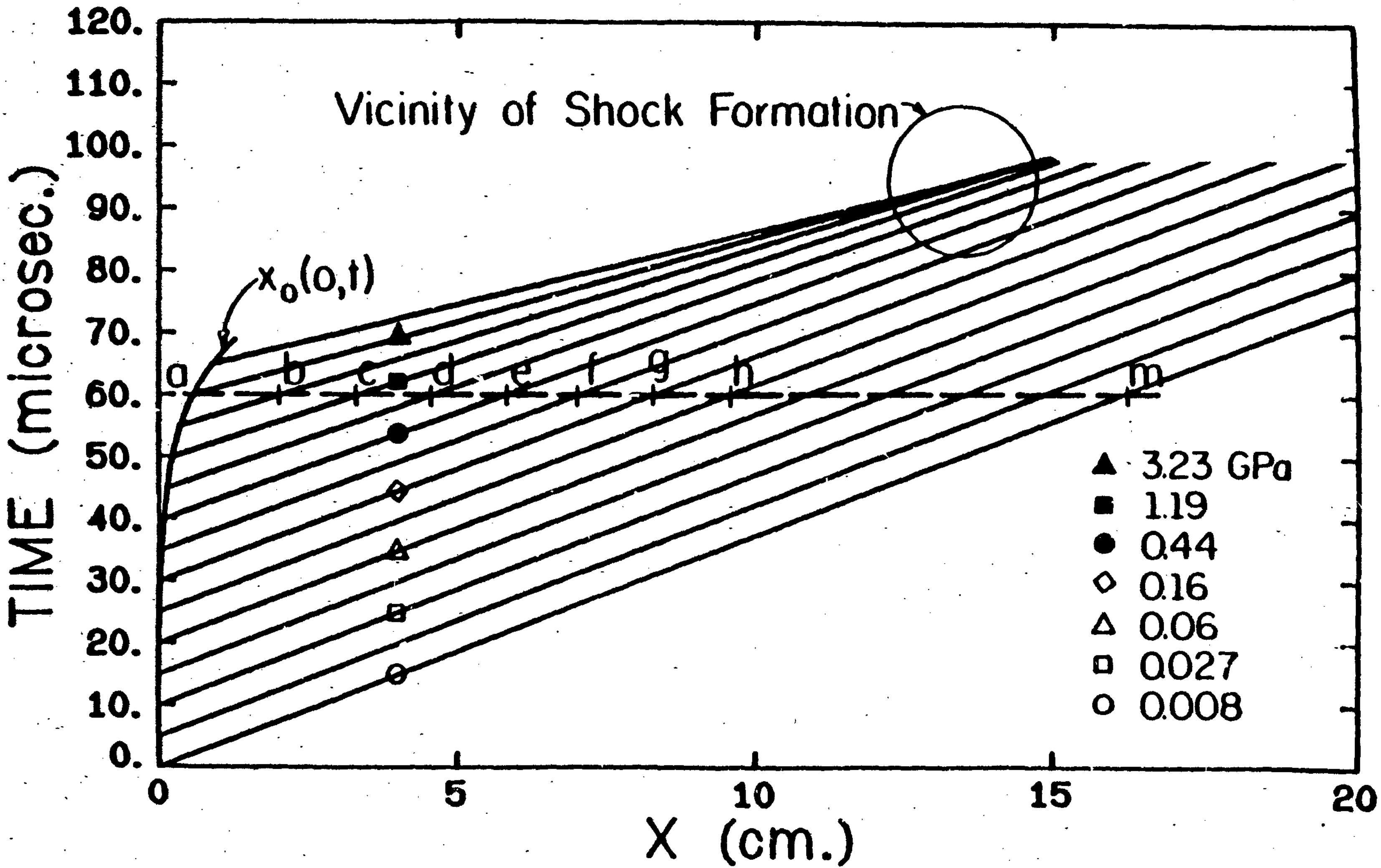

Fig. 1.8a Lines of constant stress in homogeneous material (HMX) being stressed at x=0.

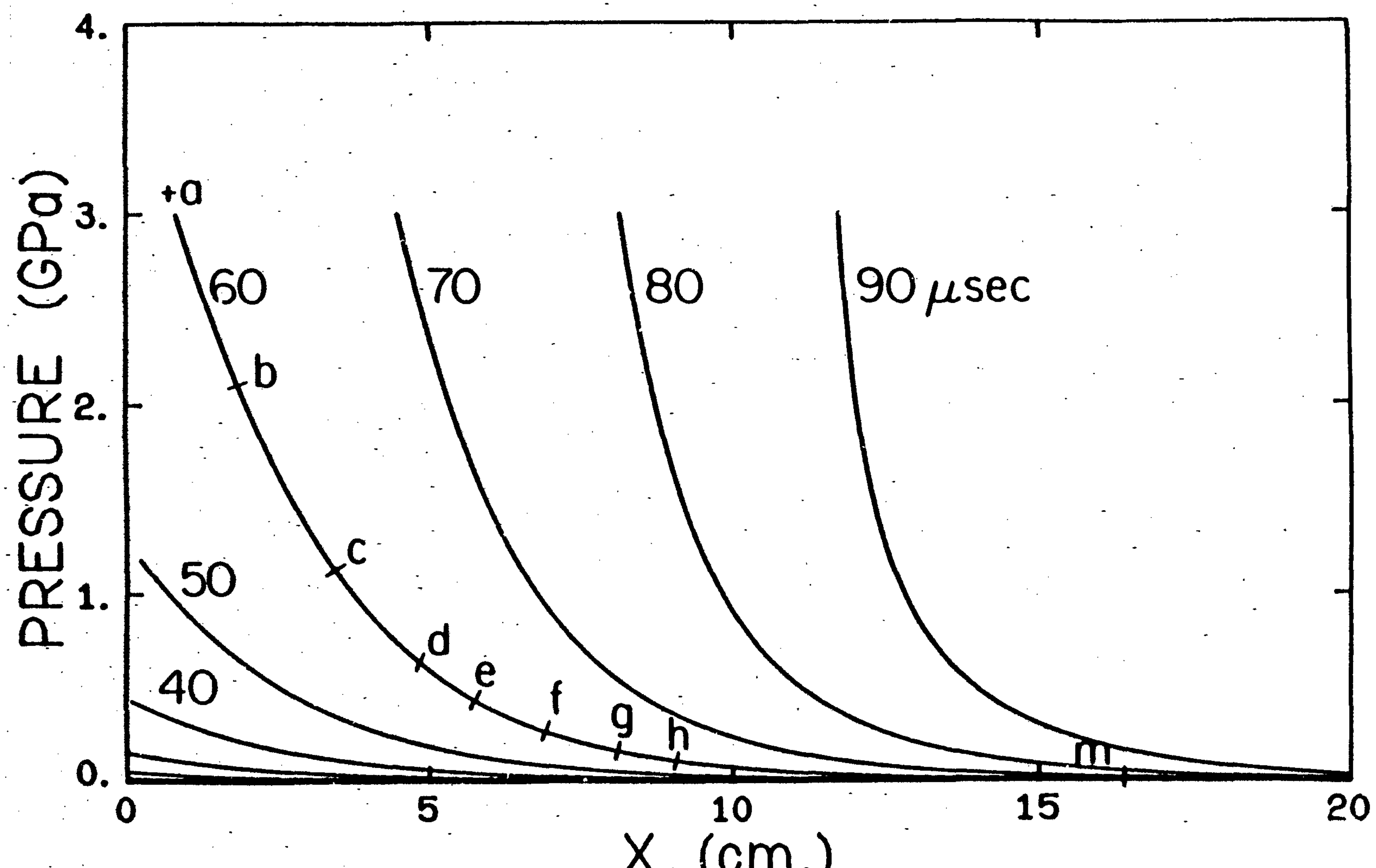

Fig. 1.8b Pressure, x-location profiles for Fig. 1.8a.

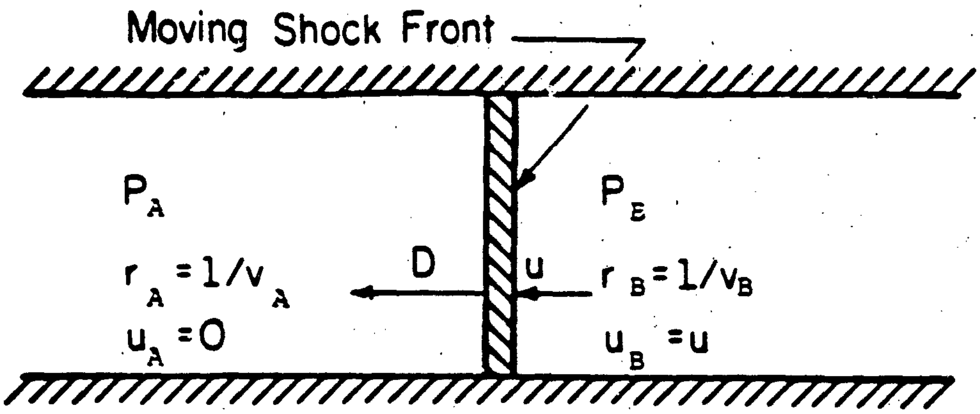

Fig. 1.9a Shock wave propagating into stationary fluid (Reference frame is fixed).

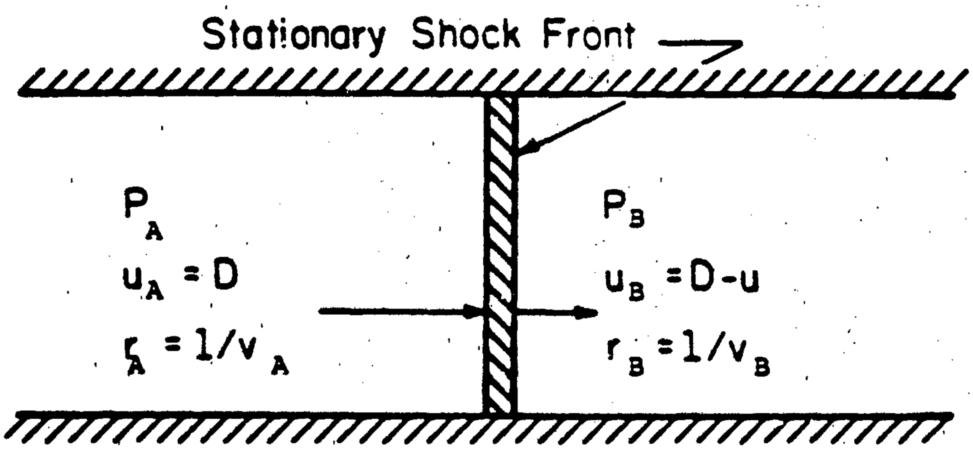

Fig. 1.9b Shock wave in fixed coordinate system.

Conservation of mass and momentum through the flow area shown in Fig. 1.9 gives respectively

$$r_A D = r_B u_B = r_B \, (D-u) \tag{1.2}$$

and

$$r_A D^2 + P_A = r_B u_B^2 + P_B = r_B \, (D-u)^2 + P_B \tag{1.3}$$

The expression for conservation of momentum (Eq. 1.3) can be further simplified by making use of Eq. (1.2) to obtain

$$P_B - P_A = r_A u D \tag{1.4}$$

Elimination of u, the particle velocity in the shocked state, from Eqs. (1.2) and (1.4) gives an expression for the shock velocity D in terms of the initial and final states in (P,v) space.

$$r_A^2 \, D^2 = (P_B - P_A)/(v_A - v_B) \tag{1.5}$$

This expression is the well-known Rayleigh line equation.

The conservation of energy across the shock wave is written as

$$e_A + P_A v_A + \tfrac{1}{2}D^2 = e_B + P_B v_B + \tfrac{1}{2}u_B^2 = e_B + P_B v_B + \tfrac{1}{2}(D-u)^2 \qquad (1.6)$$

Elimination of u and D from the energy equation [Eq.(1.6)] is obtained by substituting in the mass and momentum equations (Eqs. 1.2 and 1.4). The result is a relation between e , P, and v in both upstream and downstream states known as the Hugoniot equation. It is expressed as

$$e_B - e_A = \tfrac{1}{2}\,(P_A - P_B)(v_A - v_B) \qquad (1.7)$$

Before introducing chemical reaction terms into the energy jump condition, a graphical description of the Rayleigh lines and Hugoniot curve is in order.

Figure 1.10 is a typical plot of the Rayleigh line and Hugoniot curve for a simple compressible substance. The material is HMX, r_p=1.90 g/cc . State A (v_A, P_A) describes the material thermodynamic properties prior to being shocked and State B (v_B, P_B) represents the shocked state. It should be pointed out that the Hugoniot curve connecting State A to State B does not represent the thermodynamic states a material particle passes through when shocked from A to B. The Hugoniot curve is only a set of possible <u>end</u> states in a shock process. <u>It does not represent a path process</u> .

From Eq. (1.7) and Fig. 1.10, it can be shown that the

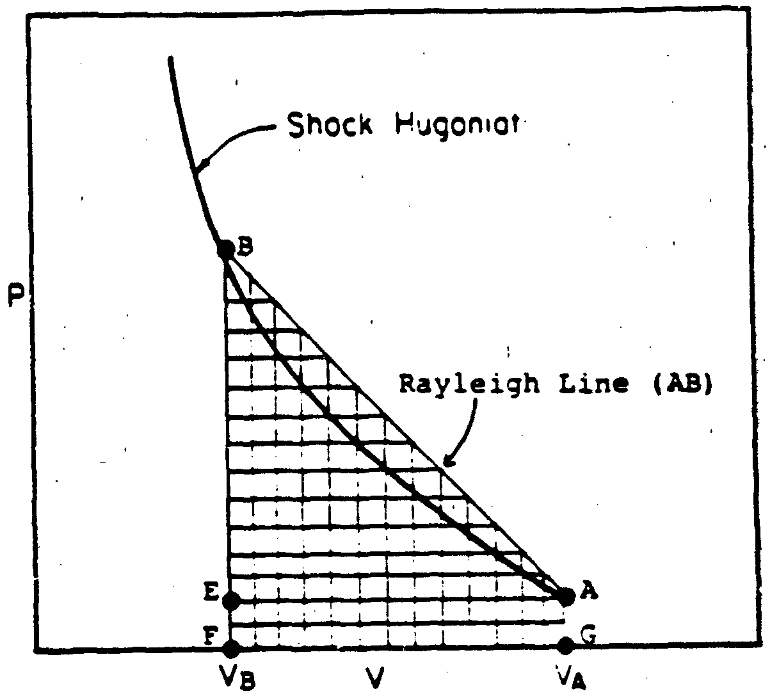

Fig. 1.10 Illustration of shock Hugoniot in Pressure, specific volume space.

increase in internal energy due to a shock compression is graphically equal to the trapazoidal area ABEFG. If $P_A = 0$, as in most condensed phase shock processes, the area approaches the triangular area ABEA. Also, manipulation of the energy jump condition and momentum jump condition yields

$$u_B^2 = P_B\,(v_B - v_A)\;/\;2 \tag{1.8}$$

Thus, in a shock process, one-half of the energy deposited by the shock wave goes into accelerating the material to a velocity u and one-half of the energy goes into increasing the internal energy of the shocked material. Since the scope of this work involves solid materials, a detailed discussion of the internal energy in a shocked state will be included in a later section.

Consider a shock wave passing through a chemically reactive material. If the amount of energy released is equal to E_{ch}, the Hugoniot for the fully reacted material is given by

$$e_A + P_A v_A + \tfrac{1}{2}D^2 = e_B + P_B v_B + \tfrac{1}{2}u_B^2 - E_{ch} \tag{1.9}$$

This is identical to Eq. (1.6) with the addition of the chemical energy term to the right-hand side of the equation. Figure 1.11 shows Hugoniots for values of (degree of reaction), $0 < \lambda < 1$. A value of $\lambda = 0$ indicates no reaction and a value of $\lambda = 1$ represents complete reaction.

The states labeled A, B, C, D in Fig. 1.11 represent a

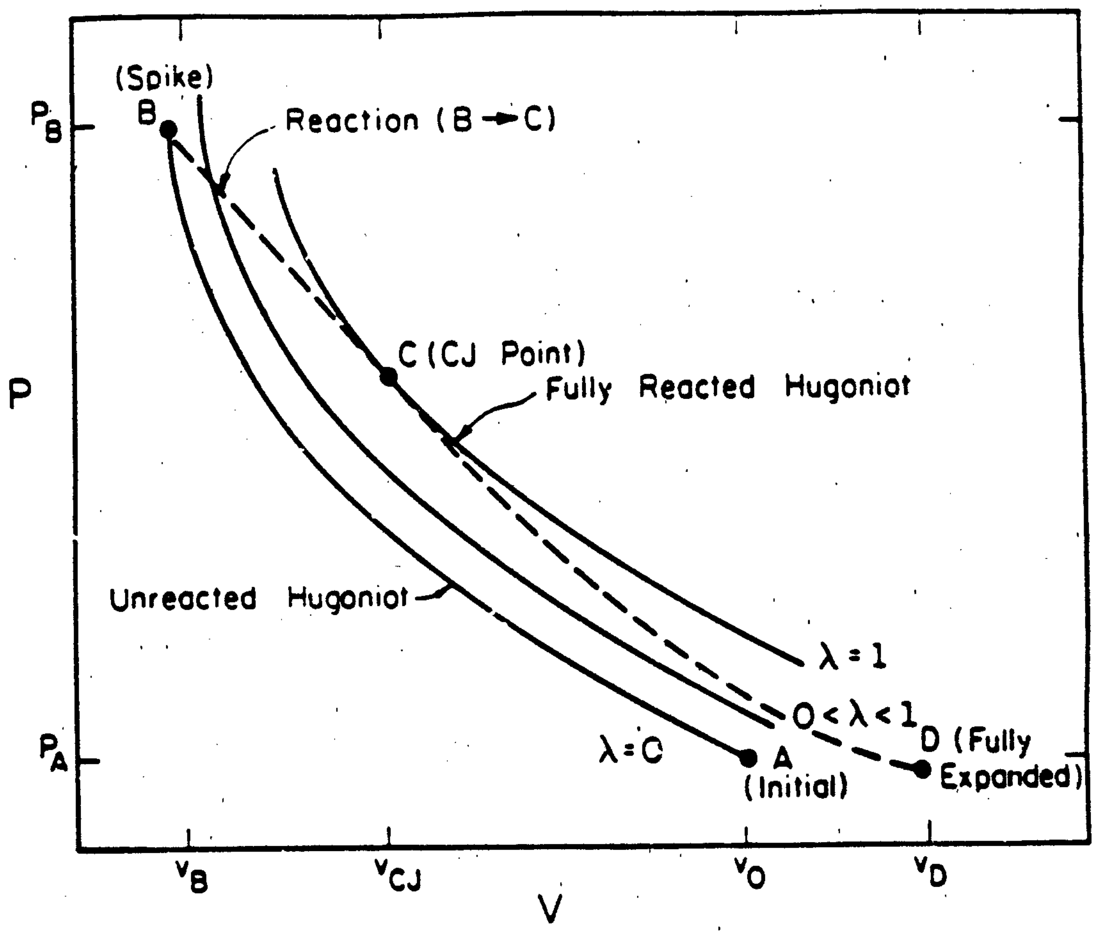

Fig. 1.11 Typical shock Hugoniots for reactive material.

typical detonation process. First, the ambient material (State A) is shocked to State B (P_B, v_B), the von Neumann spike condition. As stated earlier, the total energy deposited in the explosive across the shock front (A -> B) is given by

$$E_B = e_B + u_B^2/2 = P_B(v_A - v_B) \qquad (1.10)$$

where, E_B represents the total energy at State B. After being shocked to State B, the increase in internal energy causes the reaction to commence. This is represented by the dashed line starting at State B and ending at State C where reaction is complete and the product gases are in chemical equilibrium. In going from State B to State C the kinetic energy has decreased by

$$\Delta KE = \tfrac{1}{2}(u_B^2 - u_C^2) \qquad (1.11)$$

The final process is an expansion from State C to State D along a Taylor release wave. The corresponding P, x profile for the ZND detonation wave is shown in Fig. 1.12. For clarity, the reaction zone is not to scale with the rest of the figure.

It can be shown that a condition which must be satisfied in order for the detonation front to be constant velocity is

$$D = u + c \qquad (1.12)$$

at the point where reaction is complete and the detonation

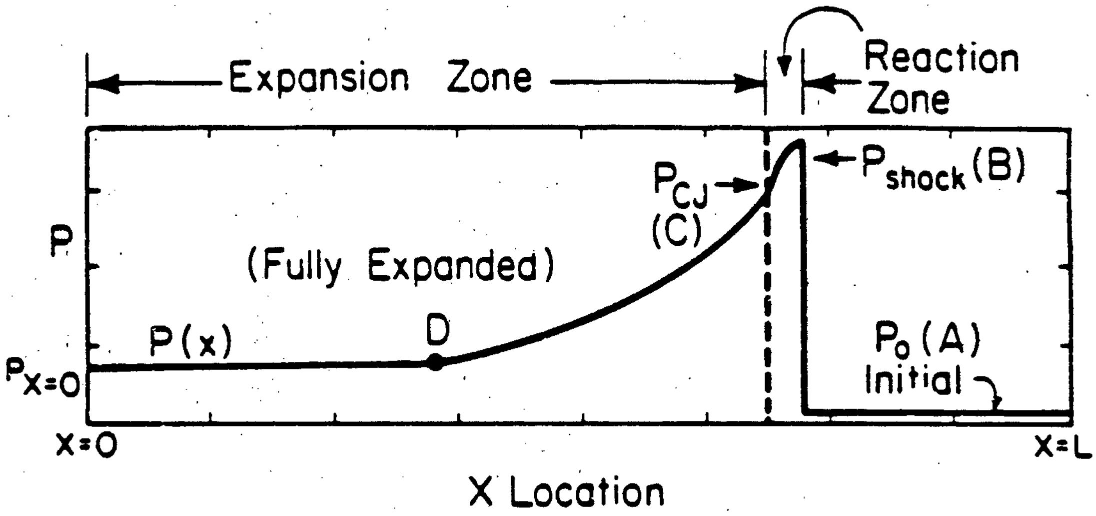

Fig. 1.12 Pressure, x-location profile for detonation wave. The states labeled correspond to Fig. 1.11

products are in equilibrium [25]. That is, at the end of the reaction zone (State C) the detonation products are traveling at a sonic velocity relative to the detonation front. Graphically this is the point where the Hugoniot curve and Rayleigh line are tangent. It is most commonly referred to as the Chapman-Jouget (CJ) point. In addition to the sonic condition at the CJ point,

$$u + c < D \qquad (1.13)$$

for any particle in the expansion wave. This implies that any small disturbance in the rarefaction region will not overtake the detonation front and attenuate the strength of the detonation wave.

The release wave from the CJ point rearward is a constant entropy process and the pressure at any state along the isentrope can be related to the CJ pressure by the expression [25]

$$P/P_{CJ} = [1 + \frac{(\gamma - 1)}{2} \frac{(u - u_{CJ})}{c_{CJ}}]^{\frac{2\gamma}{(\gamma-1)}} \qquad (1.14)$$

Here, u represents the particle velocity at the point of interest, c the sound speed and P the pressure. The subscript 'CJ' refers to the CJ point. The term γ is the logarithmic P,v slope of the isentrope passing through the CJ point.

$$\gamma \equiv -(\partial \ell nP/\partial \ell nv)\Big|_s \qquad (1.15)$$

Appendix A contains a simplified analysis of the detonation model for condensed explosive worked out by Hayes [29]. The assumption used is that the product gases are ideal with an artificially high specific heat ratio. The analysis given provides an estimate of detonation pressure and detonation velocity. Later in the text, a more precise equation of state for the detonation products will be introduced; however, for the analysis in Appendix A, the altered ideal equation of state is sufficient.

1.5 Shock to Detonation Transition

Before one attempts to analyze the DDT process in granulated propellant, a discussion on Shock to Detonation Transition (SDT) is appropriate. SDT occurs when a planar nonreactive shock wave, propagating through a homogeneous solid material, raises the pressure, temperature, and density to uniform values throughout the shocked matrix. Whether or not the temperature increase is great enough to cause initiation depends on the shock duration since the expansion wave following the shock will act to cool and extinguish the material. Shock propagation through porous reactive materials is not so well understood.

Experimental work cited in Chapter 2 shows that material samples containing voids and density irregularities will undergo shock to detonation transitions at much lower shock pressures than a homogeneous sample of the same material. Shock waves not strong enough to raise the bulk temperature of the material above the thermal explosion level are distorted by the density discontinuities of the porous material and subsequently superheat the material in these localized regions above the explosion level. Following this, the material reacts and strengthens the leading shock wave which causes the transition to a detonation. These "hot spots", as they are referred to, are an initiating mechanism in porous reactive material. The reader is referred to Ref. 30 which discusses various theories on shock initiation of condensed explosives.

CHAPTER 2

LITERATURE REVIEW: EXPERIMENTS AND ANALYSIS

2.1 DDT Experiments

Due to the obvious explosion hazard and complexity of the Deflagration to Detonation Transition (DDT) process in solid rocket motors, there are limited experimental data available to verify proposed models. It is nevertheless appropriate at this point to discuss and reference some of the more pertinent experimental work on detonations which occur in porous high-explosives and explosive-based solid propellants.

Following the work by Macek [23] on DDT in cast explosives, Griffiths and Groocock [31] studied the DDT phenomenon which can occur in porous explosives, confined in brass tubes. The explosives studied were RDX, HMX and PETN. The Russians have also investigated DDT in porous PETN [36]. Subsequent DDT research was performed by Bernecker, Price and coworkers [7,8,32] at the Naval Surface Weapons Center (NSWC), White Oak, MD. In this series of DDT experiments, the test apparatus consisted of a thick-walled steel tube, closed at both ends and packed with granulated, high-energy propellant. A schematic of the test bed is shown in Fig. 2.1 [7]. Ionization probes were placed at locations along the axial direction to track the flame front as it propagated through the explosive medium; and strain gages, fixed to the exterior of the surrounding steel shell, were used to determine

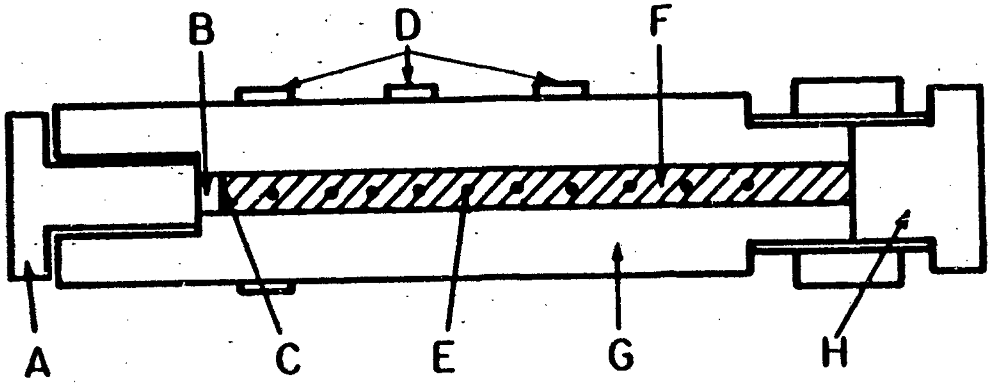

Fig. 2.1 Schematic of test apparatus used by Bernecker and Price at Naval Surface Weapons Center. (A-ignitor bolt, B-ingitor, C-ignitor/explosive interface, D-strain gages, E-ionization probe location, F-explosive charge, G-tube, H-far end closure). Taken from Ref. 7.

stress levels in the walls. Of course, strain gage data taken on the wall exterior is not always an indicator of the instantaneous pressure inside the tube. Reaction in the pregranulated propellant was initiated at one end of the DDT tube by a 0.33 gram charge of Boron/Potassium Nitrate (B/KNO3) ignited by a hot bridgewire.

In the first set of experiments [32] ammonium picrate at various loading densities and a 95/5 mechanical mixture of trinitrotolulene (TNT)/wax were tested for DDT. Both of these explosives are insensitive to detonation by weak shock compression. Data from the strain gages showed that both cases exhibited a slow rate of pressurization behind the reaction zone. In addition, the ionization probes detected the propagation of a convective flame front through the porous medium at subsonic velocities relative to the undisturbed material. The pressurization of the product gases was due to the confinement provided by the closed-end tube configuration. In the experiments the reaction front was observed to travel at approximately 0.6 mm/µs at the end nearest the igniter and accelerate slightly as it propagated further into the porous bed. This value for flame front velocity represents an average for all the experiments reported. The experiments conducted using ammonium picrate showed a slightly increasing velocity with increasing charge density [25], due in part to the increased confinement. Although these propagation velocities are much faster than the linear regression rate of the material (heat transfer by conduction), they are still subsonic by a factor of 3 or 4. Thus, disturbances in the reaction zone can be propagated upstream of the ignition front. An interpretation of the strain gage data (material stress), along with the ionization probe data (ignition front x-t trace), indicates that the pressure in the bed increased slightly prior to passage of the ignition front and then increased in a linear fashion after reaction commenced. This is consistent with the proposed theory [32] that product gases seep through the porous bed upstream of the ignition front. As expected, neither the AP or TNT/wax mixture showed a transition to detonation from the subsonic deflagration mode.

A 91/9 mechanical mixture of RDX/wax was used in the second series of experiments conducted at NSWC [8]. The weight mean particle size of the RDX was calculated to be d_o = 200 μm. Unlike the previous work [32], the material used in these experiments (RDX) is considered shock sensitive. That is, RDX has been shown to undergo shock to detonation transition (SDT) when shock heated in flyer-plate impact experiments [5]. The results presented in Ref. 8 indicate a transition to detonation for a range of initial TMD's of 67-95% where 100% TMD (theoretical maximum density) is defined as the density of a material sample containing no voids. For example, 50% TMD represents a sample of material containing 50% voids by volume.

Figure 2.2 [8] represents a typical position-time plot for a case which has exhibited a transition to detonation. These data are for a 78.8% TMD RDX/wax mechanical mixture. The first six data points (t=0 to t=190 μs) were interpreted as the convective flame front, accelerating from 0.38 to 0.61 mm/μs. At the location

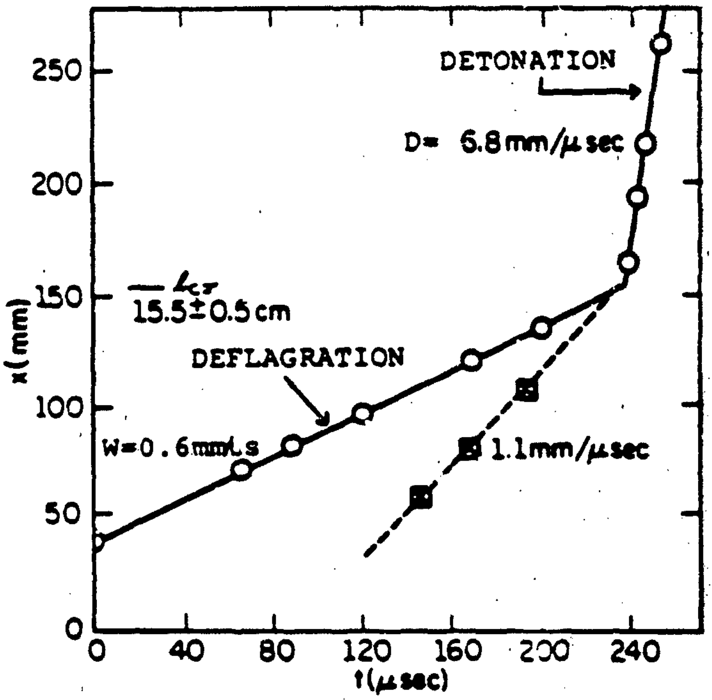

Fig. 2.2 Experimental Results for 78.8 % TMD (ϕ_c = 0.22) 91/9 RDX/wax; r_2 = 1.32 g/cc (taken from Ref. 8)

x=15.5 cm, the x-t trace shows a definite transition to a steady state detonation with velocity D = 6.8 mm/μs. The study showed that DDT occurred in the explosive samples which exhibited a rapid pressure rise, dP/dt, in the ignition region.

It should be noted that consistency in the type and quantity of igniter material is an important factor when comparing the detonability of different propellants. A strong (high pressure-rise rate) igniter system can send a precursor elastic wave upstream of the ignition front and "pretreat" the porous material by elastically closing pores and eliminating potential sites for localized heating. Since the sensitivity of an explosive to shock initiation is highly dependent on the void fraction and void size [30], this "pretreat" phenomenon should be avoided if one's goal is to show quantitative comparisons between porous explosive materials. It appears that the work conducted at NSWC [7,8,32] was carried out using similar igniter strengths, weak enough not to collapse the material voids.

A model for the transition to detonation from deflagration was developed by the NSWC group from the data obtained in their closed tube experiments [8,32]. It was concluded that highly reactive and shock sensitive materials (RDX,HMX) , when ignited in a confined bed, generate product gases rapidly enough to shock compress and detonate the remaining material which is upstream of the reaction front. An x-t trace of a typical DDT is illustrated in Fig. 2.2 . Initial conditions and material parameters such as loading density, particle size, permeability and product gas confinement were found to be important in determining whether or not the reactive material can generate gas rapidly enough to shock initiate the explosive.

Another item of interest is that Tetryl did not exhibit the sequence of events leading to DDT that HMX and RDX exhibited [33]. Ionization probe and strain gage data for both HMX and RDX showed the subsonic convective ignition front to accelerate prior to steady state detonation, accompanied by a localized pressure buildup near the reaction front. This phenomenon was not observed when Tetryl was used. For the experiments using Tetryl, a zone of rapid pressure increase was seen upstream of the ignition zone, near the transition location. This led the authors to suggest and later prove that Tetryl could exhibit transition to detonation under much less confinement than was provided by the steel tubing used in this particular set of experiments.

The next series of DDT experiments at NSWC [34] used a lightweight Lexan plastic tube to contain the explosive sample. The purpose for using transparent plastic DDT tubes rather than steel tubes was twofold. First, the plastic tubes provided much less confinement; second, photographic techniques could be used to trace the ignition front as it propagated through the bed. The photographic techniques were used in addition to the standard ionization-probe measuring technique which was used in the previous work on DDT at NSWC [7,8,32]. Both coarse Tetryl (d_o = 470 μm) and very fine HMX (d_o = 15 μm) were shown to detonate under conditions of low confinement in the plastic tubes. They concluded that the pressure buildup leading to DDT was so rapid that DDT occurred before the plactic walls were able to respond to the overpressure.

In similar experiments, Sulimov et al. [35] reported on the conditions necessary to stabilize a Convective Burn (CB) and a Low Velocity Detonation (LVD) in a porous bed of high energy propellant. Although both the CB and LVD typically occur as transient processes (i.e., DDT), the authors chose to study the two reaction waves under steady state conditions. This was accomplished by controlling the gas pressure in the zone behind the ignition front. Both processes are important in the detonation buildup phase of a DDT and they should be investigated.

A CB is characterized by hot product gases penetrating the unreacted material upstream of a subsonic ignition front [35]. In this process the flow of hot gases over the unreacted explosive causes heat transfer (convective) to the explosive, an increase in internal energy, and eventual ignition of the heated surface. The authors concluded by stating that a CB in a porous bed will stabilize if the following conditions are satisfied. First, the porosity and gas permeability of the charge are lower than certain threshold values; second, the maximum pressure in the combustion zone is maintained at a constant level; and finally, a subsonic flow of the combustion products is maintained. The first and second items are necessary in order to obtain a balance between gas production in the reaction zone and gas loss from the reaction zone.

In the case of an LVD, a weak nonelastic compression wave precedes the ignition front, collapsing pores and generating plastic deformation of the material. It is assumed that localized regions of material with increased energy due to intergranular friction and shock focusing, react and generate product gases. These high pressure product gases are what support the upstream compression wave. As pointed out in Ref. 35, both the CB and LVD are different from a classical detonation wave because the majority of the reaction products are not generated in the vicinity of the ignition front. Only 10-20% are generated near the reaction front. The remaining reaction occurs in a zone downstream of the ignition front.

The dependence of convective burn velocity (W) on the peak pressure (P_m) is illustrated in Fig. 2.3 [35]. Here, the peak pressure was defined as the pressure in the zone adjacent to the ignition front for the CB and the pressure immediately behind the lead compression wave for the LVD. Figure 2.3 is for the explosive PETN with an initial porosity of 0.1. A stabilized CB is possible when $.01 \text{ GPa} < P_m < .02 \text{ GPa}$. The dashed line from $P_m = 0.02$ GPa to $P_m = 0.2$ GPa indicates that an accelerating convective burn was observed in this range of P_m. The authors also showed that a steady LVD is possible for values of $0.2 \text{ GPa} < P_m < 2.0 \text{ GPa}$.

A second important aspect of the Sulimov research is their interpretation of streak photographs taken of what appeared to be a steady CB. Actually, the wave motion was quasi-steady with

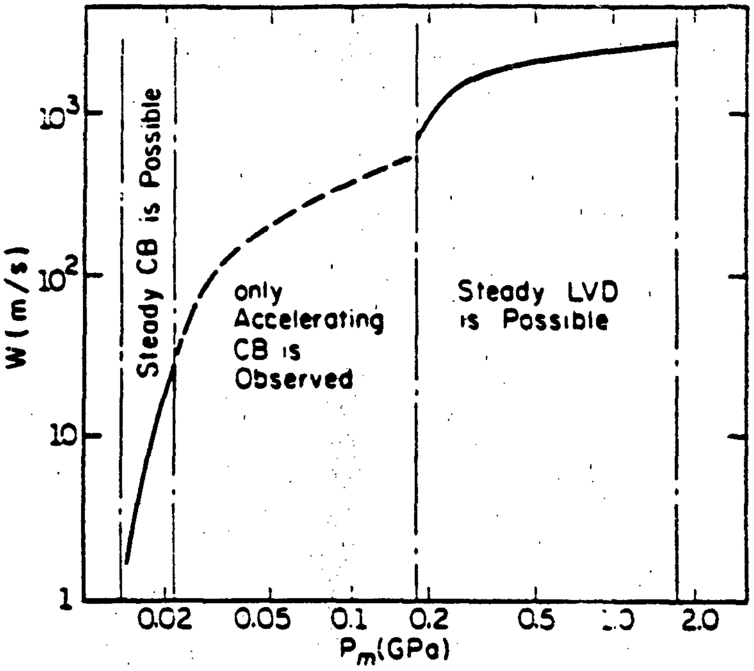

Fig. 2.3 Convective burn (CB) velocity (W) dependence on maximum pressure (P_m). The material is PETN and the initial porosity is 0.1 . ('LVD' refers to low velocity detonation) (Taken from Ref. 35)

large amplitude, high frequency spikes appearing on the photographs depicting the x,t trace of the ignition front. It was hypothesized that the high frequency oscillations appearing in the photographs were due to intense fragmentation of the explosive in the combustion zone. The authors suggested that penetration of the product gases into the unreacted zone accompanied by a sudden pressurization caused fracture of the material. The result was an unsteady convective burn.

More recently, Campbell [4] experimented with samples of granulated HMX in a detonation tube similar to Bernecker's [8,32] but segmented with neoprene disks. The disks retarded the flow of hot gases through the porous bed, but at the same time allowed stress waves to be propagated upstream and initiate detonation. Figure 2.4a is a sketch of the DDT tube used by Campbell. Each of the zones shown in the figure is packed with granular explosive and separated from the adjacent zones by the neoprene disks. Ignition begins at the left end of Zone 1 and propagates to the right. The accompanying figure, Fig. 2.4b, shows the pressure profiles (P,x) in each of the zones. At time t_4, the ignition front has just reached the first neoprene disk. The pressure profile for time t_5 shows a reflected wave in Zone 1 and a transmitted wave in Zone 2. If of sufficient strength, the transmitted wave initiates reaction in Zone 2 by shock compression. The process repeats itself when the detonation wave in Zone 2 interacts with the Zone 2/Zone 3 disk and again when the detonation wave reaches the Zone 3/Zone 4 interface.

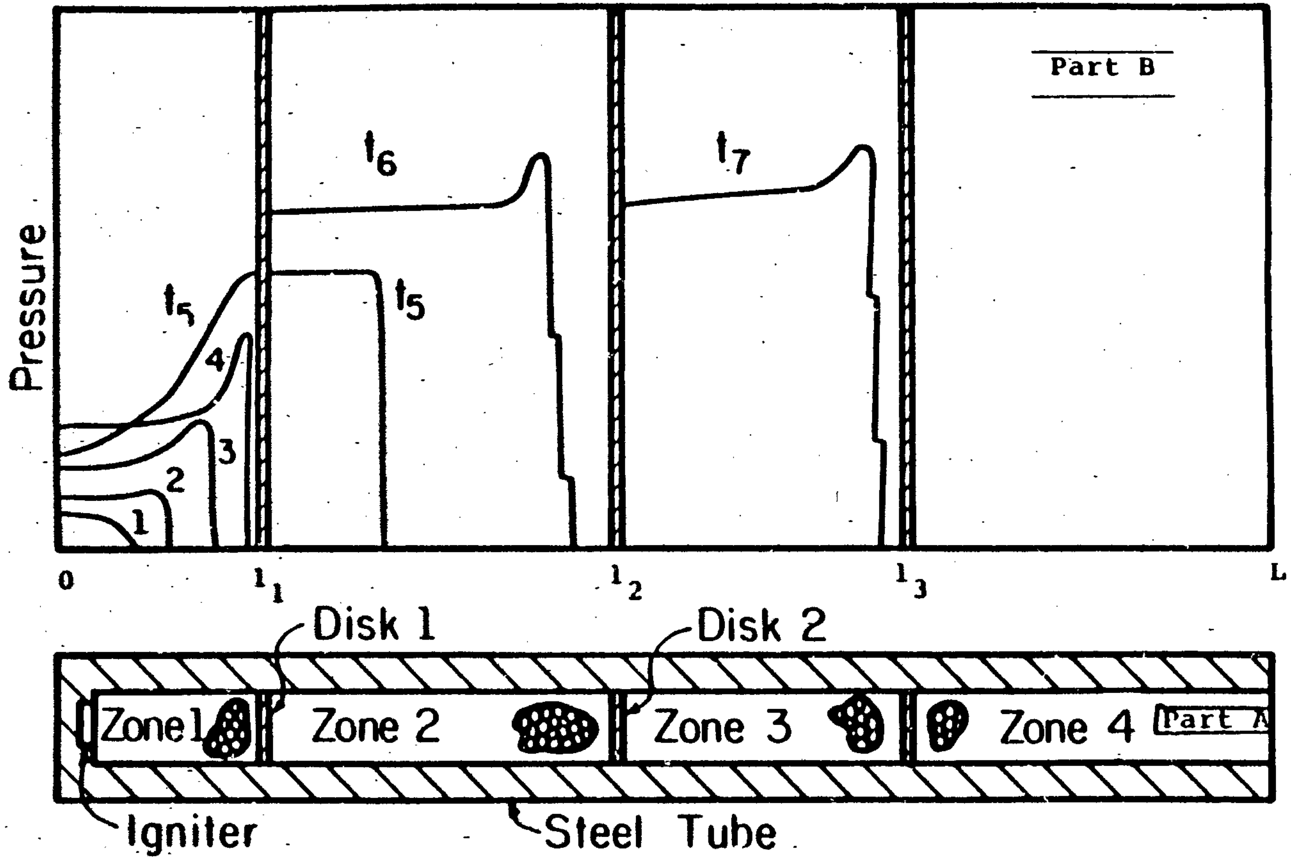

Fig. 2.4 Schematic (Part A) of Campbell's experiment [4] and illustration of assumed pressure- x-location profiles (Part B). The burning granular propellant in Zone 1 shock initiates the propellant in Zone 2.

Because he was able to reproduce detonation run-up lengths with or without the neoprene disks inserted, Campbell concluded that convective burning could only be important in the early stages of DDT (i.e., Zone 1, Fig. 2.4). He also stated that a "plug" (total void collapse) must form in the bed, terminating all convective burning and leading eventually to shock to detonation transition (SDT). The computer calculations presented in Chapter 5 also predict plug formation, but only under certain circumstances (i.e., low pressure-rise rate behind the ignition front). Figure 2.5 is a summary of Campbell's data showing detonation run-up length ℓ_{CJ} as a function of effective particle size.

2.2 Pop-plot Data

One of the most important references in explosive hazards evaluation is the Pop-plot, named after its originator, N. Popaloto [37]. The Pop-plot equates shock strength P_s to run-up to detonation distance ℓ_{CJ} on a log-log scale. Most explosives have a linear $\log P_s - \log \ell_{CJ}$ plot, with negative slope, $d(\log P_s)/d(\log \ell_{CJ})$. This indicates a longer run-up distance for a weaker wave and vice-versa.

Pop-plot data for homogeneous samples of high explosives are obtained by performing a standardized wedge test [5]. In the test, the (x,t) trajectory of a shock traversing a wedge-shaped sample is recorded by photographic techniques. Figure 2.6 shows a Pop-plot for several high explosives with near-crystalline

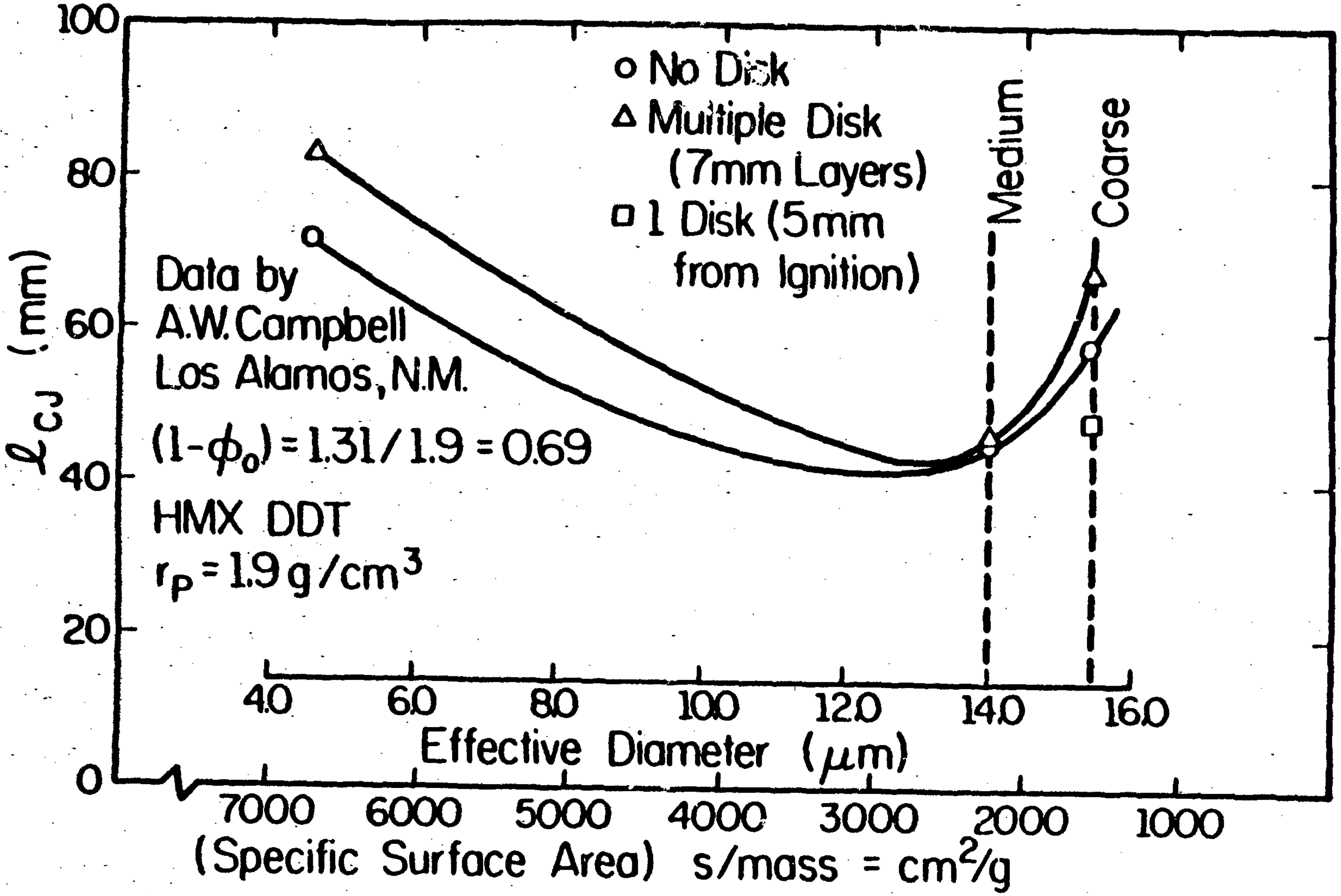

Fig. 2.5 Summary of Campbell's data [4] showing detonation run-up length ℓ_{CJ} as a function of specific surface area

densities. They include HMX (1.891 g/cc), PETN (1.75 g/cc) and Tetryl (1.70 g/cc).

Dick [5] was successful in obtaining Pop-plot data for samples of HMX with an initial density of $r_2 = 1.24 \pm .04$ g/cm (35% voids). Since most heterogeneous materials are composed of a large distribution of particle sizes and shapes, tracing a distance-time trajectory is often difficult using the wedge technique. The data acquisition technique used by Dick was different from the wedge technique. Instead of tracking the shock's (x,t) trajectory, Dick measured only the total duration of the wave passing through the explosive sample. Thus, he was able to determine one point on an x-t plot for each sample. Many tests were performed and a statistical sampling provided the porous HMX ($r_2 = 1.24$ g/cc) Pop-plot data shown in Fig. 2.6. A least squares fit to the data gives

$$\log \ell_{CJ} = \log (4.6) - 0.56 \log (P_s) \qquad (2.1)$$

Note that the Pop-plot for 35% porous HMX (TMD=0.65) lies below those of homogeneous PETN, Tetryl and HMX. This indicates that for a given shock strength, the run-up distance is much less for porous HMX than for the three other materials shown. In terms of hazard evaluation, the shorter the run-up length, the more hazardous the material.

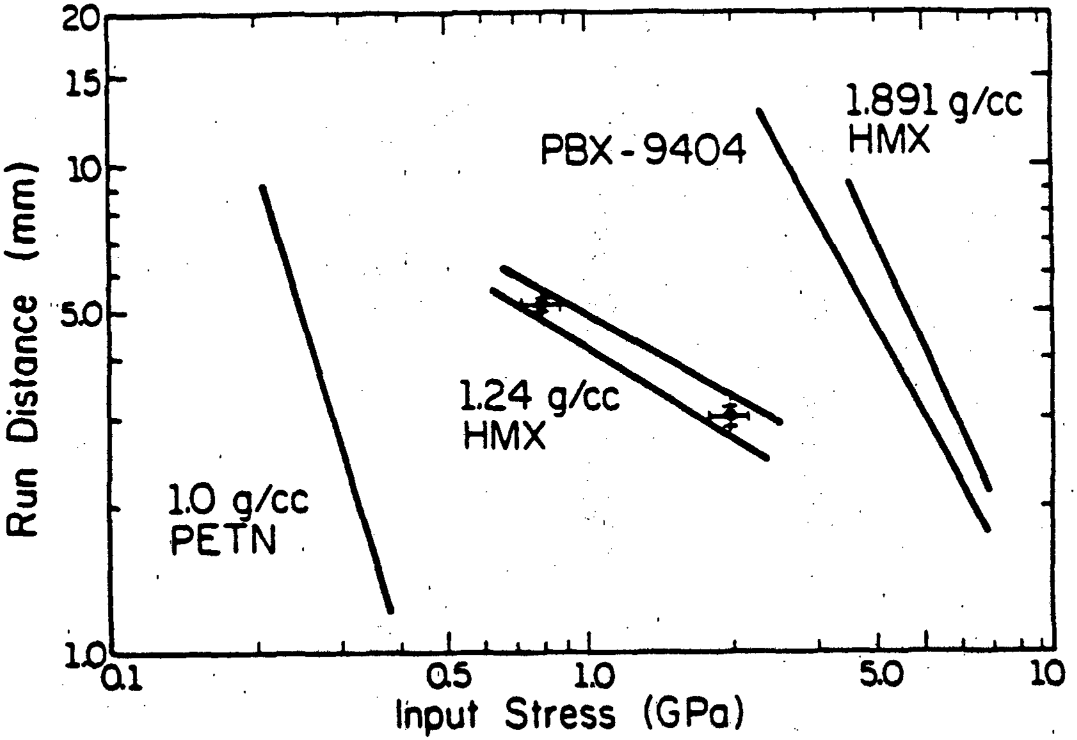

Fig. 2.6 Pop-plot data for various high-explosives. Data for PETN, PBX-9404, HMX(1.89 g/cc) is from Ref. 78. Data for HMX(1.24 g/cc) is from Ref. 5.

2.3 DDT Analysis

The analysis and simulation of the reactive two-phase flows associated with the DSDT event must compliment such experimental findings. Detailed modeling of the DSDT events in porous high-energy propellants has been carried out by Krier and co-workers [1,10-14,38,39] at the University of Illinois over the past several years and more recently by Baer, Nunziato and Gross [16] at Sandia National Laboratories, Albuquerque. Both of these research groups model the DDT process by solving the unsteady two-phase flow equations along with the proper constitutive relations. Extensive research at the University of Illinois has advanced the analysis from the equation development stage [38] to predicting actual DDTs in granular beds [1,11]. In related research the group has studied shock wave development in porous energetic materials [28]. The Sandia group has advanced the analysis effort by implementing a rate-dependent pore collapse model and thermodynamically correct equation of state for the solid phase. More recently, they have studied DDT in CP, an extremely energetic high-explosive.

Using a version of Krier's code, Pilcher, Beckstead, Christensen and King [40] investigated the effects of tube deformation on DDT in porous beds of high energy solid rocket propellants (HMX-based). The research involved a series of ten DDT experiments in addition to corresponding numerical predictions. HONDO [41], a dynamic structural analysis code (provided by Sandia Laboratories) was used in conjunction with the

Krier/Van Tassel [10] two-phase flow code in order to couple flame spreading through the porous bed with the motor case deformation. For the material examined (HMX, 500 μm<d_o<1000 μm), the occurrence was dependent on the degree of confinement of the product gases.

Out of the three test configurations used in the experiments, the one shown in Fig. 2.7 is the most applicable to the work at hand. The sketch shows a closed tube containing a segment of undamaged propellant. In contact with the undamaged propellant is a zone of granulated propellant covering the full diameter of the test tube and adjacent to the granulated propellant is a void containing the igniter. This particular test configuration showed DDT in all the tests conducted except one. For those which showed DDT it was assumed that rapid combustion in the porous bed provided the necessary pressure-rise rate to shock initiate the undamaged propellant. This particular DDT scenario (DDT-Case 2) was also examined in Ref. 14.

Others who modeled DDT in porous explosives [42,43] reduced the problem to a one-phase flow analysis by neglecting the seepage of hot gases through the porous explosive. Forest [43] made use of Pop-plot experimental data on heterogeneous detonations to derive an effective chemical reaction rate in the shocked explosive and was thus able to show the shock to detonation phase of DDT. In brief, his technique involved calculating the reaction rate necessary at a given time to develop a detonation strength shock within the known Pop-plot run-up distance.

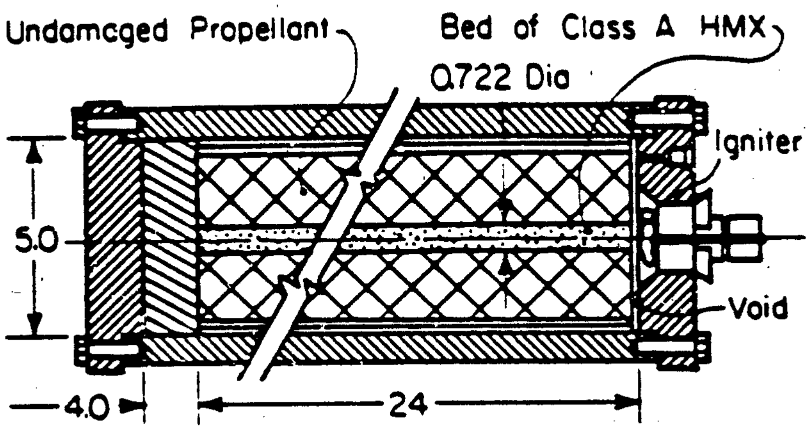

Fig. 2.7 Schematic of test configuration used by Pilcher et. al [40]. (Dimensions are in inches)

Work performed by Macek [23] and Tarver et al. [44] used the method of characteristics to predict shock development in homogeneous solid explosives. Macek used the secondary explosives diethylnitramine dinitrate (DINA) and 50/50 Pentolite in his end-burning DDT experiments. Assuming an exponential pressure rise in the product gases, Macek traced right-running characteristics (lines of constant stress) on a distance-time (x,t) plot and showed that the lines coalesced at approximately the detonation run-up length observed in experiments. An example is shown in Fig. 1.8a. The run-up length is defined as the distance from the gaseous products/unreacted explosive interface to the downstream location where the detonation originates. The coalescence of the characteristics in Macek's analysis was interpreted as the formation of a shock wave which was assumed to cause the explosive to detonate.

Although Macek's method of characteristics approach to the DDT analysis seems relatively straight forward, several inconsistencies were pointed out by Tarver et al. [44] and later by Kooker and Anderson [42]. The most obvious came in attempting to predict the pressure-rise rate in the combustion zone. Macek used strain gauges on the exterior of the DDT tube to measure the pressure-rise rate in the product gases. The data were then fit to the equation

$$P(t) = Z \exp (kt) \qquad (2.2)$$

where Z and k are constants. The values of Z and k given by Macek were $Z = 0.008$ GPa and $k = 0.10\,\mu s^{-1}$. Macek then used Eq. (2.2) as the stress input function for the method of characteristics analysis of the unreacted explosive material. The inconsistency in this approach, as pointed out by Jacobs [45], is in assuming that the details of propellant burning can be modeled as a one-dimensional linear process. Jacobs showed that the surface area available in the assumed linear regression (conductive burning) was far too little to generate the pressure-rise rate predicted by Macek. Kooker and Anderson later suggested that breakup of the burning surface could enhance the available surface area for burning. Coyne et al. [28] extended the work of Macek to include porous propellants.

2.4 Critical Energy ($P^2 - \bar{t}$) Concept

An important parameter in the evaluation of secondary explosives and explosive-based solid propellants for potential hazards is the minimum input energy necessary to initiate SDT. Walker and Walsey [46] were the first to correlate the energy transmitted upon impact from a flyer plate to an explosive sample with a 'Go' or 'No-Go' detonation result. The materials tested in the original work included PBX-9404, LX-04 and TNT. All the samples tested had high TMD's (low void volume). Figure 2.8a [46] shows the general trend of the data obtained when a flat-nosed projectile of mass, m and velocity, V' impacted a stationary explosive sample. In reality, each material would have its own

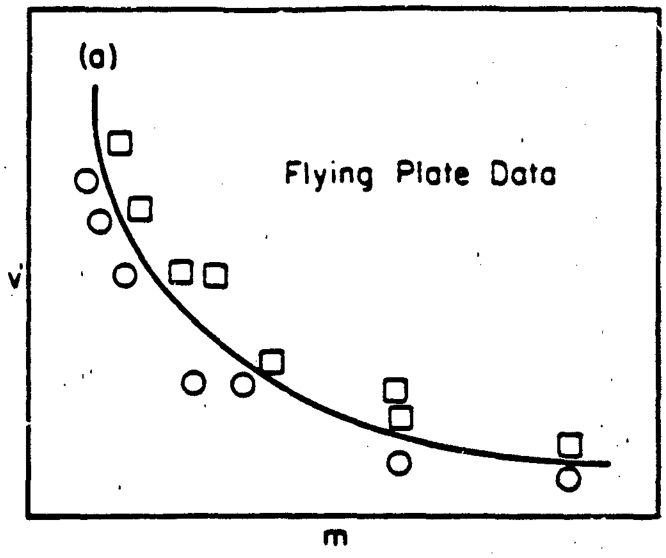

Fig. 2.8a Typical projectile velocity versus projectile mass plot for Shock to Detonation experiment. (□ indicates a 'GO' result, ○ indicates a 'NO GO' result)

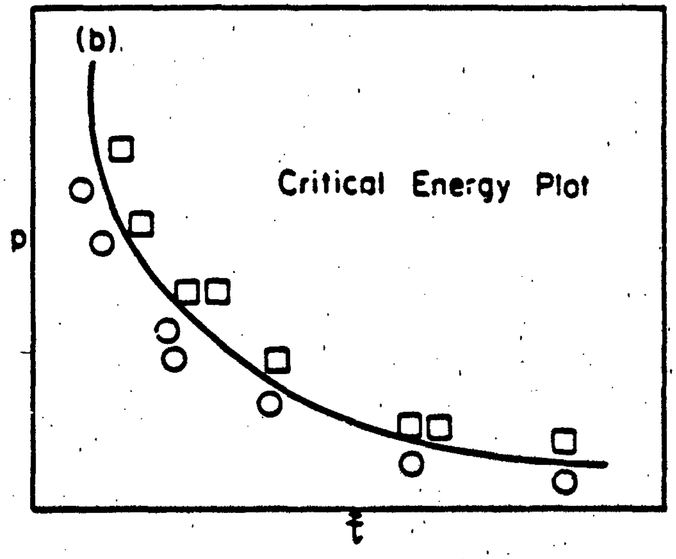

Fig. 2.8b Transformation of critical energy data from velocity, mass space to pressure, shock duration space. '$\bar{t}$' represents shock duration in the sample.

curve in m,V' space. The squares in Fig. 2.8a represent a 'Go' detonation result and the circles represent a 'No -Go' detonation failure. By using impedance matching techniques and the mass, momentum and energy conservation laws, the authors transformed the data in m,V' space (Fig. 2.8a) to data in $P, \bar{t}$ space (Fig. 2.8b) where P is the shock strength and $\bar{t}$ is the shock duration. The resulting equation for critical initiation energy is

$$E_c = A P^2 \bar{t} \tag{2.3}$$

where A = constant = $1/(r_o D)$. Assuming one-dimensional wave theory, the shock duration $\bar{t}$ is simply the time after impact required for the compression wave to transit the projectile and return from the free end as a rarefaction wave.

An interpretation drawn from Fig. 2.8 is that a shock of strength P requires a duration of at least $\bar{t}$ in order to shock initiate the material. It is obvious from Fig. 2.8b and Eq. (2.3) that as the shock strength decreases, the duration, $\bar{t}$, must increase if SDT is to occur. Whether or not the Walker and Walsey P^2-$\bar{t}$ critical energy theory holds for all explosives is debatable [47-49].

Howe, Frey, Taylor and Boyle [30] pointed out that although the P^2-$\bar{t}$ theory is applicable for low void volume explosives (high TMD), the theory does not hold when voids are introduced into the explosive sample. In their work samples of TNT were found to have different critical initiation energies, depending on the propellant particle size. It was later pointed out by Walker [47] that experiments like Howe's [30] were misleading in regards to the $P^2\bar{t}$ theory. It was argued that E_c in Eq. (2.3) represents only the amount of energy transmitted across the projectile/explosive interface. Once the stress wave begins traveling through the explosive material, density discontinuities may alter the local energy levels. For example, voids present in a material have the effect of redistributing the energy as the shock propagates through the material. Shock focusing in these voids may cause the localized energy to be ten times greater than the bulk shock energy. One can see that although the $P^2\bar{t}$ theory may hold for pure samples (100% TMD), the theory may not correlate with experimental data when the material contains structural irregularities.

2.5 Research on Initiating Mechanisms in Porous Explosives

As stated earlier, it has been found that heterogeneous explosives can undergo SDT when shocked to stress levels below the minimum necessary to cause SDT in a homogeneous sample of the same explosive. At these low shock strengths the bulk temperature of the solid explosive is below the critical temperature needed for thermal explosion. In general, the greater the void volume, the lower the shock strength necessary for detonation. A proposed theory for this occurrence is that portions of the explosive (hot spots) are preferentially heated to a temperature above the bulk shock temperature. References 50 and 51 present experimental observations made when explosives of varying porosity and pore size were initiated by planar shock waves. These will be discussed briefly in the following paragraphs.

Bowden [50] developed the theory that an inert gas was trapped in the voids of the explosive and was adiabatically compressed, thus creating regions of increased temperature. Data were presented which showed the high temperatures attainable as a result of adiabatically compressing air. It was noted that certain explosives will detonate at temperatures below their melting-point and therefore intercrystalline friction can be a possible initiation mechanism. On the other hand, other explosives melt before they detonate. Because of the onset of plastic flow in this second group of explosives, compressing voids of trapped inert gas is a viable mechanism for generating localized high temperatures.

A second hot spot theory emphasizes the nonplanarity of the propagating shock wave [51]. The proposed idea is that as the shock wave traverses the explosive, density discontinuities (voids or irregularities in the explosive) cause the wave to bend and converge. The shock wave collisions create regions of increased material compression and temperatures above the bulk shock temperature. It was hypothesized that the hot spots then cause rapid thermal decomposition which acts to reinforce the shock wave. This part of the theory is supported by observations that show detonation to originate close to the shock front for heterogeneous explosives. Unlike heterogeneous explosives, homogeneous explosives are initiated at the striking body/explosive slab interface.

Some important conclusions drawn from this work, that are supported by experimental data, are:

1. Heterogeneous explosives detonate at much lower shock strengths than homogeneous explosives

2. A heterogeneous explosive becomes easier to detonate as the density decreases (void volume increases)

3. The shock strength needed to detonate heterogeneous explosives does not have to be strong enough to raise the bulk temperature above the thermal explosion temperature; it only needs to raise the hot spot temperature above the explosion temperature

4. The effectiveness of a hot spot in causing reaction in the surrounding explosive depends on the strength of the shock

5. An increased shock strength will increase both the temperature of the hot spot as well as the temperature of the reactive material surrounding the hot spot

6. Detonation originates at the piston/explosive interface for homogeneous explosives while it has been observed to originate at the shock front for heterogeneous explosives.

More recently Hayes [29] developed an energy partition model where the shocked porous material is assumed to be at one of two possible temperatures, a bulk shock temperature or a hot spot temperature. The enegy deposited by the shock wave is equated on a mass fraction basis to the sum of the reversible work done in isentropically compressing the bulk of the material, plus the irreversible heating of localized hot spots

$$p\ (v_{oo}-v)/2 = W_H\, e(P,T_H) + (1-W_H)\, e_s(P) \qquad (2.4)$$

In Eq. (2.4) the left-hand side represents the total energy deposited in the material by the shock of strength, P. The term $e_s(P)$ represents the energy required to isentropically compress the bulk of the material to the final shock pressure and the remaining energy term, $e(P,T_H)$, is the energy available to irreversibly heat the hot spots. The Hayes model assumes the mass fraction of the hot spots, W_H, to be equal to the preshock volume fraction of pores.

$$W_H = V_{oo}/V_o - 1 \qquad (2.5)$$

Here, the subscript 'oo' represents the initial porous state and the subscript 'o' refers to the homogeneous initial state.

2.6 Summary

In this chapter some of the more relevant research on DDT in porous energetic materials has been reviewed. The first part of the chapter focused on experimental research and the second half reviewed DDT analysis. A short discussion was also included on hot spots and the critical energy theory of initiation.

Experimental research on DDT dates back to the early 1960's. DDT tube experiments have provided useful information about detonation run-up length, convective burn velocity, detonation velocity and in some cases, compaction histories of the porous bed. However, information about the fluid mechanics and shock physics of the DDT process can only be inferred from these types of experiments.

Analysis of DDT in cast explosives was first done using a method of characteristics approach. The work showed that the location of shock formation was also the location of shock initiation. More recently, the research conducted in DDT analysis has focused on understanding all the details of the two-phase flow behavior in the DDT event. In addition, there is ongoing research in trying to better understand the mechanisms responsible for hot spot formation in porous energetic materials.

The work reviewed in this chapter is a small fraction of all the available literature on DDT and related topics. For more information, the reader is referred to the proceedings of the International Symposium on Detonation (1-7) published by the Office of Naval Research.

CHAPTER 3

THE MODEL

3.1 Introduction

The governing equations and constitutive relations describing time dependent two-phase reactive flow are discussed in this chapter. Recall that the problem of interest involves a packed bed of solid particles, confined, and ignited at one end at time $t=0$ (Fig. 1.2). A separated-flow analysis [38,39,52] is used to define the field variables and flow equations for both the solid phase and the gas phase. The basis for this approach is to separate the solid from gas and to treat each phase as a continuous flow field, coupled to the other phase by appropriate source-sink interaction terms. A second assumption made in the analysis is that the mass weighted gas/solid mechanical mixture of the two phases is also a continuum. As will be discussed shortly, this assumption imposes a constraint on the gas and solid phase source terms.

The governing equations resulting from this analysis are a system of nonlinear hyperbolic partial differential equations coupled through interphase transfer terms. When the conservations of mass, momentum, and energy for the separate phases are combined, a set of conservation relations similar to the individual phase equations are obtained for the mixture. These will be derived in Section 3.3. An analysis using the

Second Law of Thermodynamics will also be presented to account for the entropy production rate in multi-phase reactive flow. This fundamental thermodynamic constraint was overlooked in our previous work [1]. Recently, Baer and Nunziato [15] and before that, Nunziato and Walsh [53] used the entropy production inequality proposed by Truesdell [54] to develop source terms for the governing equations in addition to a kinematic model for void closure. The approach taken in this work is to first present the interaction terms and then show that they do indeed satisfy the Second Law of Thermodynamics.

In addition to the conservation relations, equations of state for both the gas phase and solid phase and an interphase force balance are required in order to have the number of independent equations equal to the number of unknown variables. These additional constraints will be presented in Section 3.4. For the gas phase, a nonideal P(v,T) equation of state was used, along with a constant specific heat e(v,T) caloric equation of state. At low density these equations describe an ideal gas.

The solid phase equation of state is presented in the form of a Helmholtz free energy function similar to the function used by Baer and Nunziato [15]. The constants appearing in the equation were obtained from shock-impact experiments conducted at Los Alamos National Laboratories [55]. Expressions for P(v,T) and e(v,T) needed for the hydrocode calculations are derived from the Second Law of Thermodynamics reciprocity relations between pressure, temperature, density and Helmholtz free energy.

Finally, Chapter 4 will include a method-of-lines finite difference technique used to solve the resulting system of differential equations discussed in this chapter. A one-dimensional shock tube example [56] is referenced in order to show a comparison between calculations made by the finite difference numerical scheme and the analytic solution. This example was deemed necessary since one has no way of determining the consistency of the numerical solution for the more complex two-phase flow problem. The term 'consistency' refers to how well the computer-generated solution compares with the analytic solution.

3.2 Separated Flow Analysis

The problem posed in this work involves modeling the transition from an accelerating convective ignition front to a steady state detonation wave that occurs in a packed bed of high-energy granulated propellant. A complete fluid dynamics/ thermodynamic description of this flow process must allow for each phase to have properties of its own, independent of the other phase. This implies that at any point in space, both phases can exist and have values different from one another for fluid velocity, u, as well as the thermodynamic properties pressure P, temperature T, and density r. The governing equations describing this particular flow process were developed using a separated-flow analysis. For more detail, the reader is referred to Wallis [46], Krier and Kezerle [38], and Krier and Gokhale [39]. Other researchers to use the separated flow analysis include Chao et al. [57], Crowe [58], Butler et al. [1] and more recently, Baer and Nunziato [15]. It becomes evident when one reviews Refs. 57 and 58, that there is some controversy regarding the exact form the governing equations should take. In particular, the role of inertial coupling terms in the resulting equations generates much discussion concerning their appropriateness. The approach taken in this work involves first presenting the conservation equations for each phase separately, and then combining the separate sets of equations to yield flow equations for the mixture.

Begin by assuming that each phase is itself a continuum. For the gaseous phase this implies that 'blind' pores are nonexistent and the gas is everywhere free to move. A blind pore is simply a pocket of gas isolated from the rest of the species. This assumption also means that the discrete nature of the individual solid grains is ignored and the array of packed particles is assumed to be a continuous fluid body. However, the particle-particle interaction force does appear in the constitutive relations defining the force balance between phases (see Sec. 3.6). The overall gas/solid mixture can also be assumed to be a continuum having mass weighted properties of the two phases. By treating each phase as a continuous body of mass occupying a finite volume, one can define thermodynamic properties $(P,T,v,e,h,s,\bar{S},r)_i$, dynamic variables $(u)_i$ and their continuous derivatives $(.)_x$ at every field location, x_i. Thus, each phase is completely defined at any given point in space. Here, P represents pressure, T temperature, v specific volume, e specific internal energy, h specific enthalpy, s specific entropy, $\bar{a}$ Helmholtz free energy, r density and u particle velocity. The subscript 'i' refers to the specific phase, gas (i=g) or solid (i=p). Likewise, the same variables and continuous derivatives can be defined for the gas/solid mixture .

For a given unit volume, V_T , assume that the volume occupied by the gas phase is V_g and that by the solid phase by V_p. Together, the sum equals the total volume

$$V_T = V_g + V_p \tag{3.1}$$

As a consequence of the multiple phases, a new variable ϕ is introduced where

$$\phi_i = V_i / \sum_i V_i \tag{3.2}$$

and from Eq. (3.1)

$$\sum_i \phi_i = 1.0 \tag{3.3}$$

A new variable termed the 'phase density' can be defined for each phase as

$$r_1 = \phi_g r_g \tag{3.4a}$$

and, $r_2 = \phi_p r_p$ (3.4b)

Note, r is used for density instead of the usual ρ

The phase density simply represents the mass of a particular phase present in a multi-phase mixture divided by the total volume of the mixture. In this work only two phases are treated, solid and gas. However, the analysis can easily be extended to treat three or more constituents [53].

Once the phase densities are defined [Eqs. (3.4)], the one-dimensional conservation equations for the separate phases can be expressed in Eulerian form as [38]:

Conservation of Mass

gas phase

$$\frac{\partial(r_1)}{\partial t} = \frac{-\partial(r_1 u_g)}{\partial x} + S_g \tag{3.5a}$$

solid phase

$$\frac{\partial(r_2)}{\partial t} = \frac{-\partial(r_2 u_p)}{\partial x} + S_p \tag{3.5b}$$

Conservation of Momentum

gas phase

$$\frac{\partial(r_1 u_g)}{\partial t} = \frac{-\partial(r_1 u_g u_g + P_g \phi_g)}{\partial x} + \bar{M}_g \tag{3.6a}$$

solid phase

$$\frac{\partial(r_2 u_p)}{\partial t} = \frac{-\partial(r_2 u_p u_p + P_p \phi_p)}{\partial x} + \bar{M}_p \tag{3.6b}$$

Conservation of Energy

gas phase

$$\frac{\partial(r_1 E_g)}{\partial t} = \frac{-\partial(r_1 E_g u_g + P_g u_g \phi_g)}{\partial x} + \bar{E}_g \tag{3.7a}$$

solid phase

$$\frac{\partial(r_2 E_p)}{\partial t} = \frac{-\partial(r_2 E_p u_p + P_p u_p \phi_p)}{\partial x} + \bar{E}_p \qquad (3.7b)$$

A detailed derivation of these equations (using a control volume analysis) can be found in a paper by Krier and Kezerle [38].

The term E_i in Eq. (3.7) represents the total energy (sum of kinetic plus internal) for the 'i'th phase. The product $(rE)_i$ is therefore the total energy per unit volume. Note that energy fluxes due to radiation and conduction are neglected in these equations. The source terms, $\bar{S}$, $\bar{M}$, and $\bar{E}$ appearing in Eqs. (3.5-3.7) will be discussed later.

One of the assumptions made in the separated-flow analysis is that the gas/solid mechanical mixture of the two phases, must itself be a continuum and be definable by the same general form of the flow equations as the separate phases [Eqs. (3.5-3.7)]. This assumption leads to three mixture constraints, namely,

$$\sum_i S_i = 0 \qquad (3.8a)$$

$$\sum_i \bar{M}_i = 0 \qquad (3.8b)$$

and, $$\sum_i \bar{E}_i = GE_{ch} \qquad (3.8c)$$

The (GE_{ch}) term appearing in Eq. (3.8c) is due to the chemical reactions occurring in the mechanical mixture. Thus, consistent with Eqs. (3.8a-3.8c), the interaction terms suggested for Eqs. (3.5-3.7) are

$$S_g = G \tag{3.9a}$$

$$S_p = -G \tag{3.9b}$$

$$\bar{M}_g = Gu_p - \mathcal{D} \tag{3.10a}$$

$$\bar{M}_p = \mathcal{D} - Gu_p \tag{3.10b}$$

$$\bar{E}_g = G(\frac{u_p^2}{2} + E_{ch}) - \dot{Q} - \mathcal{D}u_p \tag{3.11a}$$

and, $$\bar{E}_p = G(\frac{-u_p^2}{2}) + \dot{Q} + \mathcal{D}u_p \tag{3.11b}$$

In Eqs. (3.9 - 3.11) the term G represents the rate of mass generation per unit volume per unit time. It is given by

$$G = \frac{6}{d} r_2 (\frac{d\hat{x}}{dt}) \tag{3.12}$$

where d is the instantaneous particle diameter and $d\hat{x}/dt$ is surface burning rate given by Eq. (1.1). For this analysis all particles are assumed to be spheres. To treat nonspherical particles Eq. (3.12) would have to be modified in order to account for the increased surface-to-volume ratio.

The term $\mathcal{D}$ appearing in the equations above is an interphase (gas-solid) momentum transfer term due to viscous effects. It is expressed as [38]

$$\mathcal{D} = \frac{\mu_g}{(2d)^2} (u_g - u_p) \, f_{pg} \tag{3.13}$$

where f_{pg} is a nondimensional drag coefficient determined from experiments involving flow through packed beds of spherical beads [59].

$$f_{pg} = (\phi_p/\phi_g)^2 [276 + 5 \, (Re/(\phi_p))^{0.87}] \tag{3.14}$$

Here, Re represents the Reynolds number. Finally, $\dot{Q}$ represents the interphase convective heat transfer rate

$$\dot{Q} = \frac{6}{d} (1 - \phi_g) h_{pg} \, (T_g - T_p) \tag{3.15}$$

The heat transfer coefficient h_{pg} is [60]

$$h_{pg} = 0.65 \, [\frac{k_g}{d}] \, Re^{0.7} \, Pr^{0.33} \tag{3.16}$$

where k_g is the thermal conductivity of the gas, and Pr is the Prandtl number.

3.3 Mixture Equations

Summing the conservation of mass equations for both phases [Eqs. (3.5a-3.5b)], one obtains an expression for the conservation of mass for the mixture

$$\frac{\partial(r_m)}{\partial t} = \frac{-\partial(r_m u_m)}{\partial x} \tag{3.17}$$

where $r_m = r_1 + r_2$, $r_m u_m = r_1 u_g + r_2 u_p$. Here, the subscript 'm' refers to the mixture properties. The mixture velocity, u_m, appearing in the equations, represents a mass weighted average of the two phases.

Likewise, the mixture momentum equation is derived by combining Eqs (3.6a) and (3.6b) to obtain

$$\frac{\partial(r_m u_m)}{\partial t} = -\frac{\partial(r_m u_m u_m + P_m)}{\partial x} - \frac{\partial[r_1 r_2 (u_g - u_p)^2 / r_m]}{\partial x} \tag{3.18}$$

where P_m represents the mixture pressure, $P_m = \phi_g P_g + \phi_p P_p$. The term appearing in Eqs. (3.18) involving the product $(r_1 r_2)$ is a mixture inertial coupling term, similar to the one found in Soo's equations [60] for the separate phases.

Finally, after manipulating Eqs. (3.7a), (3.7b), and (3.12) the mixture energy equation takes the form

$$\frac{\partial(r_m E_m)}{\partial t} = -\frac{\partial(r_m E_m u_m + P_m u_m)}{\partial x}$$

$$-\frac{\partial(r_1 r_2(E_g(u_g - u_p) + E_p(u_p - u_g))/r_m)}{\partial x} \tag{3.19}$$

$$-\frac{\partial((u_g - u_p)(\phi_g P_g r_2 - \phi_p P_p r_1)/r_m)}{\partial x}$$

3.4 Entropy Inequality

Further investigation will show that the equations describing two-phase reactive flow derived in Section 3.2 do not violate the Second Law of Thermodynamics. First stated by Truesdell [54] and later modified by Nunziato and Walsh [53], the Second Law or Thermodynamics for a chemically reacting multiphase fluid is

$$\sum_i (r_i \frac{Ds_i}{Dt} + G_i s_i + \mathrm{div}(q_i/T_i) - r_i \bar{r}_i/T_i) \geq 0 \tag{3.20a}$$

where q_i represents conductive heat transfer and $\bar{r}_i$ radiative heat transfer to the 'i'th phase. The summation in Eq. (3.20a) is over all constituents 'i' present in the mixture. For our analysis Eq. (3.20a) reduces to

$$\sum_{g,p} (r \frac{Ds}{Dt} + Gs)_i \geq 0 \tag{3.20b}$$

The entropy s can now be eliminated from the total derivative by introducing the Helmholtz free energy, $\bar{a} = e - Ts$, to yield

$$\sum_{g,p} [((r(\dot{e} - \dot{a}) - \dot{T}s)/T)_i + (Gs)_i] \geq 0 \tag{3.21}$$

where (•) represents the substantial derivative

$$\frac{D(\;)}{Dt} \equiv \frac{\partial(\;)}{\partial t} + u\,\frac{\partial(\;)}{\partial x} \qquad (3.22)$$

The energy equation [Eqs. (3.7a) and (3.7b)] for each phase can be substituted into Eq. (3.21) to eliminate e, giving

$$\sum_{g,p} [\{(\overline{E} - P\phi\,\frac{\partial u}{\partial x} - r\dot{a} - r\Delta\dot{T}\,)_i\}/T_i + (G\Delta)_i] \geq 0 \qquad (3.23)$$

After some algebraic manipulation and recognizing the thermodynamic identity

$$P = r^2\,\frac{\partial a}{\partial r} \qquad (3.24)$$

Eq. (3.23) becomes

$$\sum_{g,p} [\{ - r\,(\frac{\partial a}{\partial \phi} - \frac{P}{r})\,\frac{D\phi}{Dt} + G(e - \overline{a} - r\frac{\partial a}{\partial r}) + \overline{E}\}/T]_i \geq 0 \qquad (3.25)$$

Expanding Eq. (3.25) and introducing the void-dependent equilibrium pressure [53] (to be discussed in Sec. 3.7),

$$P^e = \phi r\,\frac{\partial a}{\partial \phi} \qquad (3.26)$$

and the chemical potential [53]

$$\mu = \frac{\partial(ra)}{\partial r} \qquad (3.27)$$

eventually leads to

$$\left[\left(-(P - P^e)\frac{D\phi}{Dt} + G\left(e + \frac{u_p^2}{2}\right) - D u_p - \dot{Q}\right)/T\right]_g$$

$$+ \left[\left(-(P - P^e)\frac{D\phi}{Dt} - G\left(e + \frac{u_p^2}{2} - E_{ch}\right) + D u_p + \dot{Q}\right)/T\right]_p \geq 0 \quad (3.28)$$

In conclusion, Eq. (3.28) is a statement of the Second Law of Thermodynamics for the reactive two-phase flow being studied. This entropy inequality must be satisfied for all field locations at all times. Stated in another way, the specific relations for the interphase drag, heat transfer, and mass transfer stated earlier [Eqs. (3.9)-(3.11)] are constrained by the Second Law of Thermodynamics.

3.5 Equations of State

Up to this point in our analysis of two-phase reactive flow, we have introduced twelve unknowns $[(u,e,P,T,\phi,r)]_g$ and, $[(u,e,P,P,\phi,r)]_p$ and only seven independent equations. The independent equations include the conservations of mass, momentum, and energy for each phase [Eqs. (3.5-3.7)] and the volume fraction summation, Eq. (3.3).

In addition to the conservation equations, constitutive relations must be provided describing the thermodynamic state of the gaseous product phase and the unreacted solid phase. These include a P(v,T) relation and an e(v,T) relation. In order to be thermodynamically consistent, the suggested state equations must satisfy the Second Law of Thermodynamics reciprocal free energy relations

$$P = r^2 \left(\frac{\partial \bar{a}}{\partial r}\right)\Big|_T \qquad (3.29a)$$

and, $$e = a - T \left(\frac{\partial \bar{a}}{\partial T}\right)\Big|_v \qquad (3.29b)$$

where '$\bar{a}$' is the Helmholtz free energy, P is the thermodynamic pressure, r is the material density, e is the specific internal energy and T is the absolute temperature.

3.5.1 Solid Phase

The general form of the solid phase equation of state should contain two terms, one dependent on the intermolecular separation distance and one due to the kinetic motion of the molecules [54].

$$P(v,T) = P_1(v)+P_2(T) \qquad (3.30)$$

A similar model suggested by Zel'dovich [27] contains a third term due to electronic excitation. However, such a term only becomes important at extremely high temperatures (T > 20,000 K).

A suggested form of the P(v,T) equation of state for the solid phase is [15]

$$P_p = [r^2\{f'(r) + \bar{G}(v)C_v(T - T_o)/r\}]_p \qquad (3.31)$$

The subscript 'p' indicates that all terms inside the brackets are for the solid phase. In Eq. (3.31) $\bar{G}(v)$ represents the Gruneisen coefficient defined as the thermodynamic derivative

$$\bar{G}(v) = \frac{1}{v}\left(\frac{\partial P}{\partial e}\right)\Big|_v \tag{3.32}$$

and the function $f'(r)$ represents the isotherm passing through the ambient state $(r,P,T)_o$. The caloric equation of state consistent with Eq. (3.32) is

$$e_p = [f(r) - \bar{G}(v)C_v \ln(r/r_o)T_o + C_v(T-T_o)]_p \tag{3.33}$$

and the defining free energy function is

$$\begin{aligned} a_p = [&f(r) + \bar{G}(v)C_v \ln(r/r_o)(T-T_o) \\ &+ C_v(T_o \ln(T/T_o) + T - T_o)]_p \end{aligned} \tag{3.34}$$

Shock impact experiments conducted at Los Alamos National Laboratory (LANL) have provided the shock velocity-particle velocity data (U_s, u_p) for HMX shown in Fig. 3.1 [55]. A least squares fit yields

$$U_s(\text{cm/s}) = c_o + Su_p \tag{3.35}$$

with $c_o = 3.07 \times 10^5$ cm/s and $S = 1.79$. This expression is valid for shock pressures less than 40 GPa, values well within the scope of this work. In fact, many solid materials exhibit linear shock velocity-particle velocity profiles for shock pressures in this range [55]. If the U_s, u_p data is indeed linear, then Eq. (3.35) along with the Rankine-Hugoniot jump conditions yields a general expression for the P,v shock Hugoniot given by

$$P_H(r) = r_{po} c_o^2 R/(1-SR)^2 \tag{3.36}$$

where, $R = 1 - r/r_{po}$ (3.37)

An ordinary differential equation for the potential function f(r) can be determined by combining Eqs. (3.31), (3.33), (3.36) and an expression for the internal energy along the Hugoniot, (Eq. 1.7). It is given as [15]

$$f'(r) = \{\bar{G}(v) f(r)/C_v - \bar{G}(v)^2 C_v \frac{T_o}{r} \ln(r/r_o) + \frac{r_o c_o^2 (1 - r_o/r)}{r^2 [1 - S(1 - r_o/r)]^2} [1 - \frac{\bar{G}(v)}{2} (\frac{r}{r_o})(1 - \frac{r_o}{r})]\}_p \tag{3.38}$$

Baer [15] has solved Eq. (3.38) using as a boundary condition a=0 at $r/r_{po}=0$. The resulting polynomial for HMX is

$$f(x) = 7.757x^2 + 13.33x^3 + 18.04x^4 + 2.828x^5 + 24.01x^6 + 278.3x^7 + 383.6x^8 \tag{3.39}$$

where, $x = (r/r_o - 1)_p$

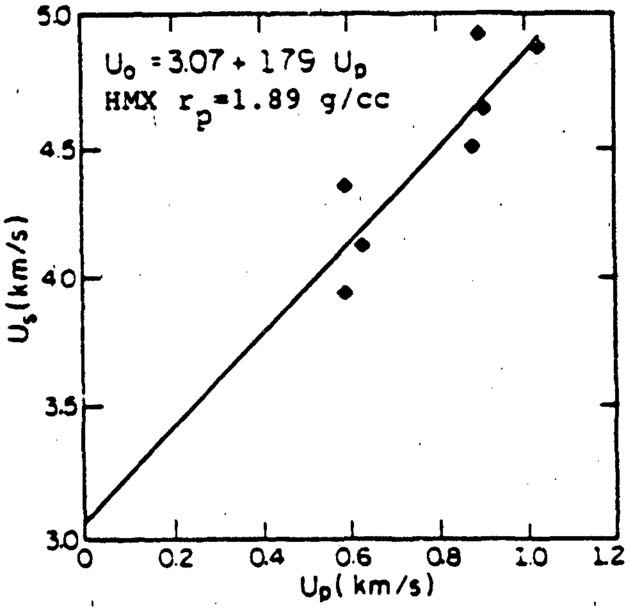

Figure 3.1 Shock velocity - particle velocity shock Hugoniot for HMX (r_p=1.89 g/cc). Taken from Ref. 55.

Thus, the P(v,T), Eq. (3.31) and e(v,T), Eq. (3.33) equations of state for the solid phase are complete.

3.5.2 Gas Phase

An equation of state for the products of both combustion and detonation must accurately describe the state of a mixture of gases over a wide range of densities. A typical value for the gas density at the CJ-plane is of the order of the condensed phase reactants (1.9 g/cc for HMX). In addition, the product gases generated in a detonation eventually expand to atmospheric density. For this reason, a single P(v,e) equation of state must cover a rather large density range.

In the work presented here, a simple nonideal equation of state taking a form similar to the Noble-Abel equation of state was used for the detonation products. Here it is assumed that,

$$P_g = r_g \hat{R}_g T_g (1+n' r_g) \qquad (3.40)$$

The covolume term n' was chosen so that the equation properly defines the thermodynamic state at the CJ point as predicted when using the TIGER [62] thermochemical code. For HMX with an initial loading density r_2=1.33 g/cc, TIGER calculations yield a CJ pressure P_{CJ}=17.1 GPa, CJ temperature T_{CJ}=4303K and CJ density r_{CJ}=1.70 g/cc. Assuming a constant specific heat and product molecular weight, M=27.81 g/g-mol, this yields a covolume

$$n' = 3.60 \text{ cc/g} \qquad (3.41)$$

Values for CJ pressure, temperature and density for other loading densities are given in Table 5.1.

A caloric equation of state e(v,T) consistent with Eq. (3.41) is determined by first expressing the total derivative of e(v,T) as

$$de = (\partial e/\partial v)_T \, dv + (\partial e/\partial T)_v \, dT \qquad (3.42)$$

Assuming a constant C_v and using Maxwell's relations gives

$$de = C_v dT + \{T(\partial P/\partial T)_v - P\} \, dv \qquad (3.43)$$

Now substituting in Eq. (3.40) gives the appropriate caloric equation of state

$$de = C_v dT + \{T(\hat{R}r)(1 + n'r) - \hat{R}Tr(1 + n'r)\}$$

$$\text{or,} \quad de = C_v dT \qquad (3.44)$$

Finally, integrating from (v ,T) to (v,T) gives

$$e(v,T) - e(v_o, T_o) = C_v(T - T_o) \qquad (3.45)$$

Through the reciprocity relations defined earlier [Eqs. (3.29a), (3.29b)] Eqs. (3.40) and (3.44) yield the free energy function

$$\bar{a}_g = [\hat{R}\,T\,\ln(r/r_o) + \hat{R}\,T\,n'\,r + C_v(T_o \ln(T/T_o) + T_o - T)]_g \qquad (3.46)$$

3.6 Interphase Force Balance

In Sec. 3.2 the equations of motion were developed for two-phase reactive flow using a separated-flow analysis. It was assumed that each phase (solid,gas) is itself a continuous body and the two phases are coupled through interphase mass, momentum and energy transfer terms. Therefore, equations of state were developed for the gas phase $P_g = P_g(T_g, v_g)$ in Sec. 3.5.1 and for the solid phase $P_p = P_p(T_p, v_p)$ in Sec. 3.5.2. Up to this point in the analysis the granular nature of the solid phase has been neglected and the flow behavior of each phase has been modeled as a simple compressible fluid.

Since the compressibility of the gas/solid mechanical mixture is void-volume dependent [63], it is desirable to develop a constitutive relation relating the stress on the granular matrix to the change in void volume (compaction).

Research in the area of mathematically modeling the equilibrium stress of a material under an applied external load is well documented [64,65]. The term equilibrium stress was defined in Eq. (3.25). In the work presented here, the matrix of packed grains is treated as a single hollow sphere where the inner and outer radii are chosen such that the overall porosity of the material is properly represented. The pore collapse is assumed to occur in three phases: (1) an elastic phase: (2) an elastic-plastic phase, where plastic deformation begins at the outer radius and progresses towards the center: and (3) a plastic phase where plastic deformation occurs throughout. The mathematical relations between equilibrated stress P^e and void porosity 'a' for the three phases of compaction and the appropriate range over which each occurs are given by [64]

<u>elastic phase</u> $a_o \geq a > a_1$

$$P^e = \frac{4G'(a_o - a)}{3a(a - 1)} \tag{3.47}$$

<u>elastic-plastic phase</u> $a_1 \geq a > a_2$

$$P^e = \frac{2}{3} Y \{1 - \frac{2G'}{Ya} (a_o - a) + \ln [\frac{2G'(a_o - a)}{Y(a - 1)}]\} \tag{3.48}$$

<u>plastic phase</u> $a_2 > a > a$

$$P^e = \frac{2}{3} Y \ln (\frac{a}{a - 1}) \tag{3.49}$$

where the limits between the phases are given by

$$a_1 = (2G'a_o + Y)/(2G' + Y) \tag{3.50}$$

and, $a_2 = (2G'a_o)/(2G' + Y)$ (3.51)

In Eqs. (3.47-3.51) Y and G' are the yield strength and shear modulus respectively. Values for Y and G' can be found in Table 5.2.

Figure 3.2 illustrates the P^e - a relationship for HMX at various initial densities. For example, a sample with an initial density of r_2 =1.58 g/cc (a =1.20) will transition from elastic deformation to elastic-plastic deformation at approximately P^e = 0.015 GPa and then to plastic deformation at P^e = 0.031 GPa. As shown in the figure, there is very little volume change prior to the transition to fully plastic deformation.

One can now write a static force balance between the gas-phase pressure P_g, the solid-phase stress P_p, and the equilibrated stress.

$$P_p = P_g + P^e \tag{3.52}$$

Equation (3.52) equates the thermodynamic stress in the solid phase, P_p, to the sum of the equilibrated stress, P^e, plus the gas phase pressure, P_g. The the term P_p represents stress due to 'compression' of the solid while P^e represents stress due to 'compaction' of the granular solid.

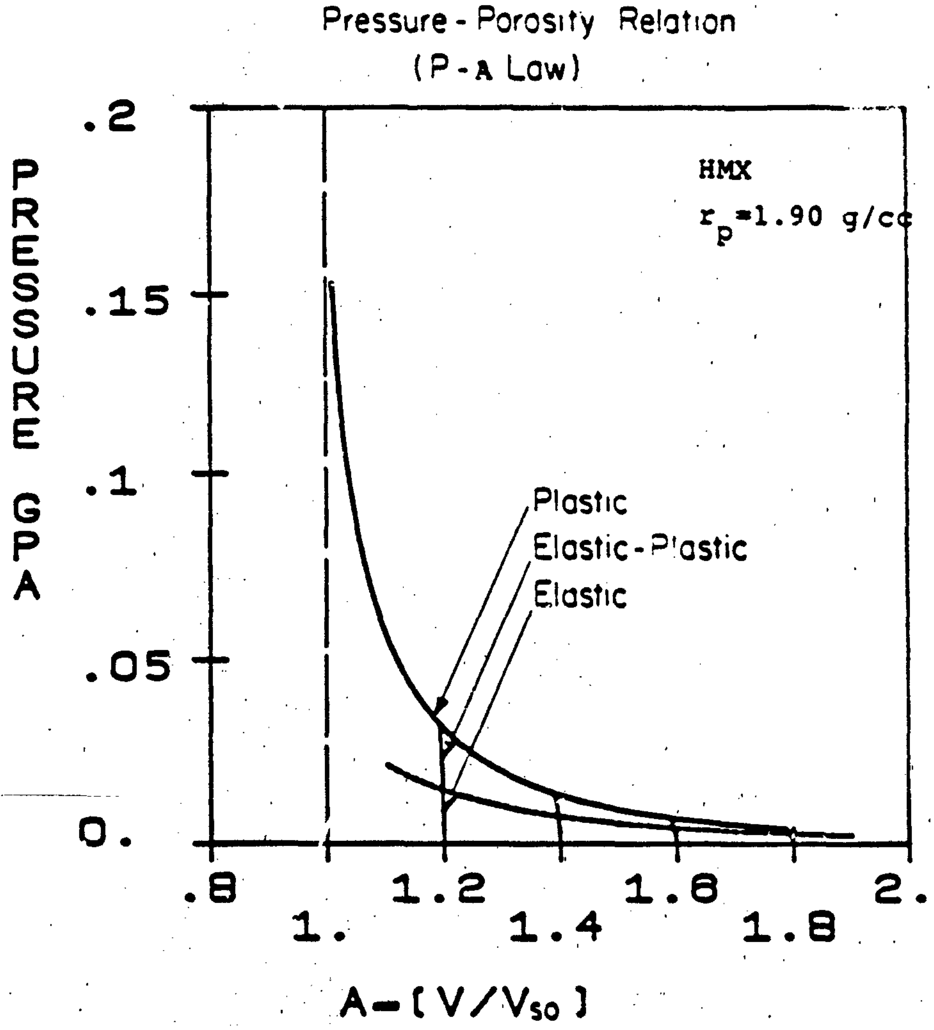

Fig. 3.2 Pressure-void volume relation -ship for porous HMX.

CHAPTER 4

NUMERICAL SOLUTION TECHNIQUE

4.1 Introduction

The governing equations derived in the previous chapter [Eqs. (3.5 - 3.7)] form a system of six nonlinear hyperbolic partial differential equations (PDEs). They can be written in vector form as:

$$\frac{\partial \overline{U}}{\partial t} + \frac{\partial F(\overline{U})}{\partial x} = \overline{S} \tag{4.1}$$

where, $$\overline{U} = [r_1, r_2, r_1 u_g, r_2 u_p, r_1 E_g, r_2 E_p] \tag{4.2a}$$

$$\begin{aligned} F(\overline{U}) = [&r_1 u_g, r_2 u_p, (r_1 u_g^2 + P_g \phi_g), (r_2 u_p^2 + P_p \phi_p), \\ &(r_1 u_g E_g + P_g u_g \phi_g), (r_2 u_p E_p + P_p u_p \phi_p)\ ] \end{aligned} \tag{4.2b}$$

and,

$$\begin{aligned} \overline{S} = [&G, -G, Gu_p - \mathcal{D}, \mathcal{D} - Gu_p, \dot{Q} - \mathcal{D}u_p + G(u_p^2/2 + E_{ch}) \\ &, \mathcal{D}u_p - \dot{Q} - G(u_p^2/2)] \end{aligned} \tag{4.2c}$$

Equations (4.1) describe one-dimensional, two-phase reactive flow with heat transfer by conduction and radiation neglected. <u>Intraphase</u> viscous effects are also neglected. The vector $\overline{U}$

contains the conserved variables, $F(\overline{U})$ the flux terms and $\overline{S}$ the interphase transport terms for mass, momentum and energy.

It should be noted that when a strong shock is present in the flow field, an additional constraint is imposed on the analysis. The Rankine-Hugoniot jump conditions [Eqs. (1.2),(1.3) and (1.7)] must be satisfied across the shock discontinuity in addition to Eqs. (4.1) . This constraint, together with the inviscid conservation equations, yields the proper increase in entropy across the shock front. When a shock is not present the conservation equations alone define the flow behavior, although, the Second Law of Thermodynamics still requires that entropy increases or is constant.

Due to the nonlinear source/sink terms, a closed analytic solution to the PDEs governing two-phase reactive flow is not possible. However, with known initial and boundary conditions one can solve the system of nonlinear equations by an appropriate finite difference technique.

4.2 Finite Difference Grid

The numerical solution to Eqs. (4.1) is determined by first discretizing the physical space domain into a finite number of grids, each a constant Δx in length. This is illustrated in Fig. 4.1 .

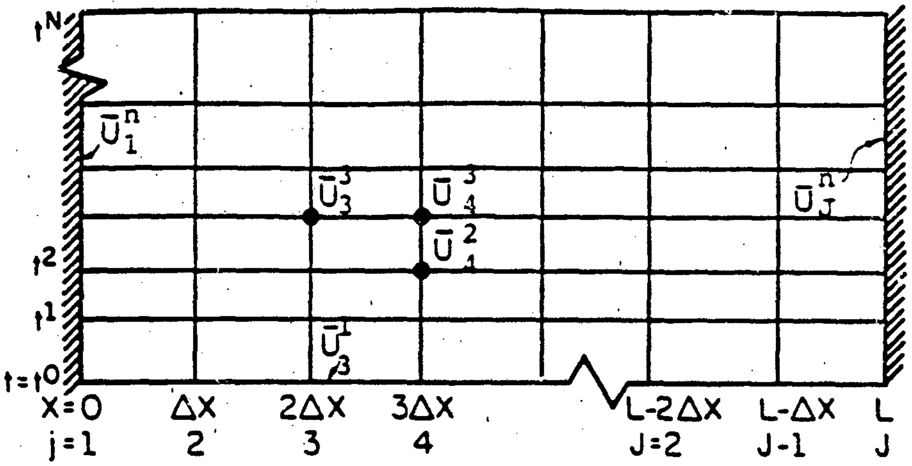

Fig. 4.1 Time-distance finite difference grid

At each nodal point 'j', the distance from the origin (j=1) can be expressed as $x_j = [(j-1)\ \Delta x]$ where j = 1,2,...J . In a similar manner, time is discretized as $t^{n+1} = t^n + \Delta t^n$ where, n = 0,1,...N . Here Δt^n represents a finite step in time. In Fig. 4.1 U_j^n represents a value of the vector $\bar{U} = [r_1, r_2, r_1u_g, r_2u_p, r_1E_g, r_2E_p]$ located at the space-time coordinate $[(j-1)\Delta x, t^n]$. It is assumed that the vector $\bar{U}$ is known for all spatial locations x_j at an initial time t^o . In addition, boundary conditions for $\bar{U}$ at x=0 and x=L $(U_1^1, U_1^2, U_1^3, \ldots U_1^n$, and $U_J^1, U_J^2, \ldots U_J^n)$ are known for all time $0 < t < T$. In the work presented here the boundaries are assumed rigid, permeable and adiabatic. These assumptions yield the following boundary conditions.

$$dP/dx\Big|_o = dP/dx\Big|_L = 0 \qquad (i = 1,2) \qquad (4.3a)$$

$$u_i\Big|_o = u_i\Big|_L = 0 \qquad (i = g,p) \qquad (4.3b)$$

$$de_i/dx\Big|_o = de_i/dx\Big|_L = 0 \qquad (i = g\ p) \qquad (4.3c)$$

Using a second-order, center-differenced finite difference approximation, Eqs. (4.3a - 4.3c) can be written as,

$$(p_i)_{j=0}=(p_i)_{j=2} \quad \text{and} \quad (p_i)_{j=J+1}=(p_i)_{j=J-1} \quad (i=1,2) \qquad (4.4a)$$

$$(u_i)_{j=0} = (u_i)_{j=J} = 0 \qquad (i = g,p) \qquad (4.4b)$$

and, $(e_i)_{j=0}=(e_i)_{j=2}$ and $(e_i)_{j=J+1}=(e_i)_{j=J-1}$ $(i=g,p)$ (4.4c)

In the equations above $j=0$ and $j=J+1$ represent 'fictitious' nodal points necessary for evaluating the x-derivatives at $x=0$ and $x=L$.

In the following section a finite difference numerical technique will be used to approximate the governing differential equations [Eqs. (4.1)], thus, providing a method to march the solution [$\overline{U}$] in time. Appendix B lists the step-by-step procedure followed to solve the equations.

4.3 Numerical Technique

A method of lines (MOL) technique [56] was used to solve the system of nonlinear partial differential equations on a high speed computer (CYBER-175). Assuming that the vector $\overline{U}$ is known for all x_j at time t^n, the first step in the MOL approach is to express the continuous x-derivatives as discrete finite differences at each of the 'j' locations. The symbol δ_{ix} will be used to represent an 'i'th order finite difference approximation to the derivative d( )/dx . The second and fourth order center-differenced algorithms are given by

$$\delta_{2x}F(\bar{U}) = (F(u)^n_{j+1} - F(u)^n_{j-1})/2\Delta x + \mathcal{O}(\Delta x^2) \tag{4.5a}$$

and,
$$\delta_{4x}F(\bar{U}) = \frac{(-8F(u)^n_{j+2} + F(u)^n_{j+1} - F(u)^n_{j-1} + 8F(u)^n_{j-2})}{12\Delta x} + \mathcal{O}(\Delta x^4) \tag{4.5b}$$

respectively. In this analysis the second order scheme was used. Using Eqs. (4.5) to express the continuous x-derivatives in Eqs. (4.1) as finite differences, the system of PDEs at time t^n are reduced to a system of ODEs. They are given by

$$dr_1/dt = f(\bar{U}^n_j, \bar{U}^n_{j+1}, \bar{U}^n_{j-1}) \tag{4.6a}$$

$$dr_2/dt = f(\bar{U}^n_j, \bar{U}^n_{j+1}, \bar{U}^n_{j-1}) \tag{4.6b}$$

$$d(r_1u_g)/dt = f(\bar{U}^n_j, \bar{U}^n_{j+1}, \bar{U}^n_{j-1}) \tag{4.7a}$$

$$d(r_2u_p)/dt = f(\bar{U}^n_j, \bar{U}^n_{j+1}, \bar{U}^n_{j-1}) \tag{4.7b}$$

$$d(r_1E_g)/dt = f(\bar{U}^n_j, \bar{U}^n_{j+1}, \bar{U}^n_{j-1}) \tag{4.8a}$$

and
$$d(r_2E_p)/dt = f(\bar{U}^n_j, \bar{U}^n_{j+1}, \bar{U}^n_{j-1}) \tag{4.8b}$$

Appendix B lists the complete form of Eqs. (4.6 - 4.8). Once the PDEs are reduced to ODEs at time t^n , the solution is advanced in time to t^{n+1} by solving the system of ODEs over the time increment $t^n \rightarrow t^{n+1}$.

Depending on the rate of chemical reaction, the system of ODEs [Eqs. (4.6 - 4.8)] can either be 'stiff' or 'nonstiff'. The term stiff refers to ODEs which have greatly differing decay time-constants [66]. Early in the DDT process the convective derivative time-constants are of the same order as those describing the solid to gas decomposition. In this regime no single term dominates the behavior of the flow equations and hence, they can be considered nonstiff. However, as the DDT developes, the reaction rate increases drastically and the chemical reaction terms in the governing equations dominate the flow behavior. When this occurs, the 'standard' ODE solvers are forced to take very small internal time increments in order to preserve stability. To be more efficient one would prefer a numerical technique that can identify and treat stiff ODEs by optimizing the internal time step.

Three different solution techniques were tested on Eqs. (4.6 - 4.8) . They include; a fifth order Runge-Kutta technique, Gear's backward differentiation formulae (BDF) and, an Adams technique. References 66 and 67 provide more information on these techniques. In brief, the Adams method (Subroutine ODE [68]) is a predictor-corrector solution technique where the predictor cycle is explicit and the corrector is implicit. The Runge-Kutta technique used (Subroutine RKF45 [68]) is a modified version of the classical explicit Runge-Kutta [67] method, and Gear's BDF method (Subroutine DGEAR [69]) is a multi-step algorithm for stiff ODEs.

For comparison purposes, the three different methods were used to solve a 'baseline case'. The input data for the case is listed in Table 5.2 . This particular set of initial conditions was selected since one can show that it represents flow behavior which begins as a slow burning convective ignition front and eventually makes a transition to a steady-state detonation wave. The test case is introduced here only to make a comparison between the different ODE solvers. Further details of the steady-state parameters predicted for this case and a comparison with experimental data can be found in Chapter 5 .

Each of the numerical algorithms was used to solve the baseline case from $t=0$ to $t=38.2$ μs. At $t=38.2$ μs the steady-state detonation wave had reached the $x=L$ boundary and the program was terminated. In Table 4.1 a comparison of pressure, density and velocity at $t= 30.2$ μs (382 time step cycles) is given. The three show excellant agreement with each other and all three techniques satisfy the theoretical steady-state detonation solution. Regarding execution time, the Runge-Kutta took 116 cpu seconds, the Adams method took 138 cpu seconds and Gear's method took 107 cpu seconds. For comparison purposes with other machines, all were run on a Cyber-175 which computes approximately 5.5 million instructions per second.

The comparison shown in Table 4.1 does not imply that the

TABLE 4.1: Comparison of ODE solver (t=30.2 μs)

x(cm)	0	2	4	6	8	10	12	14	16	18	20	
ρ_g (g/cc)	1.034	1.099	1.134	1.196	1.321	1.485	1.612	.001	.001	.001	.001	Adams
	1.033	1.097	1.133	1.194	1.317	1.485	1.646	.001	.001	.001	.001	Gear
	1.034	1.097	1.133	1.194	1.317	1.479	1.660	.001	.001	.001	.001	R-K
P_g (GPa)	4.622	4.607	4.699	5.364	7.060	9.990	16.03	0	0	0	0	Adams
	4.609	4.613	4.700	5.347	7.018	9.937	16.01	0	0	0	0	Gear
	4.608	4.608	4.701	5.351	7.022	9.879	15.90	0	0	0	0	R-K
u_g (m/s)	0	-14	0	152	509	1019	2084	11	0	0	0	Adams
	0	-8	6	155	505	996	2010	18	0	0	0	Gear
	0	-11	3	153	502	1004	1961	21	0	0	0	R-K

finite difference solutions are 'consistent' with the exact analytic solution. It simply shows that the three methods are 'self-consistent' and that Gear's BDF is the most efficient for the problem posed. Since there does not exist an exact analytic solution to the two-phase reactive flow equations, one cannot make a statement regarding the solutions consistency. However, by reducing the governing equations to a system which can be solved analytically, one can make implications about the merits of using the MOL technique. This was done in Ref. 56 where the Riemann shock tube problem was solved for a polytropic gas using the MOL method. The governing equations for the Riemann shock tube problem are the one-phase, nonreactive version of Eqs. (4.1) . The results from the finite difference MOL technique were in close agreement with the analytic solution to this problem.

In addition to the three methods discussed here, a Lax-Wendroff two-step scheme and a second-order MacCormack predictor-corrector method were also tested. As shown in a recent review article by Sod [70], the solution calculated by both methods develop stability problems.

4.4 Artificial Viscosity

The artificial dissipation inherent in the finite difference approximation to the Euler equations is sufficient to smooth out small oscillations and energy cascades present in flows not involving strong shocks [71]. However, if a strong shock is present an additional term should be included in the finite difference form of the equations. It should be representative of the entropy increase associated with a shock wave and act to damp out oscillations occurring in the flow.

Artificial viscosity was first included in the Lagrangian form of the conservation equations as a means of stabilizing the numerical solutions to flow analyses involving shock waves [71]. The viscous term suggested was

$$q = - \frac{(\bar{c}\Delta x)^2}{V} \frac{\partial V}{\partial t} \left| \frac{\partial V}{\partial t} \right| \qquad (4.9)$$

In Eq. (4.9) the term $\bar{c}$ is a constant $0 < \bar{c} < 1$.

The 'viscous pressure' q was added to the thermodynamic pressure , P, in the momentum and energy equations. Thus, terms like dP/dx took the form d(P + q)/dx. The dV/dt dependency of Eq. (4.9) indicates that the viscous pressure is much greater in the vicinity of shock waves than in compression waves which have slow strain and relaxation rates.

In the work presented here, artificial viscosity was included in the Eulerian form of the governing equations as a second order finite difference [56]

$$\frac{\partial \bar{U}}{\partial t} + \frac{\partial F(\bar{U})}{\partial x} = \bar{S} + \frac{\partial}{\partial x} \left(\hat{a}\Delta x \frac{\partial \bar{U}}{\partial x}\right) \qquad (4.10)$$

where the viscosity term is approximated by

$$\frac{\partial}{\partial x}\left(\hat{a}\Delta x\,\frac{\partial \overline{U}}{\partial x}\right) = P^{n}_{j+\frac{1}{2}} - P^{n}_{j-\frac{1}{2}} \tag{4.11}$$

and where,

$$P^{n}_{j+\frac{1}{2}} = (\hat{a}_{j+1} + \hat{a}_{j})^{n}(\overline{U}_{j+1} - \overline{U}_{j})/2\Delta x \tag{4.12}$$

with $\hat{a}^{n}_{j} = (u + c)^{n}_{j}$ (4.13)

4.5 Entropy Production in a Shock Wave

In addition to eliminating the oscillations inherent in the numerical technique, there are several reasons based on physical arguments for including the viscous pressure term in what appears to be a correct finite difference approximation to the actual differential equations. This section is included to outline some of the reasons for including artificial viscosity in the numerical model.

As stated earlier, the governing equations include no viscous effects. An interphase momentum transfer term appears in the variable $\overline{M}$ [see Eq. (3.10)], dependent on the relative phase velocities, but intraphase viscous effects are simply neglected. This assumption is valid as long as the rate of volume deformation in the gas is low. However, within the thickness of a shock wave, the strain rate is extremely high and viscous effects play an important role in determining the shock structure. Because of this, Eqs. (4.1) must be modified in the region of the shock front to include viscous energy dissipation.

Begin by considering a very limiting form of the conservation equations for one-dimensional flow where viscosity, conduction, radiation and chemical reaction are neglected.

$$\frac{\partial r}{\partial t} + \frac{\partial (ru)}{\partial x} = 0 \qquad (4.14)$$

$$\frac{\partial (ru)}{\partial t} + \frac{\partial (P + ru^2)}{\partial x} = 0 \qquad (4.15)$$

$$\frac{\partial (rE)}{\partial t} + \frac{\partial (Pu + ruE)}{\partial x} = 0 \qquad (4.16)$$

Along with an equation of state, $P=P(v,e)$, Eqs. (4.14 - 4.16) completely define the flow behavior of a constant entropy process. When a shock wave is present in the flow field the flow is no longer reversible. Hence, to be correct, the entropy increase across the shock wave must be included in the defining equations. By including a viscous pressure term, q, with the same strain rate dependency as Eq. (4.9), the entropy increase in the shock wave can be properly modeled.

Including q, the governing equations take the form

$$\frac{\partial r}{\partial t} + \frac{\partial (ru)}{\partial x} = 0 \qquad (4.17)$$

$$\frac{\partial (ru)}{\partial t} + \frac{\partial ((P + q) + ru^2)}{\partial x} = 0 \qquad (4.18)$$

and $$\frac{\partial (rE)}{\partial t} + \frac{\partial ((P + q)\ u + ruE)}{\partial x} = 0 \qquad (4.19a)$$

The 'new' energy equation [Eq. (4.19a)] can be rewritten for a Lagrangian cell as [72]

$$de = -(P+q)\,dv \qquad (4.19b)$$

Equating Eq. (4.19b) to the First Law of Thermodynamics

$$de = Tds - Pdv \qquad (4.20)$$

yields

$$Tds = -qdv \qquad (4.21)$$

or,

$$\dot{e}_i = -q\dot{v} \qquad (4.22)$$

where the subscript 'i' refers to the irreversible shock process. Integrating Eq. (4.22) from the initial state to the shock state yields

$$\int_{e_o}^{e_s} de_i = -\int_{v_o}^{v_s} q\,dv \tag{4.23}$$

or,

$$(e_s - e_o)_i = -\int_{v_o}^{v_s} q\,dv \tag{4.24}$$

Equation (4.24) is an expression for the amount of energy available to irreversibly heat the shocked material. The right hand side can be evaluated in the computer program at each x-location and compared to the irreversible work, $(e_s - e_o)_i = \int T ds$, which can be calculated from known shock Hugoniot data [73]. If the two are equivalent, the 'artificial' term q is accurately modeling the entropy production in the shock process.

CHAPTER FIVE

Results

5.1 Introduction

Proposed in Chapter 1, Section 1.3, were three different scenarios describing DDT in condensed propellants/explosives. Although the predetonation events are different for each proposed scheme, the final solution, a steady state detonation, is the same for all three. Two of the three cases, DDT-Case 1 and DDT-Case 2 will be examined in more detail in this chapter. The finite difference numerical method developed in Chapter 4 will be used to integrate the time dependent PDEs governing the flow behavior and the results obtained from the computer code will be compared with theoretical steady state detonation solutions. In addition, experimental data from outside sources will be introduced for comparison with the computer predictions.

Table 5.1 presents data for CJ pressure, CJ temperature, CJ density, covolume n' and detonation velocity D for HMX explosive at various initial densities. The initial loading density was defined in Eq. 3.4b as

$$r_2 = \phi_p r_{po} \qquad \text{or, } r_2 = r_{po}/a_o \qquad \text{since, } a_o = 1/(1-\phi_{go})$$

The data in Table 5.1 is for the density range 1.20 g/cc $< r_2 <$ 1.90 g/cc where the upper limit represents crystalline HMX ($\phi_{go} =$ 0.0, $a_o = 1.0$). These data were calculated using the TIGER chemical

TABLE 5.1: CJ Parameters (P,T,v,D from TIGER)

ϕ_{go}	a_o	r_2(g/cc)	P_{CJ}(GPa)	T_{CJ}(K)	v_{CJ}(cc/g)	D(mm/μs)	n´(cc/g)
0	1	1.90	36.57	3840	.4067	9.20	4.86
.06	1.06	1.80	32.25	3973	.4260	8.77	4.50
.11	1.12	1.70	28.50	4083	.4471	8.35	4.22
.16	1.19	1.60	25.20	4171	.4707	7.98	4.00
.21	1.27	1.50	22.22	4236	.4973	7.65	3.84
.26	1.36	1.40	19.62	4280	.5276	7.33	3.74
.32	1.46	1.30	17.26	4304	.5629	7.05	3.68
.37	1.58	1.20	14.92	4337	.6064	6.76	3.61

equilibrium computer code developed at SRI International [62]. Each set of thermodynamic properties (P,v,T) represents the CJ state for the specified initial density r_2 . The TIGER code computes the CJ state from information about the unreacted shock Hugoniot, chemical formula of the condensed explosive, and equation of state for each of the product gases [74]. Throughout Chapter 5 the steady state solutions predicted by the DDT code will be compared with the TIGER data in Table 5.1 .

5.2 DDT-CASE 1

The test configuration (Fig. 1.2) for DDT-Case 1 consists of a bed of propellant grains, tightly packed ($a_o < 1.67$) in a steel tube. Prior to ignition at $x=0$, the bed has a uniform distribution of unisized spheres. The reader is referred to Section 1.3 for a review of this particular DDT process. Whether or not the accelerating deflagration wave actually makes a transition to a steady state detonation depends on the properties of the material and the initial conditions. A few of the parameters which determine whether a DDT event will take place include; propellant density r_{po}, initial loading density r_2, propellant chemical energy E_{ch} , bed confinement ϕ_{go} , burning rate $d\ell/dt$, bed length L, igniter strength, and initial grain size d_o . No single parameter alone can be regarded as the most critical factor in determining whether a DDT will occur. For example, a confined bed of small, high-energy, tightly-packed grains provides the ideal pressure-rise rate for a DDT, however, if the bed is shorter than the critical detonation run-up distance ℓ_{CJ} a detonation cannot occur. The granular bed would experience a rapid overpressurization but it would not detonate.

To test the DDT computer code we chose to model the well-documented experimental work of Bernecker and Price [7,8,32,75]. Computer output for four sample cases predicting a DDT outcome will be discussed in this section. Common input data for the four sample runs can be found in Table 5.2 . The material being studied is HMX [73] and the initial grain size is d_o=200 μm. Throughout the remainder of this chapter, the four cases will be referred to as Case 1A, Case 1B, Case 1C and Case 1D. With the exception of initial gas porosity ϕ_{go}, the input data is the same for all four cases. Cases 1A-1D have initial porosities of ϕ_{go} =0.32, 0.26, 0.37, and 0.30 respectively. Values predicted by the DDT code for CJ pressure, CJ temperature, CJ density, and detonation velocity will be compared with TIGER data [62] and the initiation front x,t locus will be compared with experimental data [75].

The predicted gas pressure, gas velocity, porosity and gas generation rate profiles for Case 1A (ϕ_{go}=0.32) are shown in Figs. 5.1a-5.1d respectively. For this particular case the rate of product gas generation is extremely rapid and the accelerating deflagration wave makes a transition to a steady state detonation 10 cm from the ignition source (x=0). The rapid pressure rise during the deflagration phase is due in part to the high surface-to-volume ratio of the very small (d_o=200 μm) propellant grains. It should be noted that the initial particle size does

TABLE 5.2 INPUT DATA FOR CASES 1A, 2A, 3A and 4A

Bed length $L = 20$ cm

Burning rate index $n = 1.00$

Burning rate coefficient $b = (0.002)(\mathrm{cm/s})\ (1.45\times10^{-4})\ \mathrm{Pa}^{-1}$

Gas specific heat at constant volume $C_{vg} = 1.77\times 10^{7}$ erg/g-K

Solid specific heat at constant volume $C_{vp} = 1.5 \times 10^{7}$ erg/g-K

Chemical energy $E_{ch} = 5.84 \times 10^{10}$ erg/g

Gruneisen coefficient at (P_o, r_o, T_o) $G_o = 1.10$

Shock velocity-Particle velocity hugoniot slope $S = 1.79$

Solid phase sound velocity at (P_o, r_o, T_o) $C_o = 3.07 \times 10^{5}$ cm/s

Number of cells $N = 200$

Solid density $r_p = 1.90$ g/cc

Yield strength $Y = 3.52 \times 10^{10}$ dy/cm^2

Initial pressure $P_o = 1.0 \times 10^{6}$ dy/cm^2

Initial temperature $T_o = 300°$ K

Initial grain size (spheres) $d_o = 200$ μm

Initial porosity Case 1A $\phi_o = 0.32$, $a_o = 1.46$

Initial porosity Case 1B $\phi_o = 0.26$, $a_o = 1.35$

Initial porosity Case 1C $\phi_o = 0.37$, $a_o = 1.59$

Initial porosity Case 1D $\phi_o = 0.30$, $a_o = 1.43$

not alter the final detonation state. However, it clearly effects the predetonation pressure-rise rate and the detonation run-up length.

Figure 5.1a illustrates the gas pressure profiles (P,x) for Case 1A at time increments of 5 µs. The CJ pressure is calculated from the computer output to be P_{CJ}=16.9 GPa and the steady state detonation velocity is D=7.01 mm/µs. Case 1A also predicts values of T_{CJ}=4289 K and v_{CJ}=0.568 cc/g. These and other data can be found in Table 5.3 . The DDT code values compare favorably with the TIGER chemical equilibrium predictions of P_{CJ}=17.26 GPa and D=7.05 mm/µs . TIGER predictions are the result of a chemical equilibrium calculation involving the detonation product gases. The code also includes solid carbon in oxygen deficient explosives (i.e., TNT). It has been thoroughly tested for detonating homogeneous explosives and is well accepted in the explosives community.

In addition to the computer calculated CJ properties being in agreement with the theoretical CJ properties, the expansion wave following the steady state detonation should satisfy certain fundamental relations of fluid mechanics. In particular, any state along the expansion wave is related to the CJ point by Eq. (1.14),

$$P/P_{CJ} = \left[1 + \frac{(\gamma - 1)}{2} \frac{(u - u_{CJ})}{c_{CJ}}\right]^{\frac{2\gamma}{(\gamma-1)}}$$

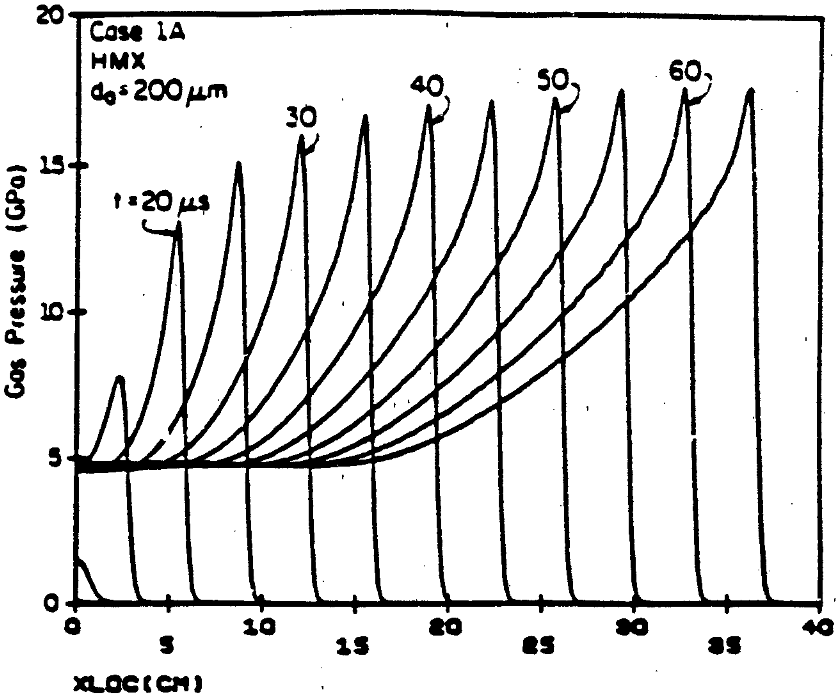

Fig. 5.1a Pressure-distance profiles for Case 1A. P_{CJ}=16.9 GPa, T_{CJ}=4289 K, r_{CJ}=1.76 g/cc.

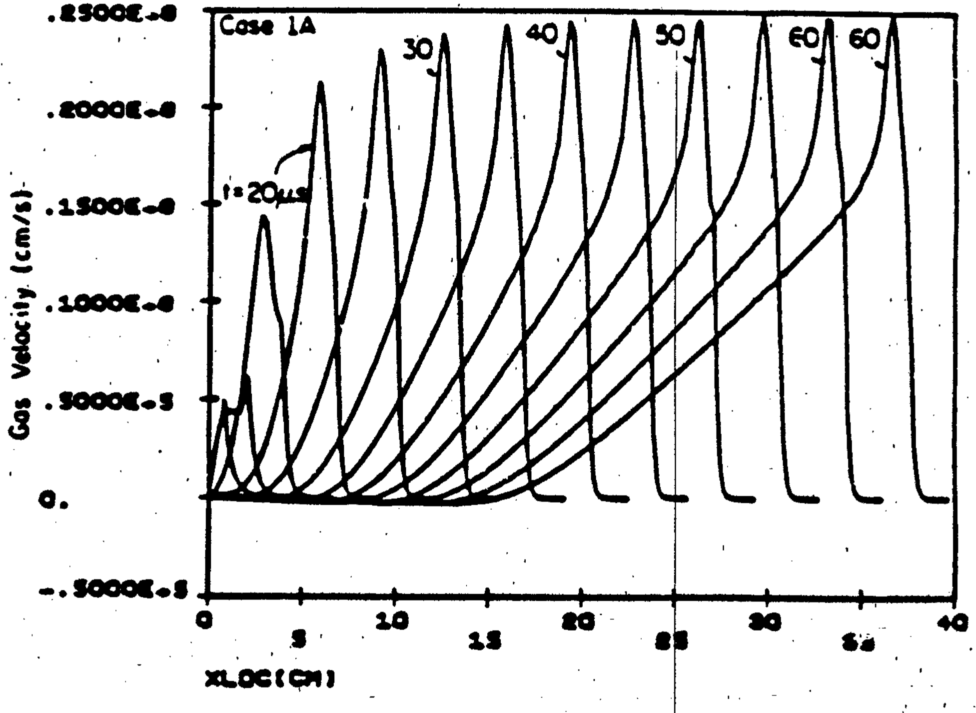

Fig. 5.1b Gas velocity-distance profiles for Case 1A. u_{CJ}=1.88 mm/μs, D=7.01 mm/μs.

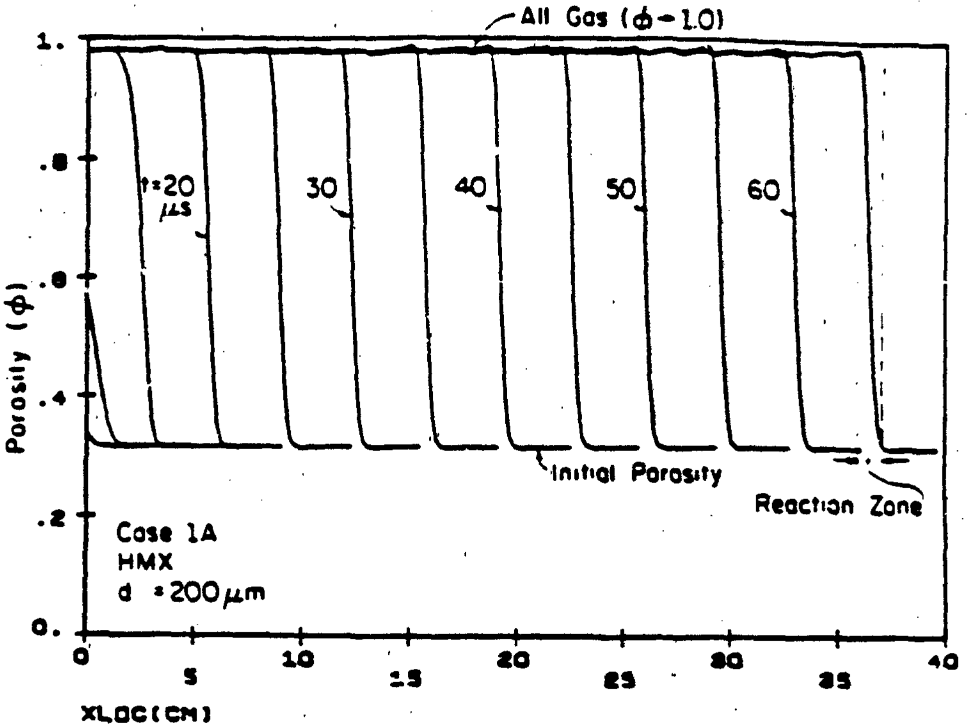

Fig. 5.1c Porosity-distance profiles for Case 1A.

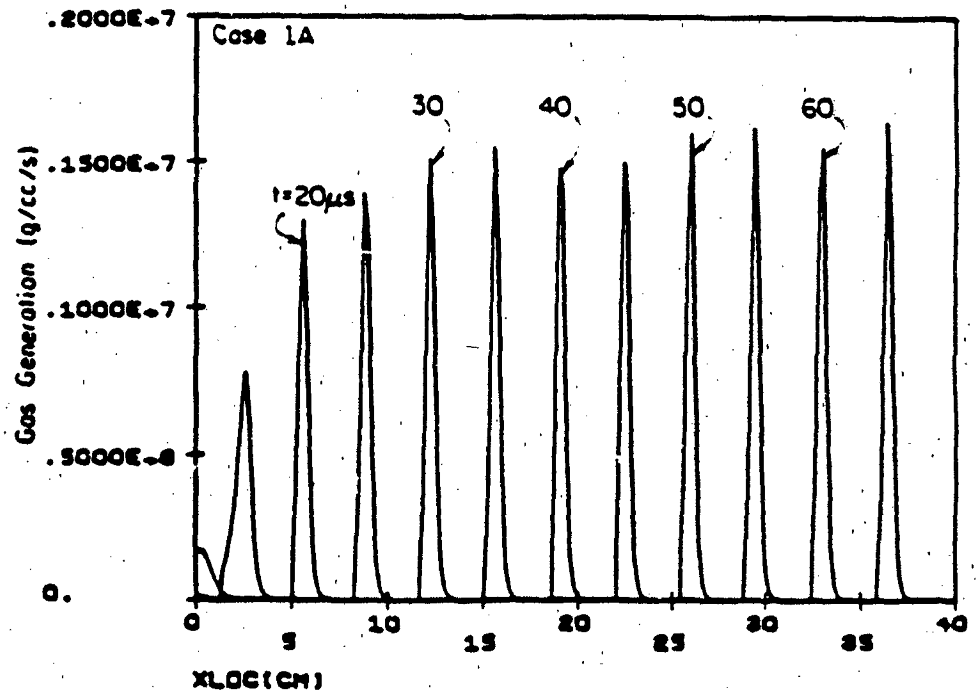

Fig. 5.1d Gas generation rate (G) - distance profiles for Case 1A.

where γ is the polytropic exponent, $u(x)$ is the fluid velocity at some location x in the expansion wave, and c_{CJ} is the sound velocity at the CJ point. Also, two known boundary conditions are that the fluid velocity must equal zero at both the fixed walls ($x=0$, $x=L$). Thus, the steady state wall pressure, $P(x=0)$, predicted by the computer code should satisfy Eq. (1.14) with $u(x=0)=0$. Case 1A predicts values of $u_{CJ}=1.88$ mm/μs, $c_{CJ}=5.12$ mm/μs and $\gamma=2.73$. For these input parameters Eq. (1.14) yields a steady state wall pressure, $P(x=0) = 5.0$ GPa . This is consistent with the code predictions (see Fig. 5.1a), wnere $P(x=0, t > t_{CJ})$ $=4.9$ GPa.

Shown in Fig. 5.1b are the gas velocity profiles (u,x) for Case 1A at 5 μs time increments. It is interesting to note that u approaches zero at approximately the midpoint between the CJ point and the wall. Detonation theory [25] predicts $u = 0$ at exactly half-way for a polytropic gas and approximately half-way for other gases.

Using the $t=60$ μs profile as an example, several key features of the detonation wave can be illustrated. First, upstream of the detonation front, $x > 35$ cm, the material is undisturbed and $u = 0$. Figures 5.1a, 5.1c, and 5.1d also indicate that for $x > 35$cm the pressure and porosity are unchanged from their initial conditions and the product gas generation rate is zero. Again referring to thu $t=60$ μs profile in Fig. 5.1b, one can see that the gas velocity rises rapidly across the shock front ($x=34$ cm) and then decreases to $u = 0$ at around $x=13$ cm. This feature is consistent with the statement presented above regarding the shape of the expansion wave. (Note, the t=60 μs profile was selected for illustration purposes only.) Because of the steady state nature of the detonation solution, all of the post-detonation profiles will show similar characteristics.

The remaining figures for Case 1A (Figs. 5.1c, 5.1d) illustrate the gas porosity (ϕ ,x) and gas generation rate (G,x) profiles at time increments of 5 μs. The very narrow detonation reaction zone is apparent in both figures. In Fig. 5.1c it is depicted by the short distance over which the porosity increases from ambient, ϕ_{go}=0.32, to an all-gas regime, ϕ_g= 1.0 .

Finally, the ignition front x,t locus for Case 1A was compared with experimental data by Price and Bernecker [75]. The comparison is shown in Fig. 5.1e. The square data points indicate the experimental (x,t) data [75] and the solid line comes from the numerical simulation. The agreement is favorable with both sets of data indicating a steady state detonation velocity of approximately 7 mm/μs.

As stated earlier, the input data for Cases 1B, 1C, and 1D are similar to Case 1A with the exception of the initial porosity. The gas pressure, gas velocity, porosity and gas generation rate profiles for these three cases can be found in Figs. 5.2 - 5.4 . Also, Table 5.3 provides a summary of the CJ parameters for all the cases. The first line in each data set lists the values calculated using the DDT computer code and the second line

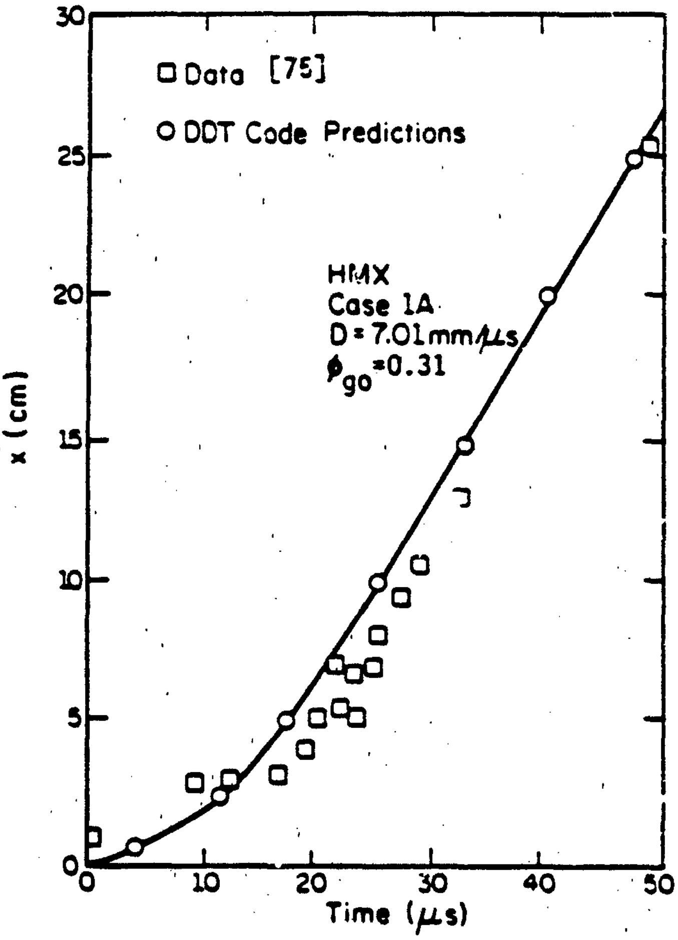

Fig. 5.1e : comparison between experimental [75] x,t ignition front data and DDT code predictions.

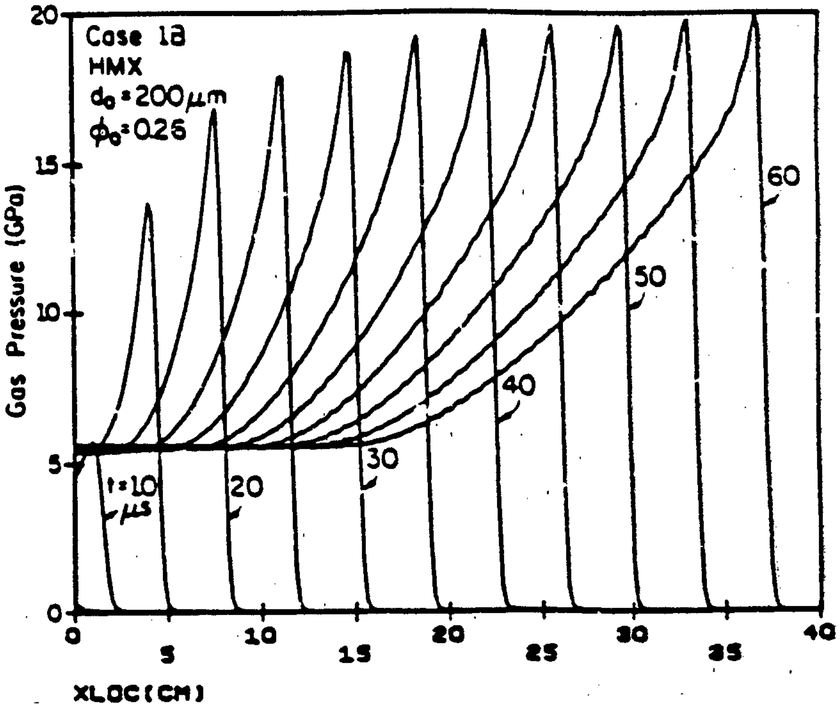

Fig. 5.2a Pressure-distance profiles for Case 1B P_{CJ}=19.64 GPa, T_{CJ}=4293 K, r_{CJ}=1.87 g/cc.

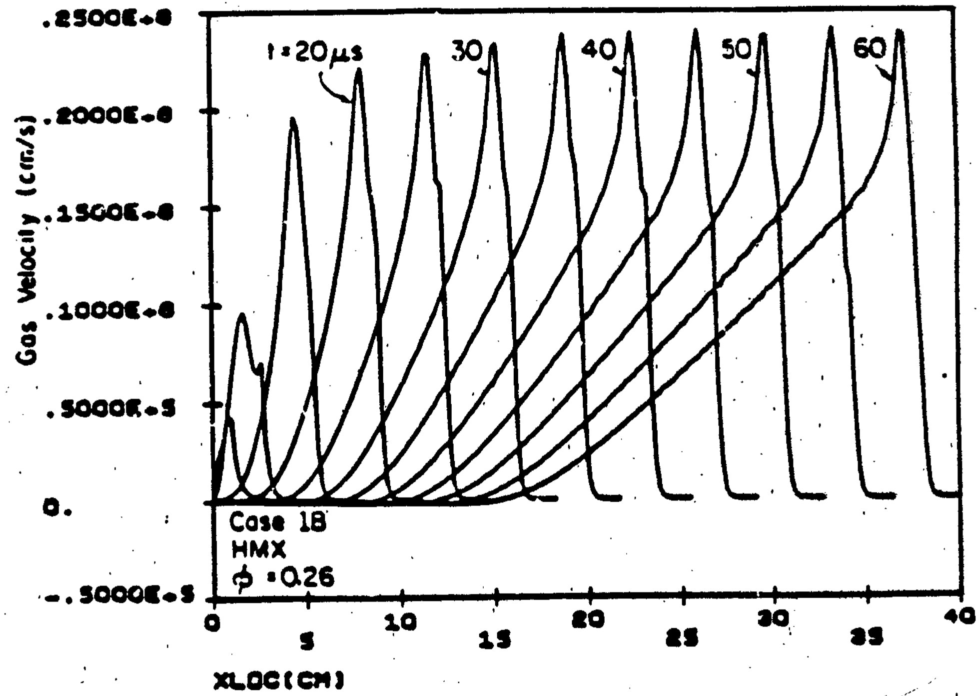

Fig. 5.2b Gas velocity-distance profiles for Case 1B, u_{CJ}=1.93 mm/µs, D=7.40 mm/µs.

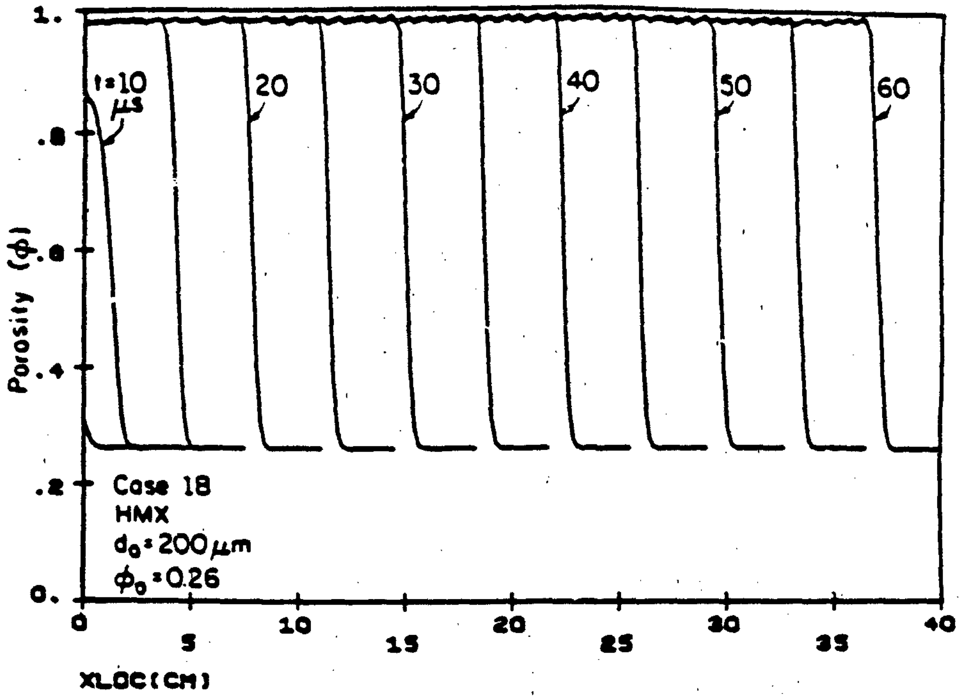

Fig. 5.2c Porosity-distance profiles for Case 1B. ϕ_{go}=0.263.

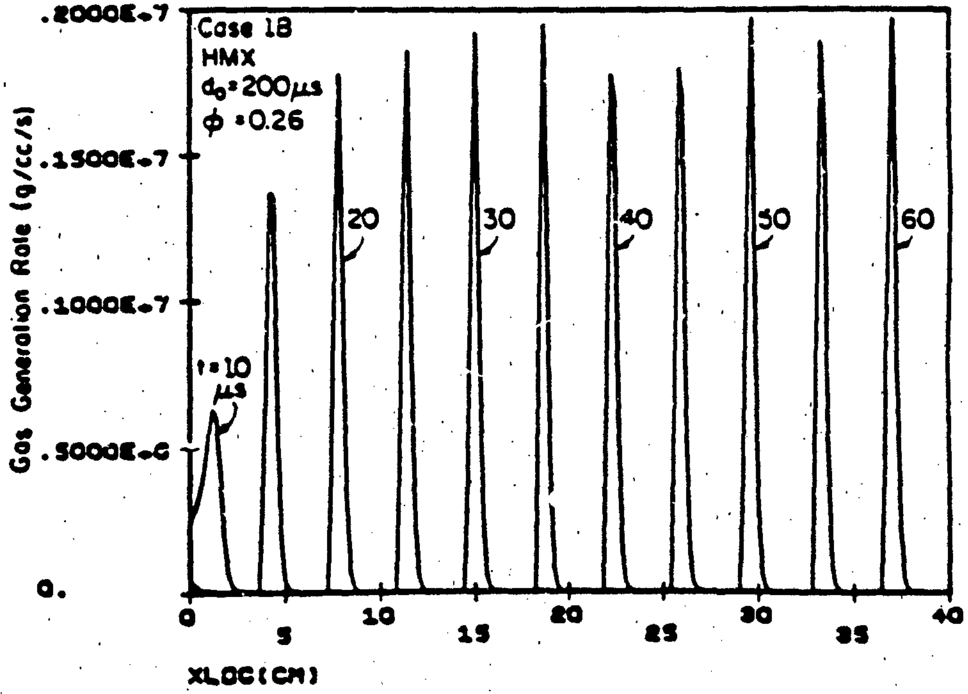

Fig. 5.2d Gas generation rate-distance profiles for Case 1B.

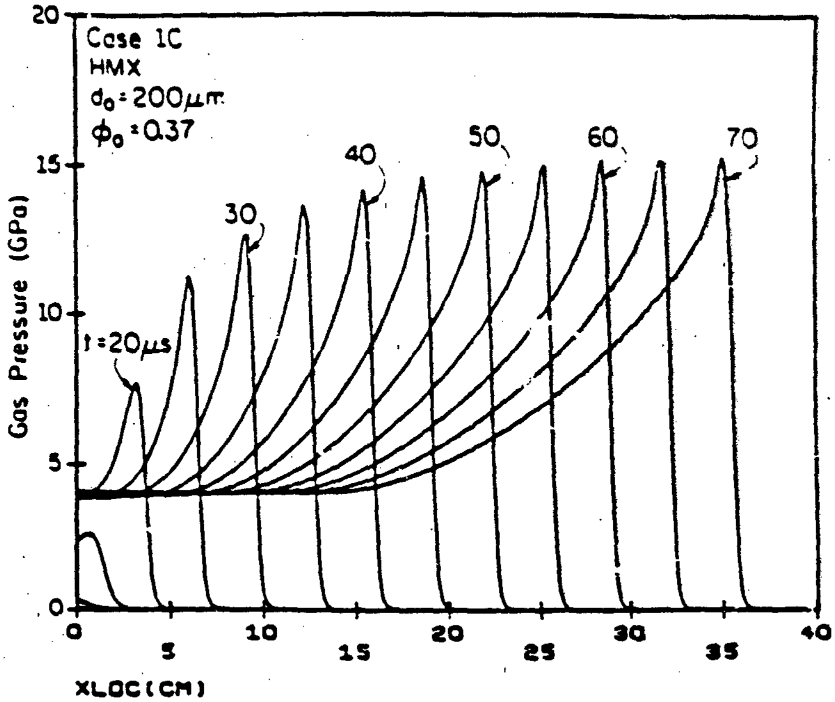

Fig. 5.3a Pressure-distance profiles for Case 1C. P_{CJ}=14.38 GPa, T_{CJ}=4201 K, r_{CJ}=1.64 g/cc.

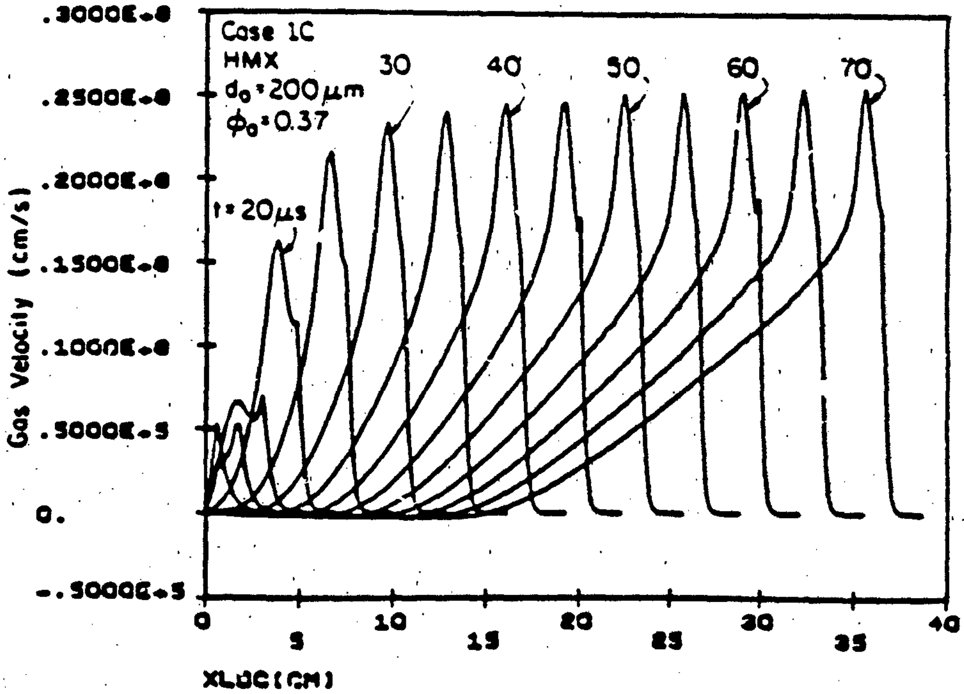

Fig. 5.3b Gas velocity-distance profiles for Case 1C. u_{CJ}=1.82 mm/μs, D=6.65 mm/μs.

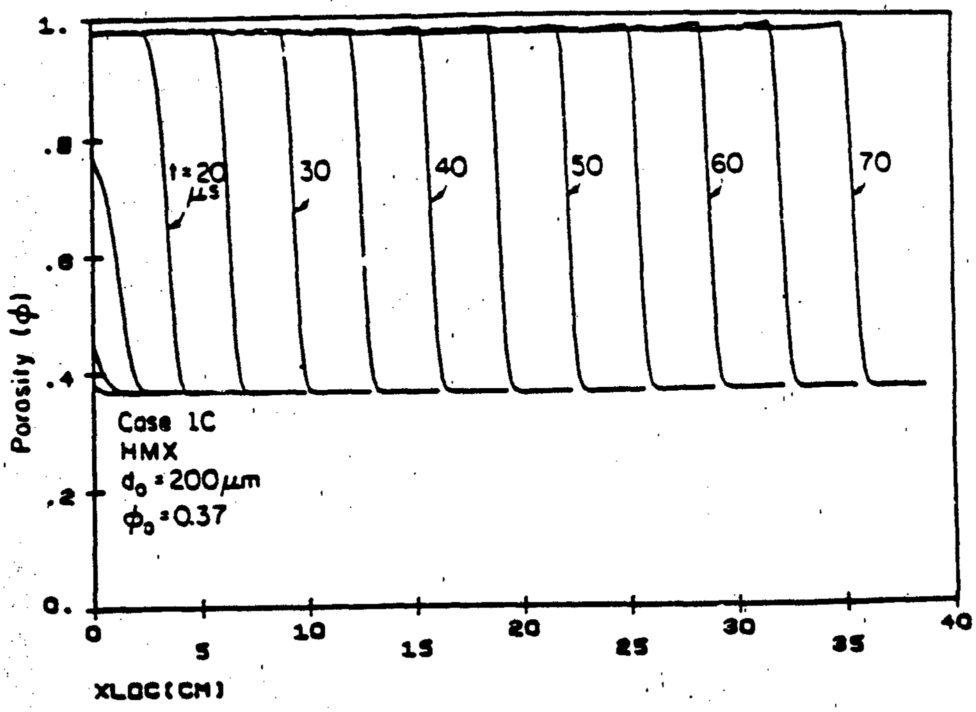

Fig. 5.3c Porosity-distance profiles for Case 1C. ϕ_{go}=0.368.

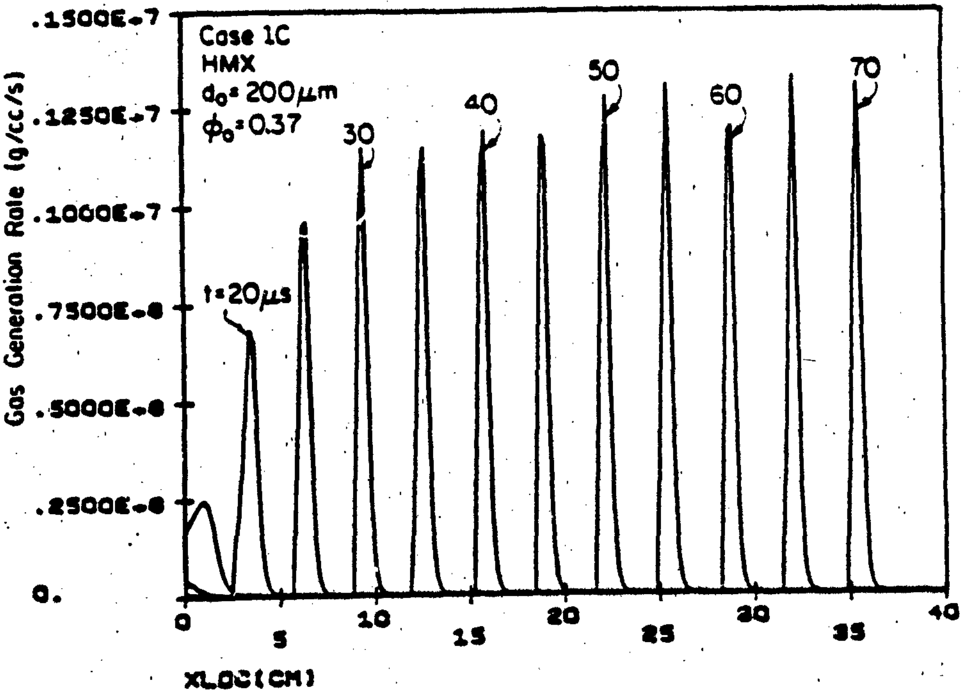

Fig. 5.3d Gas generation rate-distance profiles for Case 1C.

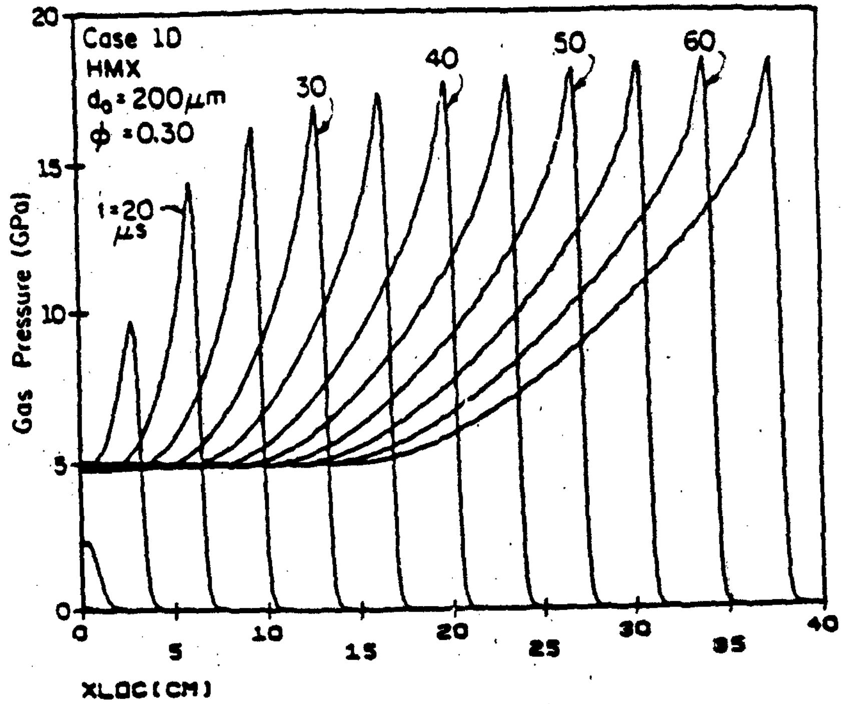

Fig. 5.4a Pressure-distance profiles for Case 1D. P_{CJ}=18.11 GPa, T_{CJ}=4406 K, r_{CJ}=1.80 g/cc.

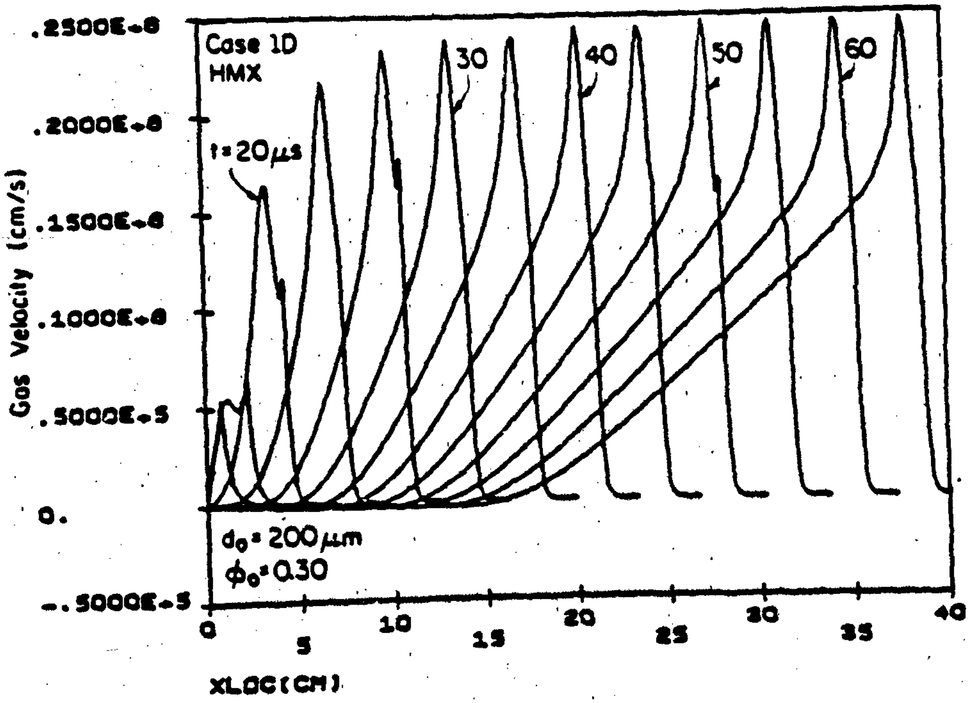

Fig. 5.4b Gas velocity-distance profiles for Case 1D. u_{CJ}=1.95 mm/μs, D=7.14 mm/μs.

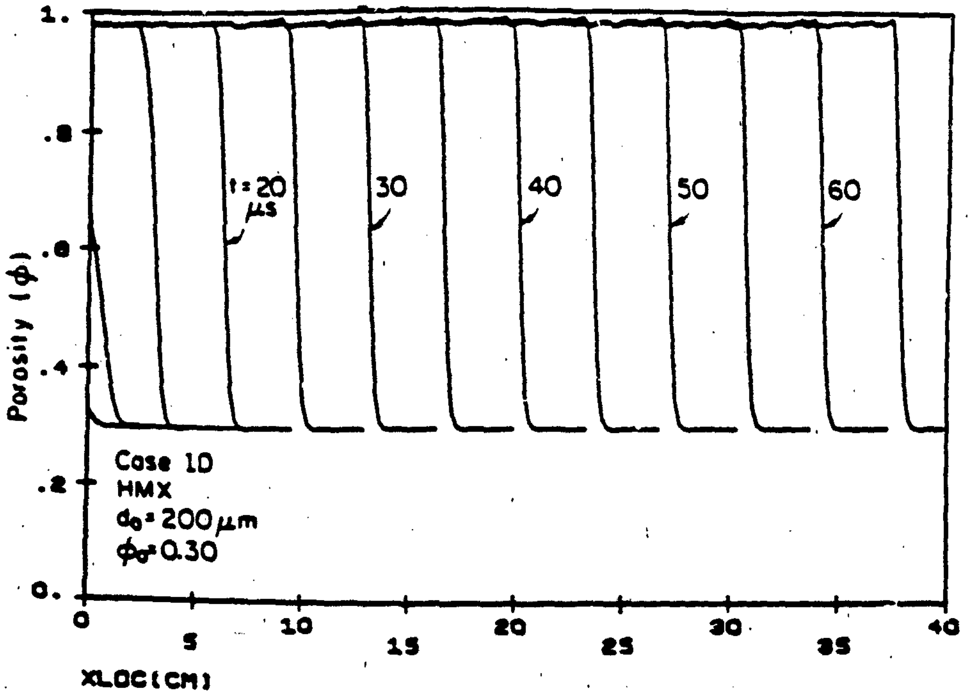

Fig. 5.4c Porosity-distance profiles for Case 1D. ϕ_{go}=0.30.

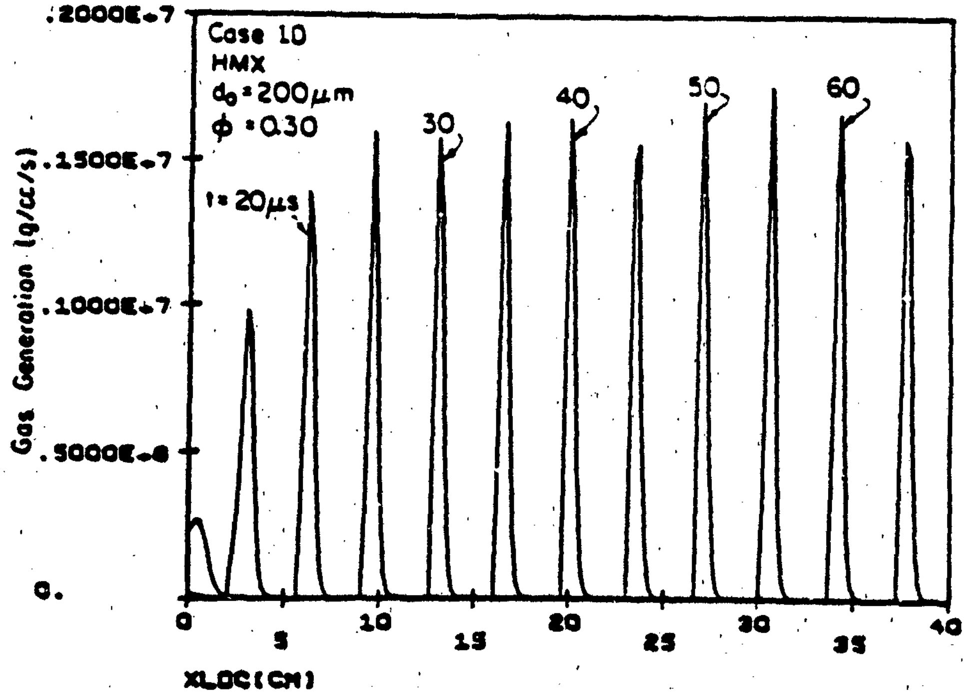

Fig. 5.4d Gas generation rate-distance profiles for Case 1D.

TABLE 5.3: CJ Parameters (P,T,v,D from DDT code)

	r_2(g/cc)	ϕ_o	P_{CJ}(GPa)	T_{CJ}(°K)	u_{CJ}(mm/us)	c_{CJ}(mm/μs)	D(mm/μs)	r_{CJ}(g/cc)
DDT Code	1.20	0.368	14.38	4201	1.82	4.83	6.65	1.64
TIGER	"	"	14.92	4337	1.84	4.92	6.76	1.65
DDT Code	1.30	0.316	16.90	4289	1.88	5.12	7.01	1.76
TIGER	"	"	17.26	4304	1.89	5.16	7.05	1.78
DDT Code	1.33	0.300	18.11	4406	1.95	5.26	7.14	1.80
TIGER	"	"	18.00	4300	1.91	5.22	7.13	1.81
DDT Code	1.40	0.263	19.64	4393	1.93	5.45	7.40	1.87
TIGER	"	"	19.60	4280	1.92	5.42	7.33	1.89

contains the TIGER predictions.

Figure 5.5 is a plot of detonation pressure versus initial loading-density squared (r_2) for HMX. The data comes from three sources, TIGER, the DDT computer calculations and data from Ref. 76 . In the range of densities 1.0g/cc < r_2 < 1.38 g/cc, the approximation [76]

$$P_{CJ}(GPa) = 10.3\ r_2^2 \qquad (5.1)$$

can be used to calculate the CJ pressure for these explosives.

As shown in Ref. 76, most condensed explosives consisting of the elements Carbon, Hydrogen, Nitrogen and Oxygen (CHNO-type) have a linear relationship between CJ density and initial loading density, $r_2 = (1-\phi_{go})r_{po}$. In fact, the P,v behavior is independent of the CHNO formulation. This is illustrated in Fig. 5.6 . The open-circle data points represent TIGER predictions for HMX ($C_4H_8N_8O_8$) and the triangular data points are for several different CHNO explosives. They include; TNT $C_7H_5N_3O_6$, RDX $C_3H_6N_6O_6$, PETN $C_5H_8N_4O_{12}$, Tetryl $C_7H_5N_5O_8$, and Picric acid $C_6H_3N_3O_7$. The DDT code predictions are shown as the solid-box data points. A least squares fit to the data from Ref. 76 yields

$$r_{CJ} = 0.136 + 1.238\ r_2 \qquad (5.2a)$$

and a least squares fit to the TIGER data yields

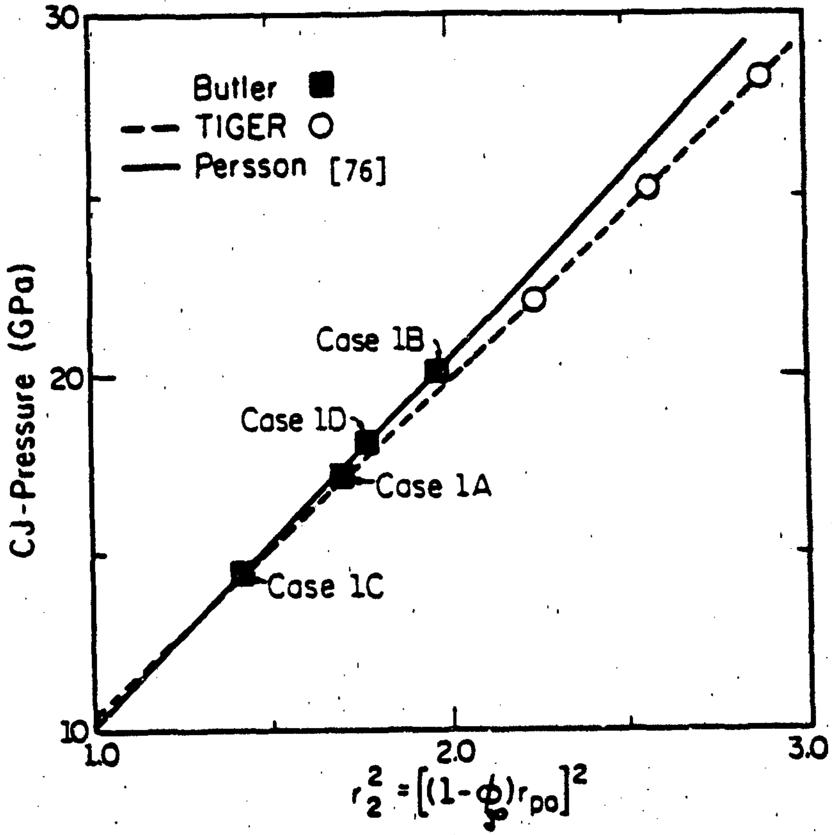

Fig. 5.5 CJ Pressure-(loading density)^2 data from three sources. For 1.0 g/cc<r_2<1.38 g/cc, P_{CJ}=10.3 r_2 (GPa).

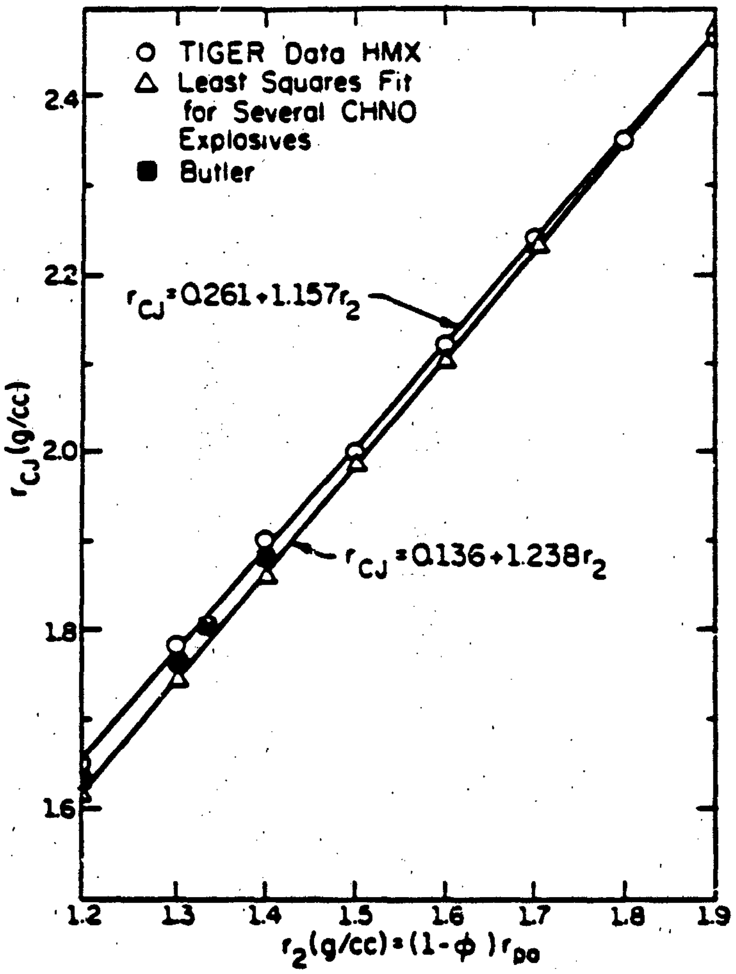

Fig. 5.6 Illustration of linear relationship between CJ density (r_{CJ}) and initial loading density (r_2) for most CHNO-type explosives.

$$r_{CJ} = 0.261 + 1.157\, r_2 \qquad (5.2b)$$

Shown in Fig. 5.7 is a plot of the detonation run-up distance as a function of the initial porosity, ϕ_{go}. The input data for each case is the same as in Table 5.2 . The one experimental data point shown is from Ref. 75. For the porosity range $0.26 < \phi_{go} < 0.37$, Fig. 5.7 shows the detonation run-up distance increases as the initial porosity increases. This is in fact the same trend shown by Korotkov et. al [36] for granulated PETN (d_o =40 μm and d_o = 1000 μm). However, their data showed the run-up length to be a minimum at ϕ_{go}=0.20 (for d_o =1000 μm) and then to increase for $\phi_{go} < 0.20$.

The four cases discussed above, Cases 1A, 1B, 1C, and 1D are all examples of a DDT-Case 1 hazard. Each simulates a packed bed of HMX undergoing a transition from an accelerating convective burn to a steady state detonation. Values predicted for CJ pressures, CJ temperature, and CJ density match TIGER calculations. In addition, the detonation run-up length ℓ_{CJ} and steady state detonation velocity D obtained from the DDT code are in close agreement with experimental data.

From the data presented above, it appears that this type of DDT is primarily a result of the rapid pressure rise early in the event. Because of the complex coupling between all of the flow variables, it would be misleading to state that one parameter alone is responsible for the DDT. The 'pressure-rise rate' is a

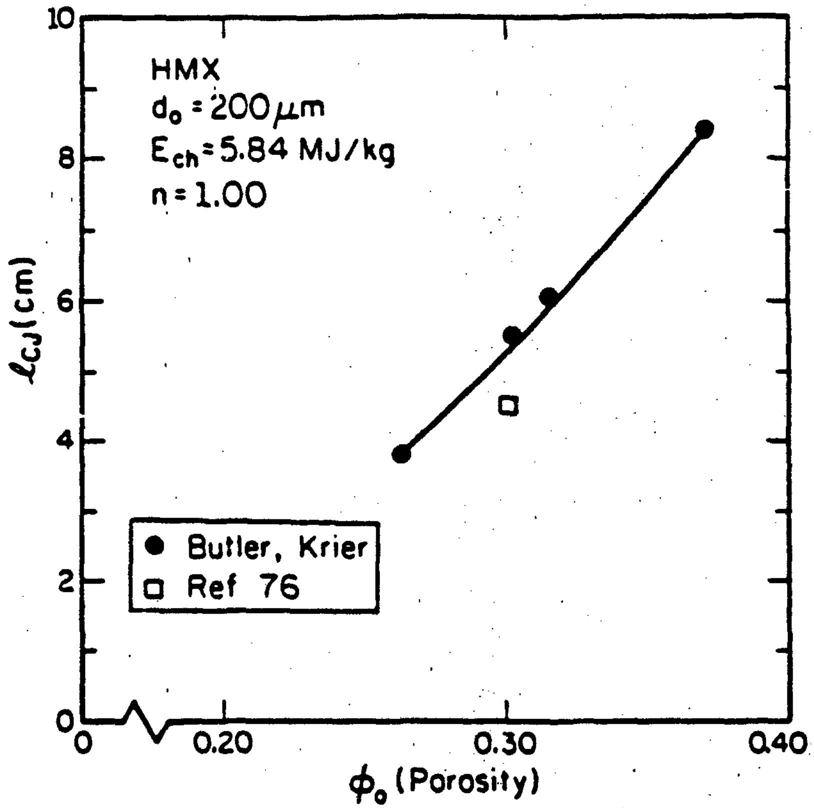

Fig. 5.7 Detonation run-up distance (ℓ_{CJ}) versus initial porosity (ϕ_o) for Cases 1A-1D and data from Ref. 76.

function of several variables. In all cases studied thus far, the initial grain size was very small (d_o=200 μm) and the reaction rate (reflected in the burning rate index n) was very high (n=1.0). These two factors, combined with product gas confinement, high initial solids loading ϕ_{go} and high chemical energy E_{ch} ,result in a rapid pressure rise.

It should be noted that in some instances of convective burning in a confined bed of granulated propellant, DDT will not occur. For instance, experiments [36] show that when a granular bed has a high initial gas porosity (i.e., ϕ_{go}=0.55), DDT does not occur.

The question now arises as to whether a propellant bed with the same initial conditions as Case 1A - 1D will make a transition to a detonation if the reaction rate is reduced. Although it is true that the steady state detonation solution is unaffected by the kinetics, the transient events prior to detonation are greatly affected. The DDT code yields the same CJ properties and detonation velocity over the range $0.85 < n < 1.02$. However, the detonation run-up distance λ_{CJ} was found to be dependent on the reaction rate n. Figure 5.8 is a plot of λ_{CJ} versus burning rate index, n. With the exception of n, the input data is unchanged from Case 1A. Interestingly, when the index was lowered to n=0.80, a major new factor is predicted.

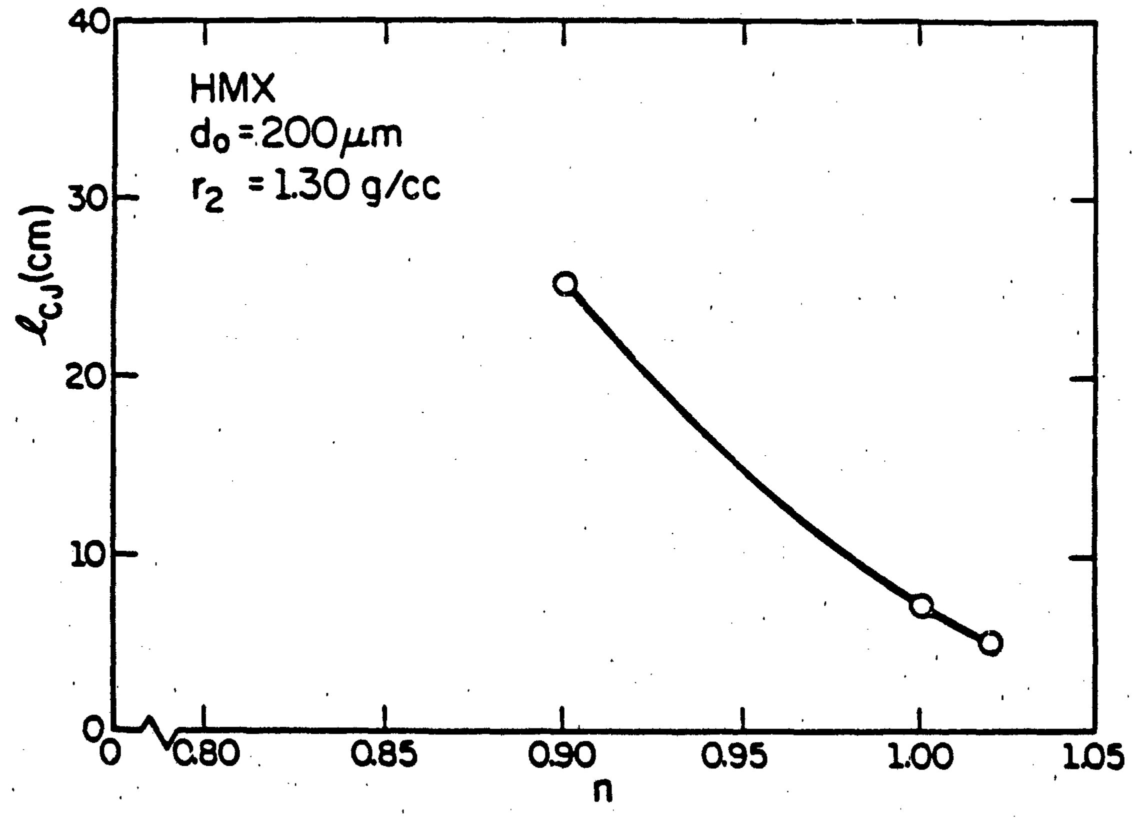

Fig. 5.8 Detonation run-up distance (ℓ_{CJ}) as a function of burning rate index (n) (see Eq. 1.1a). E_{ch}=5.84 MJ/kg, ϕ_{go}=0.316.

5.2.1 Plug Formation

Figures 5.9a - 5.9c show the pressure profiles (P,x) for a case identified as Case 1E. The initial conditions are the same as Case 1A with the exception that the burning rate index is now n=0.80. Figure 5.9a shows pressure profiles for 75 μs < t < 103 μs. At t=103 μs the ignition front has reached x= 10 cm and is traveling at a velocity , u = 0.5 mm/μs. Note, due to the slow burning propellant grains, the pressure buildup is very slow relative to Cases 1A - 1D. The maximum pressure at t =103 μs is 3 GPa. Figure 5.10a shows the porosity profiles for the same times. Behind the ignition front, ϕ_g slowly increases with time. Ahead of the ignition front, ϕ_g is decreasing, indicating that the voids are closing.

An interesting event happens at t= 104 μs. The bed has totally collapsed ahead of the ignition front. The term "plug" is sometimes used in the DDT literature [4]. Once the plug forms, the hot product gases can no longer permeate the material ahead of the ignition front. From t=104 μs on, the propellant behind the ignition front continues to react, increasing the local gas pressure. As the gas pressure at x=10 cm increases with time, the propellant to the right of the plug will be stressed. Figure 5.9b shows the pressure-distance profiles at t = 104 μs, 105 μs, 106 μs and 107 μs. The increasing gas pressure to the left of the plug has stressed the right hand side, increasing the thickness of the solid plug. In addition, a shock wave has formed at the front of the plug as a result of coalescing stress waves. Figure 5.10b

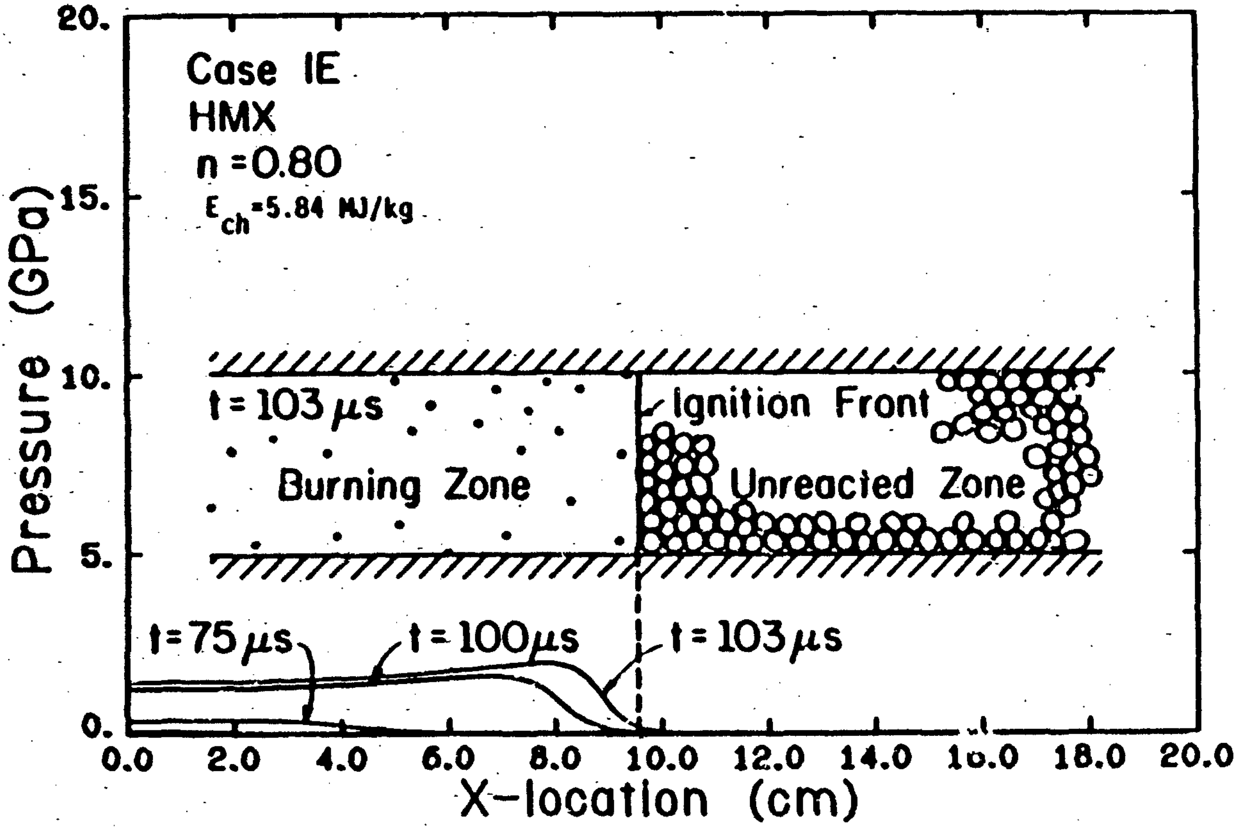

Fig. 5.9a Pressure-distance profiles for Case 1E illustrating slow (compared to Cases 1A-1D) pressure-rise rate in reaction zone.

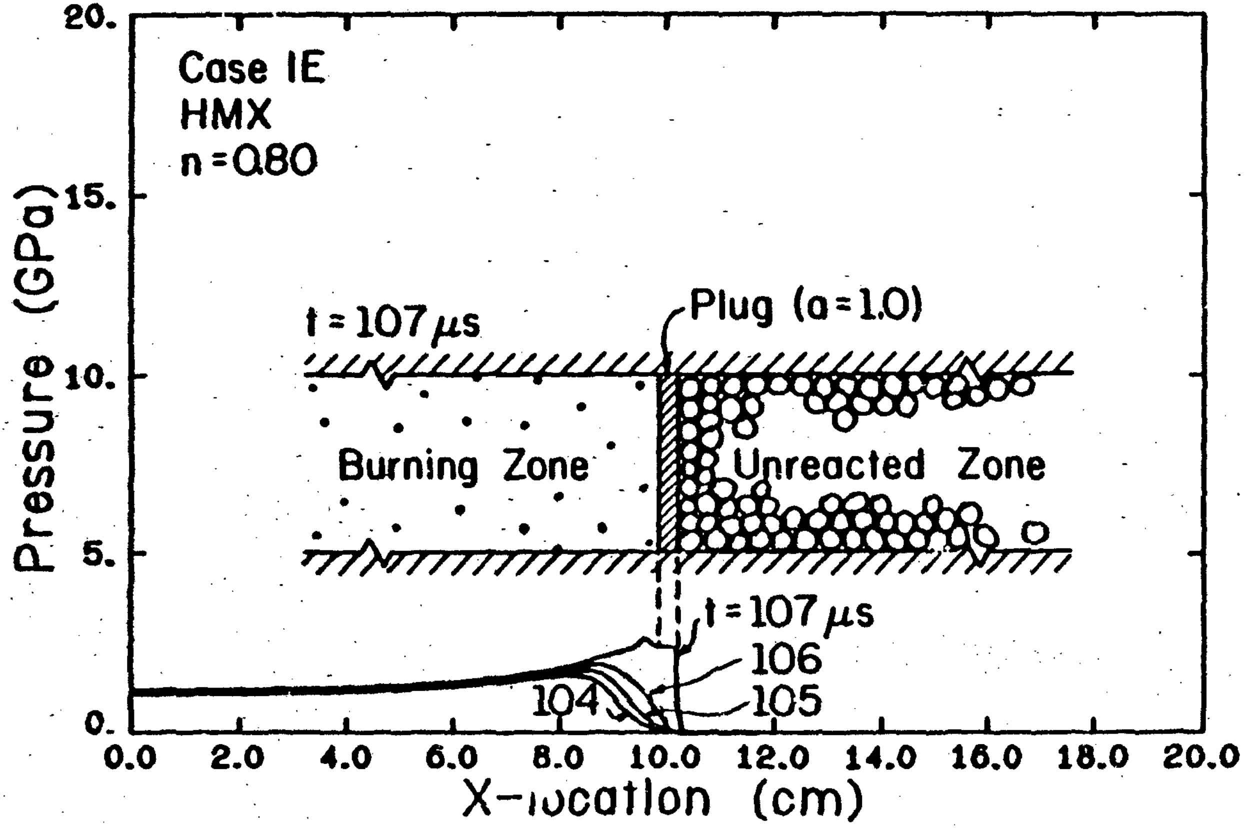

Fig. 5.9b Pressure-distance profiles for Case 1E showing plug formation at $x=10.0$ cm. Shock wave propagating through the plug is shown in the $t=107$ us profile.

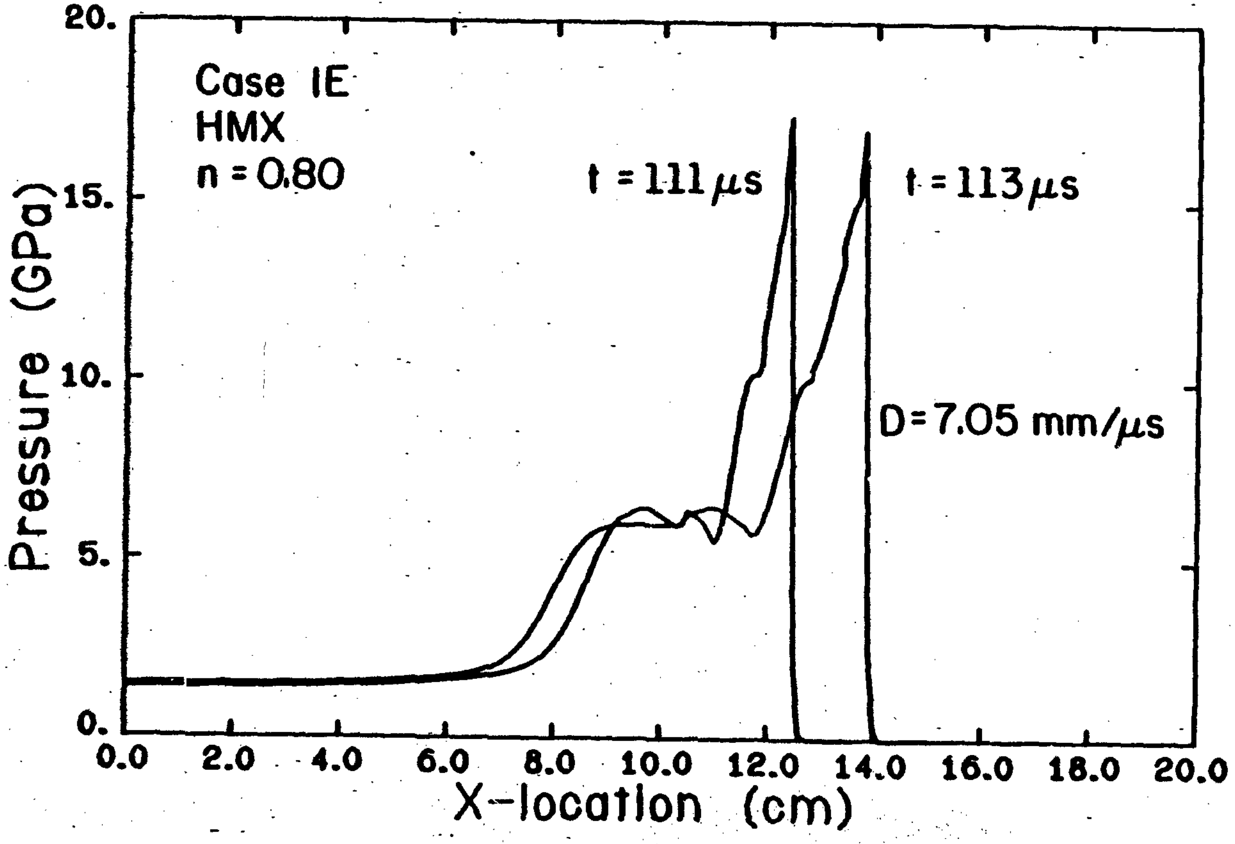

Fig. 5.9c Pressure-distance profiles for Case IE showing the detonation wave propagating through the granular material at D=7.05 mm/μs.

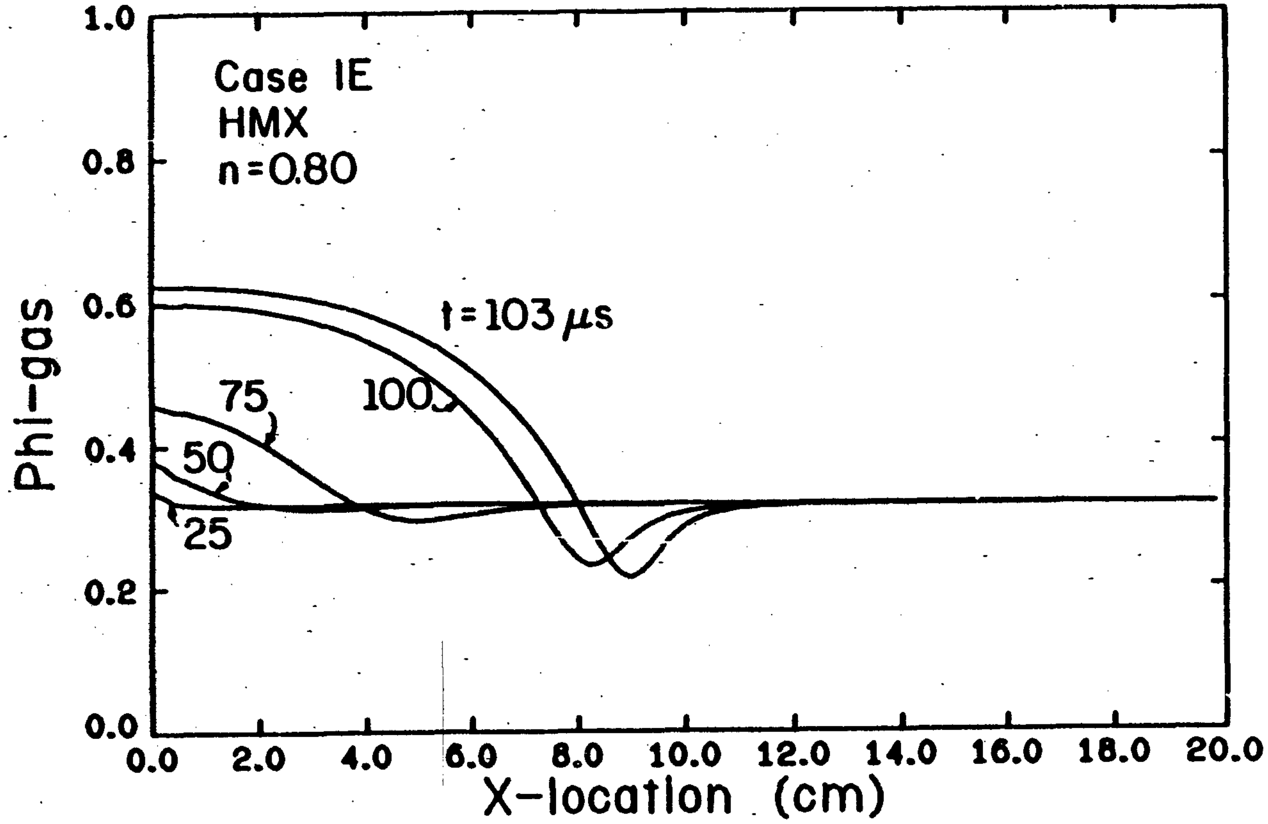

Fig. 5.10a Porosity (ϕ_g) versus distance profiles for Case 1E prior to plug formation.

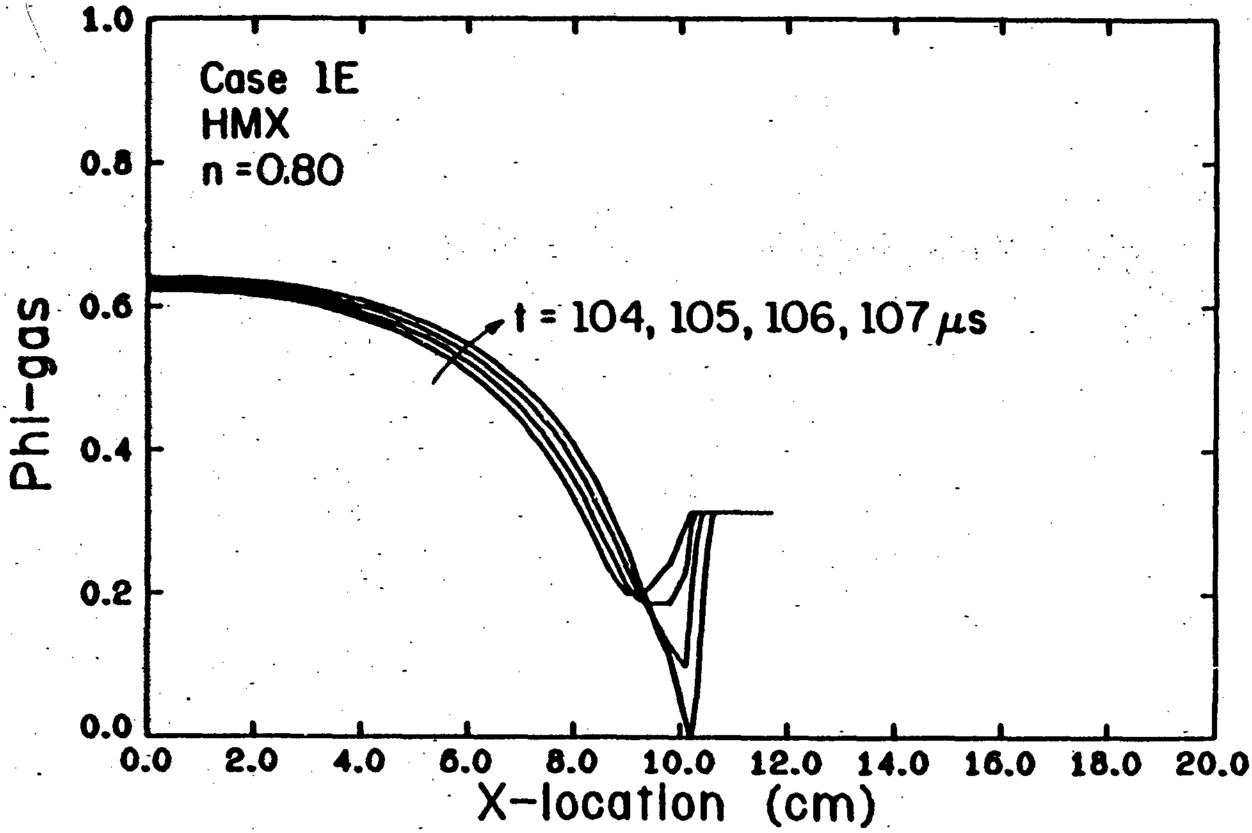

Fig. 5.10b Porosity (ϕ_g)-distance profiles for Case 1E showing plug formation.

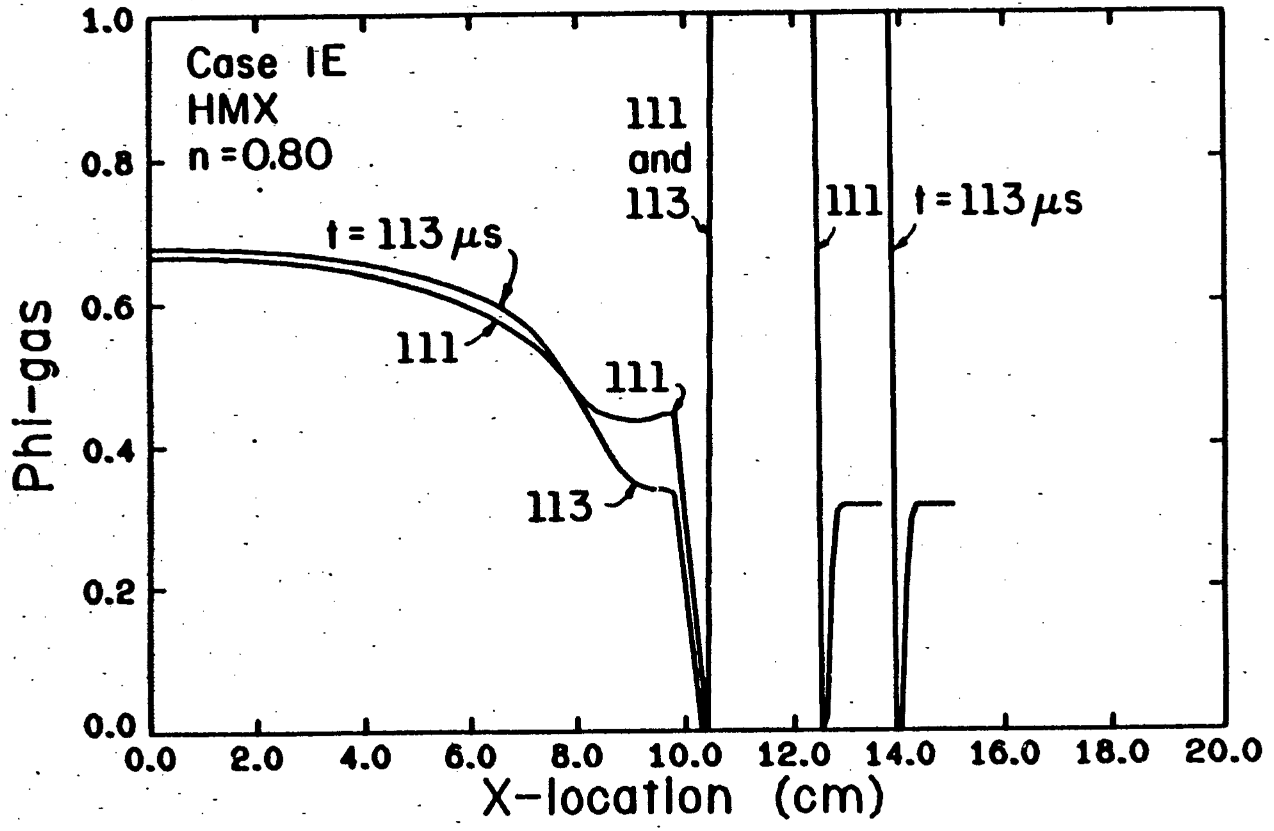

Fig. 5.10c Porosity-distance profiles for Case 1E after DDT. A value of ϕ_g=1.0 indicates complete burn out and ϕ_g=0.0 indicates plug formation.

shows the porosity-distance profiles for the same four times.

The final two figures, Figs. 5.9c and 5.10c show the pressure-distance and porosity-distance profiles at t = 111 μs and t = 113 μs. The shock wave developed in the plugged propellant has shock initiated the material at the location x = 12 cm. The result is a steady-state detonation wave traveling at CJ velocity through the unreacted material. Figure 5.11 is a plot of the ignition front x,t locus for Case 1E. The ignition front accelerated to u = 0.5 mm/μs while burning in the convective mode prior to plug formation. After shock initiation of the plugged material, the wave travels at a constant value of D =7.0 mm/μs.

5.2.2 DDT-Case 1 Summary

The DDT-Case 1 scenario involves an accelerating convective ignition front propagating through a bed of fragmented high-energy propellant. Under certain circumstances (i.e., small particles, high confinement, rapid solid to gas decomposition, long bed length, high initial solids loading), a shock can develop before the ignition front reaches the end of the granular bed. If so, the deflagration wave can make a transition to a steady state detonation wave. This was illustrated in Cases 1A - 1D. In each of the four cases the DDT event started with a quiescent bed of granular propellant, ignited at one end by a thermal source. The final solution in each of the four cases was a steady state detonation wave which satisfied the Rankine - Hugoniot jump conditions.

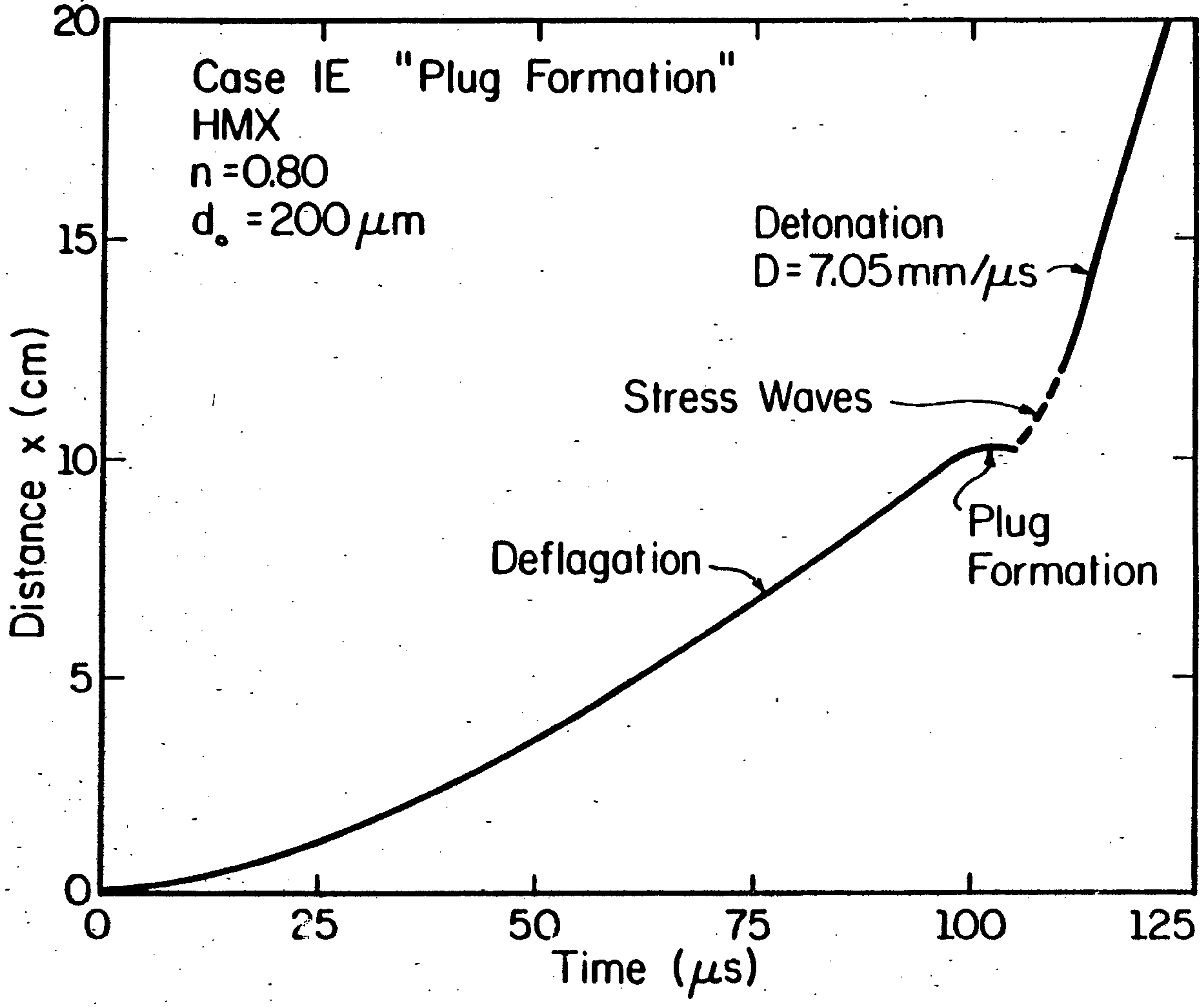

Fig. 5.11 Ignition front (distance,time) locus for Case 1E. A 'plug' has formed at x=10 cm and the detonation initiates at x=12 cm.

As expected from chemical equilibrium calculations, the CJ properties and detonation velocity predicted by the DDT code are dependent on the initial solids loading. This was illustrated in Fig. 5.1e and 5.1f . One should note that this is only true _if_ the granular bed makes the transition to detonation. Simply specifying an initial solids loading does not assure a transition to detonation. Put more strongly, the buildup to DDT cannot be equated to a single propellant property or initial condition alone. This is apparent when one studies the complex system of coupled differential equations governing the flow behavior.

A second branch of the DDT-Case 1 hazard was illustrated in Case 1E. The initial conditions were the same as Cases 1A - 1D with the exception of the burning rate index which was lowered to n = 0.80. At first, it would appear that a lower decomposition rate would eliminate the rapid pressure rise behind the reaction front and thus eliminate the DDT hazard. However, as was shown in Case 1E, a DDT is still possible. In Case 1E the granular bed formed a "plug" ahead of the ignition front. This was due to the compaction caused by the stress wave transmitted ahead of the slow burning reaction front. Several microseconds after plug formation, stress waves generated by the reacting granular material behind the plug, shock initiated the porous material ahead of the plug. This type of DDT has been identified in the recent experiments conducted by Campbell [4].

Although the granular bed DDT scenario (Case-1) is the most widely studied in the laboratory [4-8,32], it may not be the only DDT hazard possible in a rocket motor environment.

5.3 DDT-Case 2

Figure 1.5 is an illustration of the DDT-Case 2 experimental configuration. The region labeled "Zone 2" is a segment of cast explosive or cast high-energy propellant and "Zone 1" is a granular bed of the same material. It is assumed that the length L of the granular bed is less than it's critical detonation run-up length, ℓ_{CJ}. This indicates that the granular bed <u>cannot</u> undergo a direct transition from deflagration to detonation. However, through momentum transfer across the Zone 1/Zone 2 interface, the rapid pressure rise in Zone 1 can result in shock initiation of the cast material in Zone 2.

Figure 5.12 shows the proposed sequence of events leading to a DDT-Case 2 event. Superimposed on each section of the figure is a solid line representing the local gas porosity ($\phi_g = 1/(1-a)$) as a function of x, the distance from the left wall. A value of $\phi_g = 1.0$ ($a=\infty$) represents a zone of all gas while $\phi_g=0$ ($a=1.0$) indicates a homogeneous solid.

Part A is a sketch of a granular bed adjacent to a porous, cast explosive. The black dots in Fig. 5.12 represent voids in the cast material. Throughout the entire process (A-F) the solid grains to the left of the ignition front are reacting, resulting in an increasing gas pressure. Consequently, the porous material

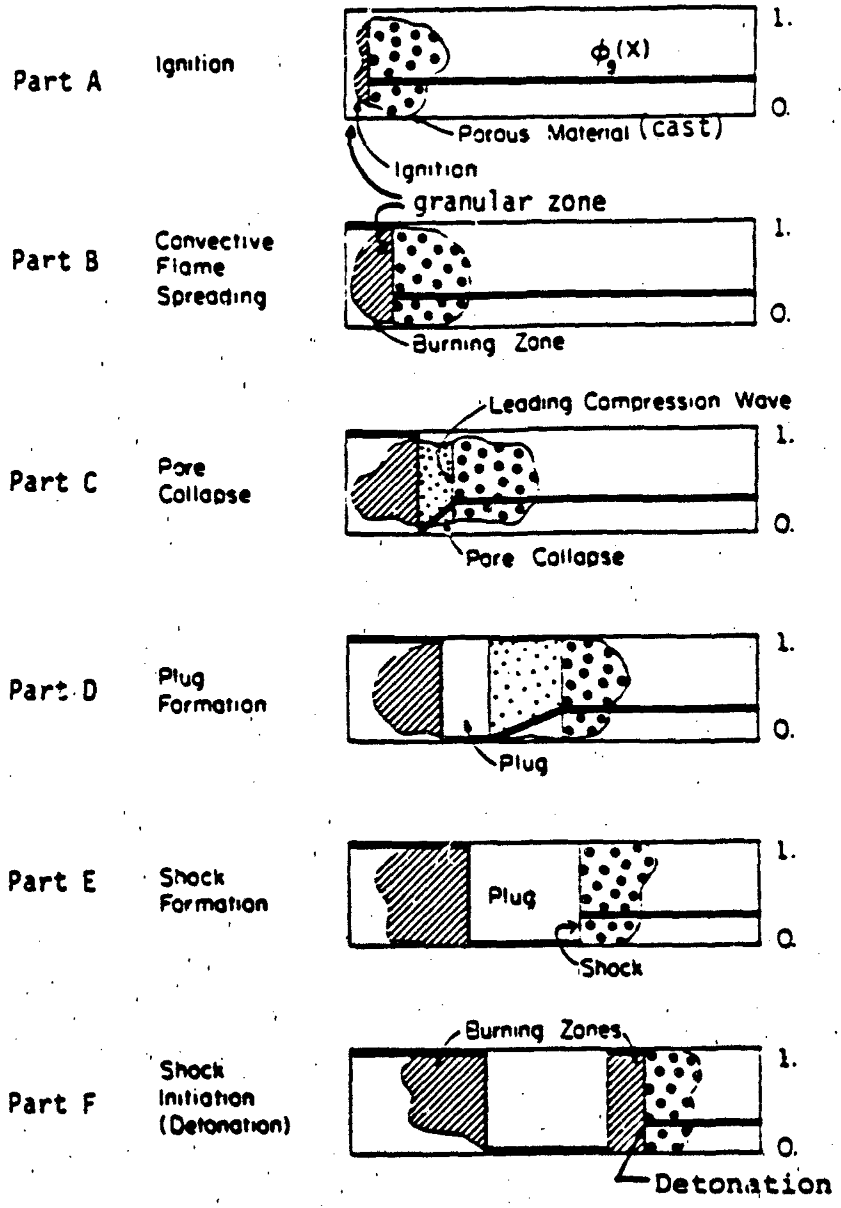

Fig. 5.12 Proposed sequence of events leading to a DDT-Case 2.

to the right of the ignition front is stress loaded at the material interface. Illustrated in Part C is the collapse of the pores ($\phi_g = 0$), a result of the local stress exceeding the yield strength of the material (see Sec. 3.6). As shown in Part C, the pore collapse begins at the porous explosive/ burning bed interface. Parts D and E show the thickness of the pore-collapse zone to increase with time as the lead compression wave travels further into the cast material. Finally, the finite compression waves coalesce into a shock front which shock initiates the cast explosive at a location downstream of the interface. Starting at this location a detonation propagates through the porous material while a retonation wave propagates back through the compressed material (Part F).

If one is to analyze the transient events occurring in the cast material shown in Fig. 1.5 (Zone 1), one initial and two boundary conditions must be specified. For this analysis the initial conditions are the same as those listed in Table 5.2. To specify the boundary condition at $x=0$ one must determine the rate at which the reacting granular bed (Fig. 1.5, Zone 2) stresses the cast material (Fig. 1.5, Zone 1). This was determined by running the DDT code discussed in the previous section with bed lengths less than the critical detonation run-up length. For example, Case 1A ($\ell_{CJ} = 6$ cm) was run witn L=4 cm. Plotted in Fig. 5.13 are the P(t, x=L) functions obtained for several different cases. As shown in the figure, the pressurization rate in the granular bed, dP/dt, is strongly dependent on the initial particle size. Using the information provided in Fig. 5.13 as a P(x=0,t)- time boundary

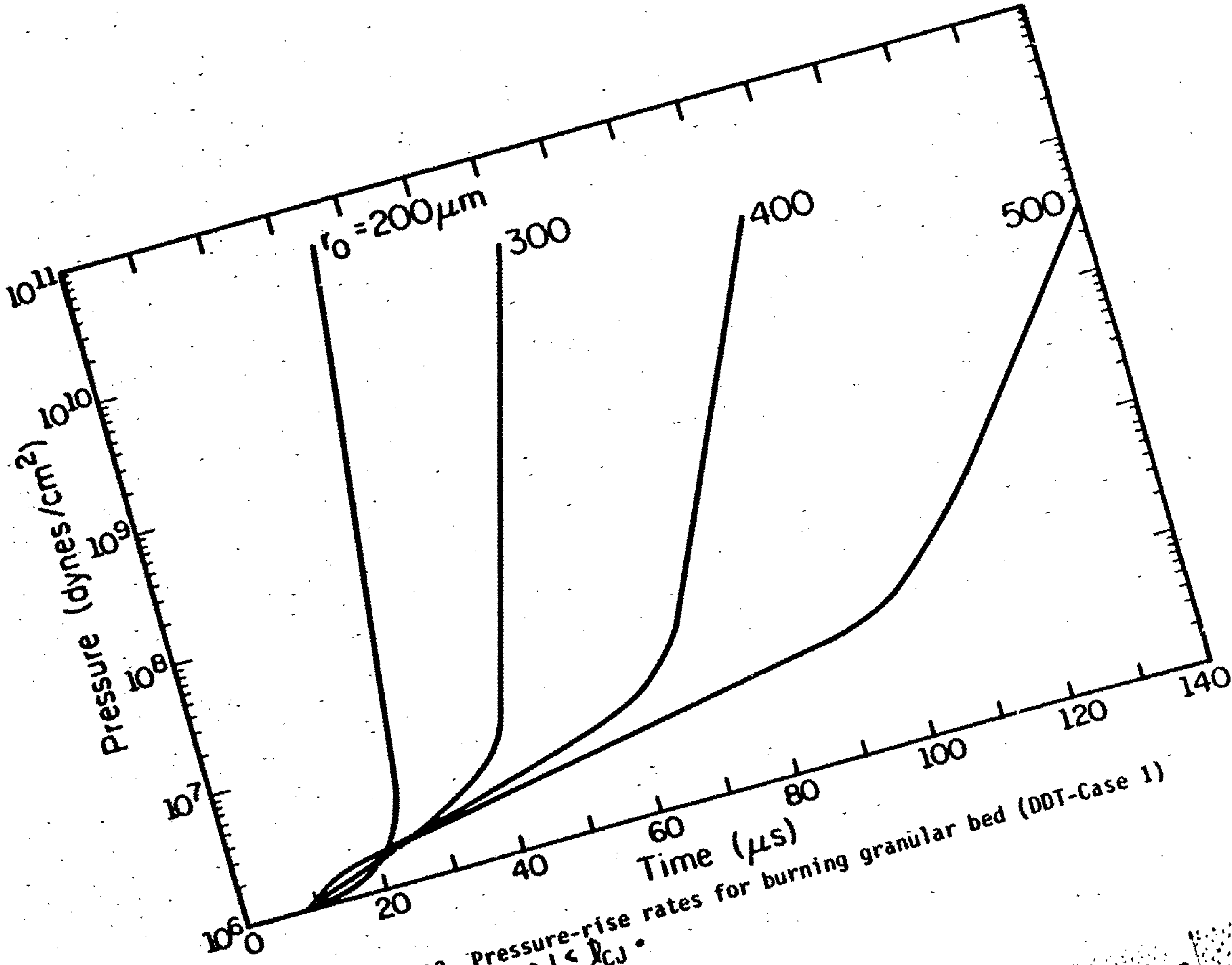

Fig. 5.13 Pressure-rise rates for burning granular bed (DDT-Case 1) where $L < \ell_{CJ}$.

condition, one can now evaluate the stress wave propagation through the cast material.

For comparison purposes, two DDT-Case 2 simulations were run where a linear stress-time function

$$P(x=0,t) = (0.20\ \mathrm{GPa}/\mu s)\ t \qquad (5.3)$$

was used as the $\bar{X}=0$(Fig1.5) boundary condition. The first case (r_2 =1.90 g/cc, a_o =1.00) will be referred to as Case 2a and the second case (r_2=1.30 g/cc, a_o=1.46) as Case 2b.

The Pop-plot data shown in Fig 2.4 provides useful information for this comparison. A shock strength of 3 GPa in porous HMX (r_2 =1.24 g/cc, a=1.53) corresponds to a detonation run-up distance of ℓ_{CJ} = 5 mm . In fact, the porous HMX will detonate when shocked to a strength as low as P = 0.6 GPa. On the other hand, the near-crystalline HMX (r_2=1.89 g/cc, a=1.01) shown in Fig. 2.4 requires a shock strength of at least P = 4 GPa to detonate.

Figure 5.14 is a plot of the stress profiles (P,x) predicted for Case 2a. The stress waves coalesce into a 3 GPa shock at a distance of approximately x = 16 cm. Once the shock forms it propagates through the bed at a constant velocity of U = 3.88 mm/μs. There are no signs of chemical reaction throughout the entire process (0< t<80 μs). The temperature behind the shock front is calculated from the solid-phase caloric equation of state

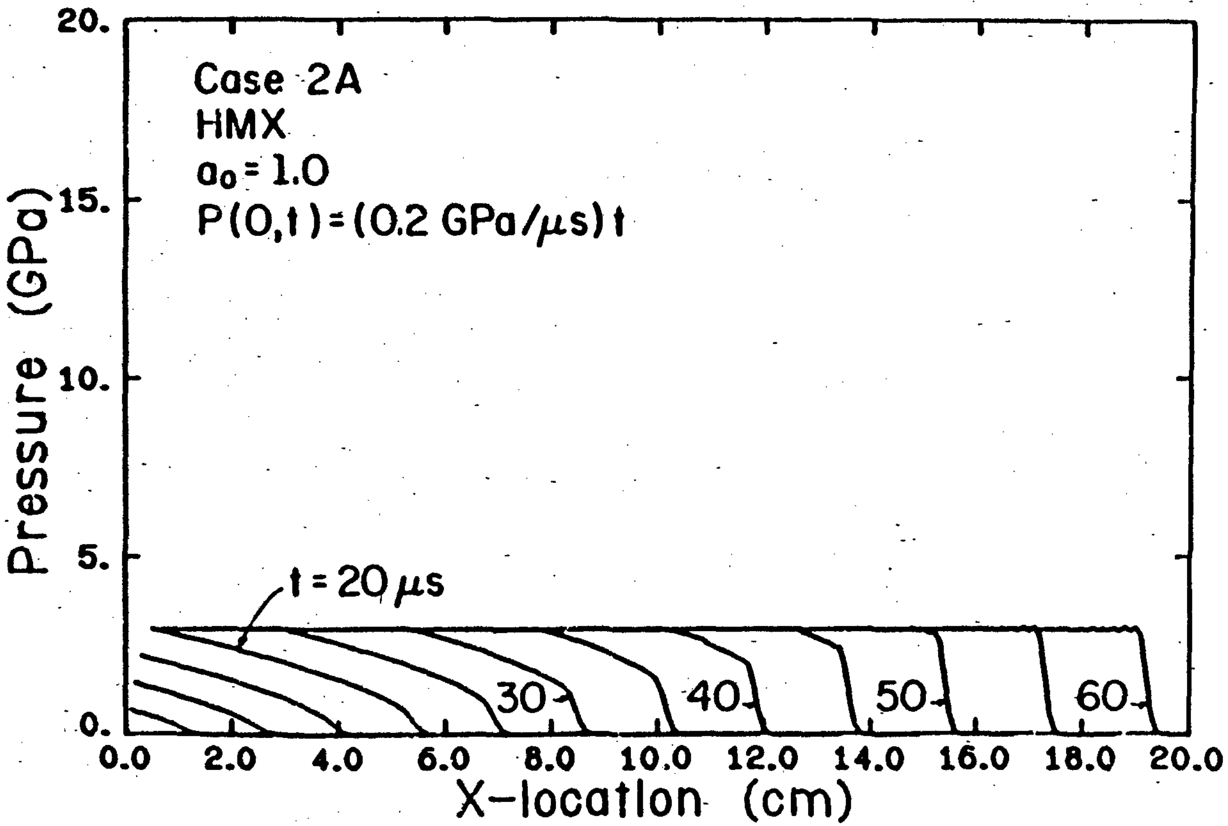

Fig. 5.14 Stress-distance profiles for Case 2A. A shock forms at x=16cm.

(Eq. 3.38) to be T = 345 K, a value too low to initiate reaction in the homogeneous solid.

Porous, exothermic materials are much more sensitive to shock initiation than those containing voids. Pop-plot data (Fig. 2.4) clearly indicates that porous materials will detonate at much lower shock strengths than the equivalent homogeneous sample. It's theorized [51] that the density discontinuities within the porous material are responsible for multi-dimensional shock interactions resulting in localized zones of increased thermal energy. It has been estimated that a shock strength of 3 GPa in HNS will generate a hot spot temperature of well over 1000 K [29]. The DDT computer code incorporates the hot spot theory of Hayes [29] (see Appendix C) when modeling porous reactive materials.

Shown in Fig. 5.15 are the pressure profiles (P,x) for Case 2b. Profiles for t= 5 μs and t= 10 μs are shown in Fig. 5.15a. During the time increment $0 < t < 10$ μs the voids in the porous material begin to collapse. At t=10 μs a shock wave begins to form at around x=1.5 cm. Prior to t=10 μs there is no sign of chemical decomposition of the solid phase. Shown in Fig. 5.15b are the pressure- distance profiles at t=11 μs. The solid has begun to react and the pressure shows a peak of P = 4.5 GPa. The bulk temperature at this time is only T=350 K.

Note, a 50 K increase in the solid phase temperature should not be enough to initiate reaction. However, the hot spot temperature, calculated for the 3 GPa shock front, is T_H =2066 K.

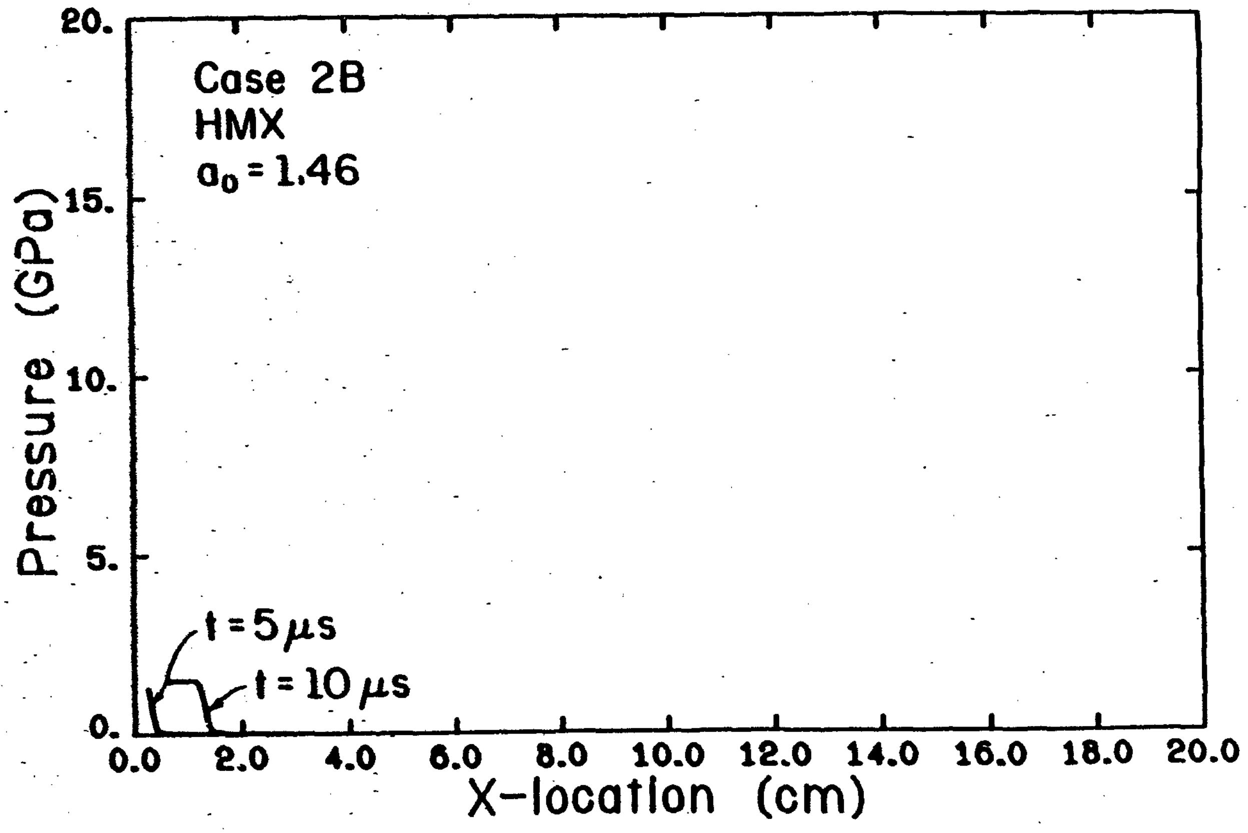

Fig. 5.15a Stress-distance profiles for Case 2B. A shock forms in the porous HMX at t=10 us.

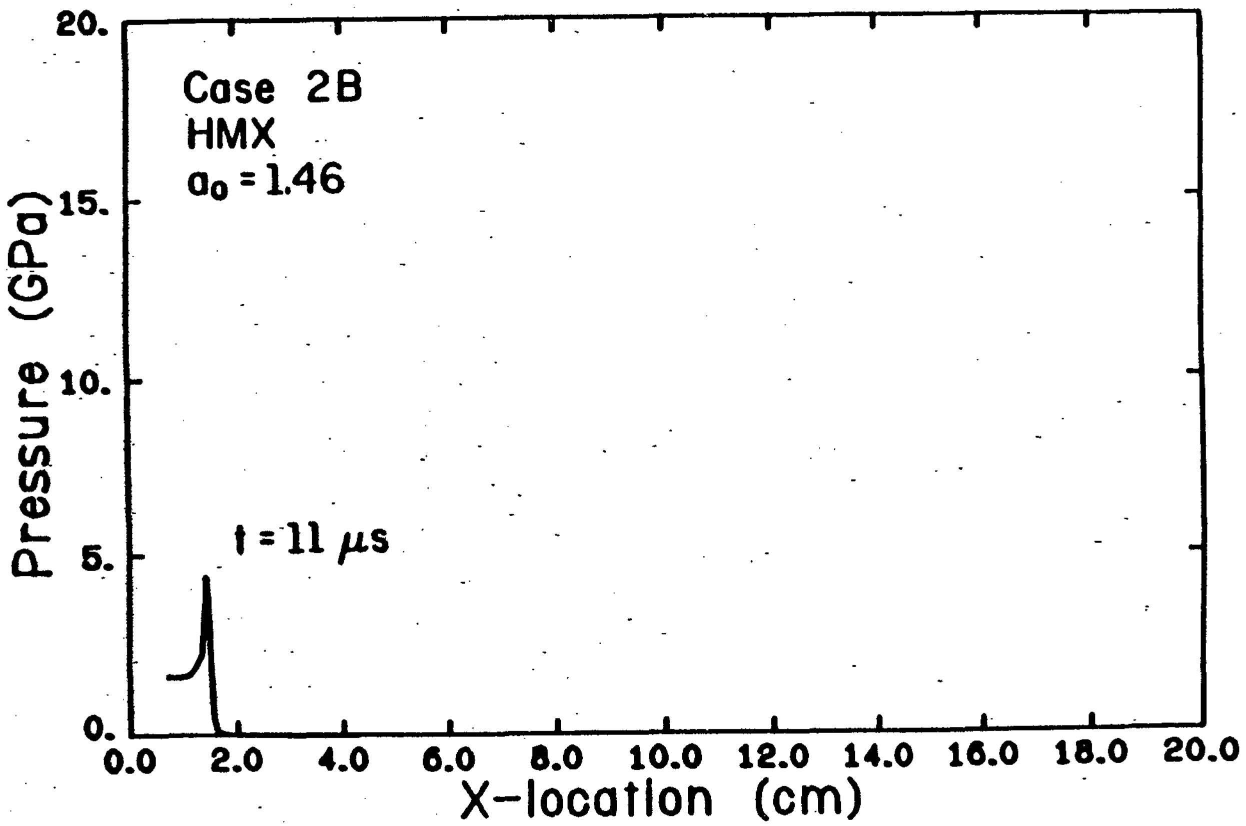

Fig. 5.15b Pressure-distance profile for Case 2B at t=11 us. The shock formed at t=10 us has shock initiated the HMX.

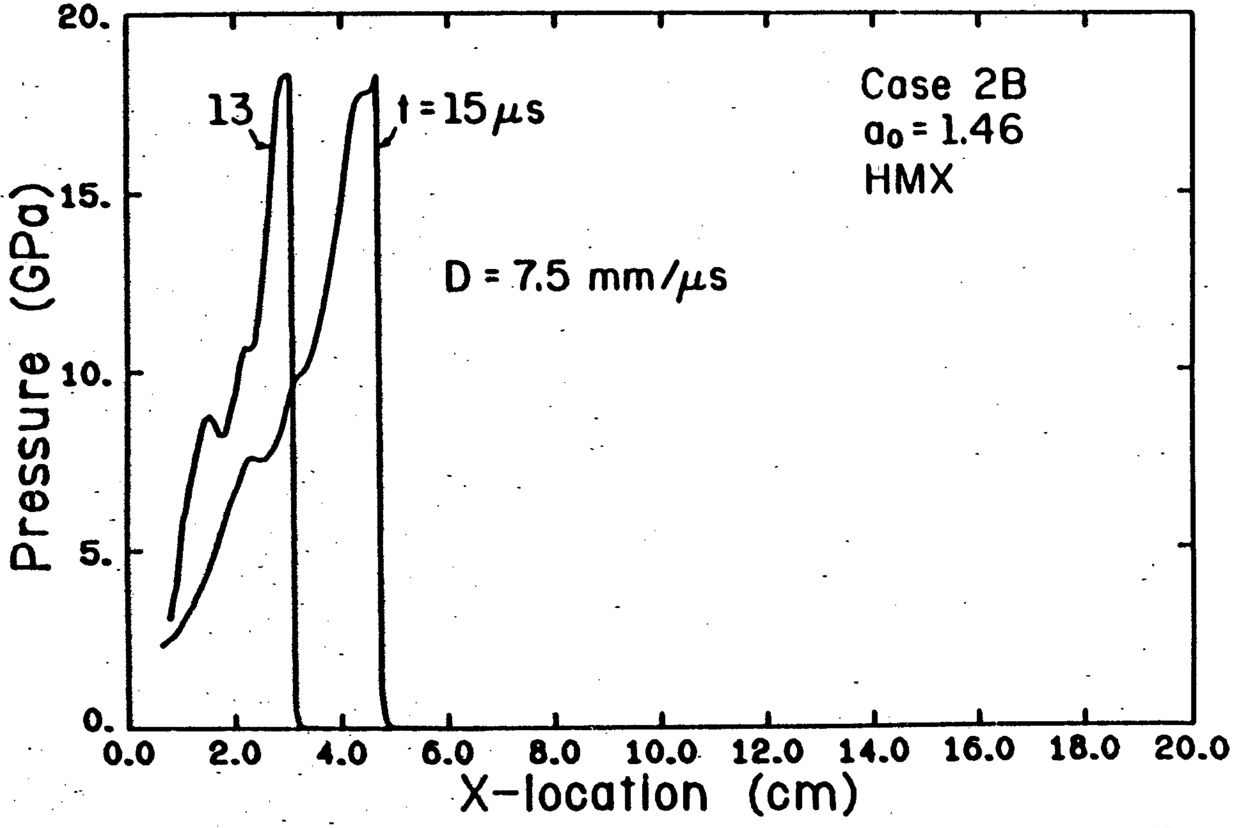

Fig. 5.15c Pressure-distance profiles for Case 2B at t=13 us and t=15 us.

The solid decomposition begins in the hot spot vicinity and spreads to the surrounding material. This all occurs in less than one-half microsecond. The sequence of stress profiles shown in Fig. 5.15c illustrate the fully developed, steady state detonation wave propagating through the reactive material at a velocity of D=7.50 mm/μs. The CJ state is measured to be P=17.9 GPa, T_{CJ}=4200 K and v_{CJ}=0.619 cc/g. Figure 5.16 shows the x,t locus of the stress wave front and the detonation front for Case 2B.

5.3.1 DDT-Case 2 Summary

In some instances, the length of a granular bed (i.e., Fig. 1.1) may be less than the critical detonation run-up length of the bed configuration. If this is the situation, one might assume that the motor would over-pressurize, but not detonate. However, when one considers the surrounding porous cast propellant, the hazard still exists.

A DDT-Case 2 event can occur when the stress waves generated in a burning granular bed shock initiates adjacent cast material. Computer predictions show this to be a very likely event if the adjacent cast material contains voids. This was illustrated in Case 2B. Two mechanisms have been identified as contributing to the increased shock sensitivity of porous cast propellant compared to a voidless sample of the same propellant. First, it was shown that for the same stress rate applied to the surface of the cast material, the stress waves will coalesce into a shock much sooner in porous material than in nonporous material. This is due to the

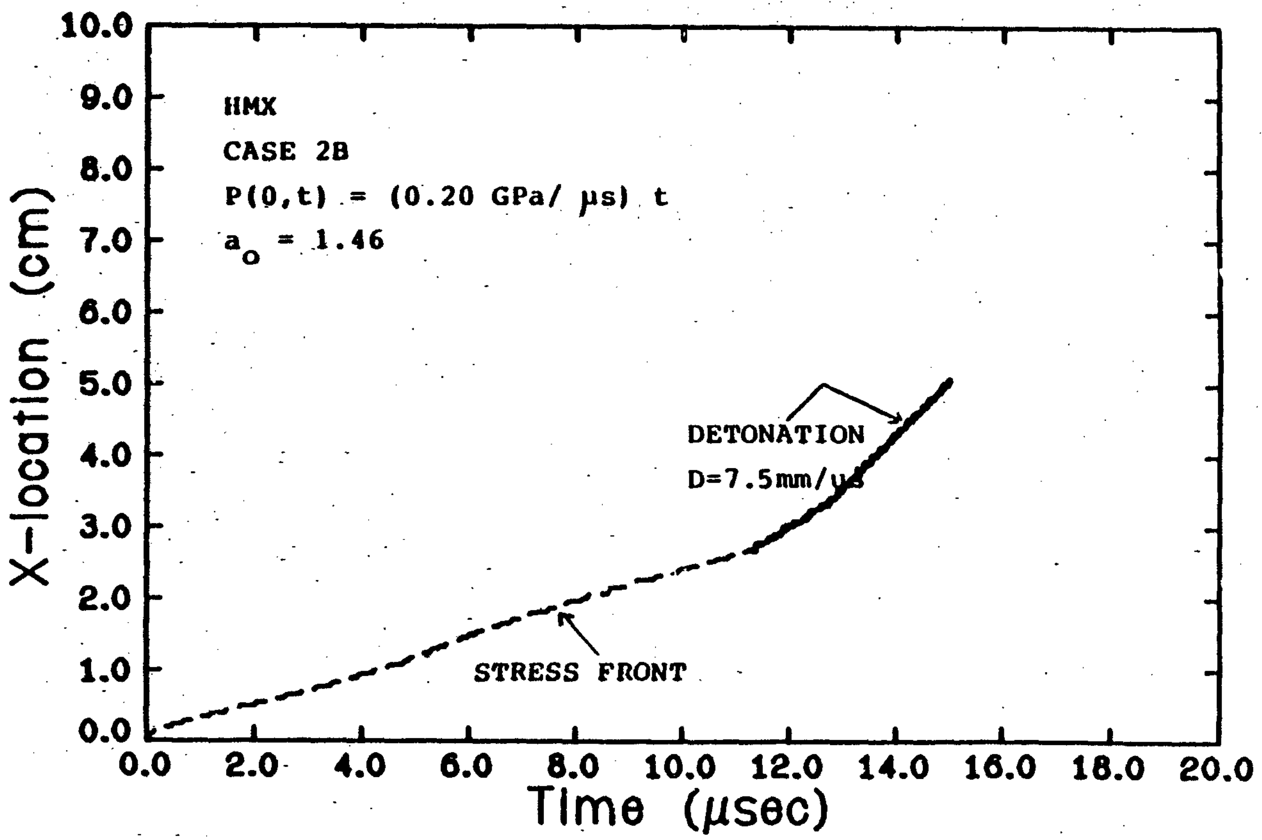

Fig. 5.16 Stress front and Detonation front (x,t) locus for Case 2B

increase in sound velocity as the porous material is consolidated. Secondly, the porous material will shock initiate at much lower shock strengths than the homogeneous material. It is theorized [51] that density irregularities in the porous material can cause shock coalescence which leads to localized areas of increased internal energy. If the localized heating is great enough to initiate solid decomposition, the result can be run-away reaction, shock strengthening, and subsequent detonation.

Again, as in the DDT-Case 1 study, the important aspect of this type of DDT analysis is the predetonation pressure buildup in the reaction zone. The rate at which the stress waves are transmitted from the burning granular bed to the porous cast material determines where and when the shock wave developes. Taken in conjunction with the propellant properties and physical dimensions of the motor, one can determine if a DDT hazard is likely.

CHAPTER 6

SUMMARY, CONCLUSIONS AND RECOMMENDATIONS

6.1 Summary of DDT

The work presented in this report has categorized three distinct ways in which high-energy solid propellant can undergo a transition from deflagrative (convective) combustion (DDT-Case 1, DDT-Case 2) or conductive combustion (DDT-Case 3) to a high-order detonation. The event referred to is called DDT (Deflagration to Detonation Transition) or DSDT (Deflagration to Shock to Detonation Transition). The terms DDT and DSDT were used interchangeabley throughout the text. The emphasis of the research presented here was on the transient events prior to the detonation as well as the steady state detonation conditions.

Chapter 1 provided a review of shock waves and detonation waves in homogeneous fluids and Chapter 2 documented some of the published work on two-phase flow, SDT (Shock to Detonation Transition), DDT, and other related topics. A mathematical description of the fluid mechanics of the DDT process was developed in Chapter 3. A major assumption made in modeling the transient, two-phase (product gas, unreacted solid) flow behavior was that each phase, by itself, is a continuum. In addition, the mass-weighted mechanical mixture of the two phases combined is also a continuum. The resulting 'separated flow' governing equations include the conservations of mass, momentum and energy for both the solid phase and the product gas phase. The gas phase and solid phase conservation equations are coupled through constitutive relations for interphase mass, momentum and energy transfer. Equations of state for both the compressible solid material and the detonation product gases were also developed. The solid phase equation of state is based on information from the unreacted shock Hugoniot and the gas phase equation of state is a modified form of the nonideal Nobel-Abel equation of state. Finally, an interphase force balance between the gas pressure, solid stress and void-dependent equilibrium stress was used to obtain closure.

In Chapter 4 a finite difference numerical technique was described which solves the resulting system of coupled, time-dependent, two-phase flow equations. A method of lines (MOL) procedure was used to solve the 'stiff' differential equations. The technique involves decoupling the space and time derivatives at each discrete point in x,t space. References cited in Chapter 4 show that the MOL is a suitable numerical technique for solving the Euler equations. Included in Chapter 4 was a short discussion on the artificial viscosity coefficient used in the finite difference form of the differential equations. The term was included to smooth small oscillations present in the numerical solution. It was also shown in Chapter 4 that the term is necessary in order to properly account for the entropy increase across shock waves.

Finally, results obtained from the numerical simulations were presented in Chapter 5 for two of the three DDT scenarios. Whenever possible, the numerical predictions for CJ properties, detonation velocity and detonation run-up length were compared with experimental data and predictions obtained from a comprehensive chemical equilibrium computer code (TIGER [62]).

The first DDT scenario (DDT-Case 1) describes the results from convective combustion in a packed bed of granulated high-energy propellant or explosive. The term 'convective combustion' is used to describe flame spreading through a granular bed of reactive material resulting from a pressure gradient driving hot gases over the surface of the unreacted particles.

Four examples (Cases 1A -1D) were shown where DDT-Case 1 did occur. In each case the process started as a slow burning convective ignition front which after a short time (20 - 50 μs) made a transition to a steady state detonation. Values predicted for the CJ properties (pressure, temperature, specific volume) and detonation velocity were in close agreement with values predicted by the chemical equilibrium computer code. Also, the ignition front (x,t) locus for one case was compared with experimental data from Price and Bernecker [75]. In that particular case, both experimental data and numerical predictions showed the detonation wave traveling at a constant detonation velocity D=7.00 mm/μs.

It should be re-emphasized at this time that a DDT of this type did not always occur. Simply having accelerating convective combustion in a confined granular bed does not imply a DDT will always occur. For example, as shown in Sec. 5.2 , a granular bed with a high initial gas porosity ($\phi_{go} > 0.55$) will not undergo a

DDT, at least within a reasonable length of less than one meter.

From the experimental data cited and the computer predictions, it appears that the initial porosity plays a key role in determining whether a DDT-Case 1 will occur. As stated above (and in Sec. 5.2), a loosely packed bed (high ϕ_{go}) generally does not provide enough confinement of the product gases in the reaction zone. On the other hand, a bed which is too tightly packed (low ϕ_{go}) restricts the flow of hot product gases over the unreacted particles. In effect, a bed which is too tightly packed terminates convective combustion, and therefore, there is a range of initial porosities over which a granular bed will DDT. If the DDT does occur, the detonation run-up distance ℓ_{CJ} is dependent on the initial porosity.

This does not imply that the initial porosity is the only initial condition which affects the outcome. Other material properties and initial conditions which were shown to be important include; initial particle size, bed length, burning rate, and bed confinement. Combined, they play a key role in controlling the pressure-rise rate in the reaction zone.

An interesting event occurred when the burning rate index was lowered to n=0.80. Instead of slowly burning through the bed as expected, the porous bed formed a solid 'plug'. The product gas pressure immediately rose to shock initiation levels (3-5 GPa) and with a specific model for hot spot formation assumed, shock initiated the consolidated material at the plug/porous propellant interface. This was a significant result since it showed that simply reducing the reaction rate did not eliminate the detonation hazard.

The DDT-Case 2 event involved a burning granular bed adjacent to porous, cast explosive. In this case the granular bed is not long enough to undergo a DDT-Case 1. However, through momentum transfer across the granular bed/ cast explosive interface, the pressure-rise rate in the granular bed stresses the cast material. It was shown that if the pressure-rise rate in the granular bed is rapid enough, it can lead to shock initiation in the cast material. This event is more likely to occur if the material is porous than if it is homogeneous.

6.2 Concluding Remarks

Much progress has been made in the study of DDT in nitramine-based solid propellants. However, it is clear that there are still many aspects of the transient events leading up to DDT that need to be explored further.

At the present time one of the most important topics which must be adressed is the concept of 'hot spot' formation in heterogeneous energetic materials. It is clear from experiments that the hot spots play a key role in making porous materials much more shock sensitive to detonation than nonporous samples. Research in this field must focus on determining the different mechanism which cause hot spots to develop and on the ensuing reaction which strengthens the shock front. Although experimental evidence has supported the notion that hot spots do exist, very little is actually known about how they are formed. Clearly, two- and three-dimensional shock interactions occuring in porous materials must also be considered.

But more importantly, much more work in shock physics should be conducted in which measurements are made of the run-up distance as a function of the burning rate, porosity, chemical energy and solid density. A better data base is also required in order to better define the interphase mass, momentum and energy transfer rates [Eqs. (3.12, 3.14, 3.16)].

APPENDIX A

DETONATION (CJ) PRESSURE ESTIMATE

The material presented in this Appendix comes from a set of lecture notes on stress wave phenomena prepared by Dr. Dennis Hayes, Sandia National Laboratories [72]. It illustrates how a simplified equation of state can be used to obtain estimates of the equilibrium detonation pressure, P_{CJ}.

Begin by assuming the detonation products at the CJ plane obey an ideal equation of state

$$Pv = gRT \tag{A.1}$$

where g represents the ratio of specific heats. For monatomic and diatomic molecules at atmospheric conditions, typically the parameter g ranges from 1.4 to 1.66. However, in treating highly compressed detonation products, g is taken to be approximately three [25].

From the First Law of Thermodynamics, Maxwell's relations and definitions for specific heat, one obtains a caloric equation of state compatible with Eq. (A.1), i.e.,

$$e = Pv/(g - 1) \tag{A.2}$$

Since the thermodynamic state of the detonation products must lie on the fully reacted Hugoniot, then

$$e = P(v_o - v)/2 + E_{ch} \qquad (A.3)$$

Equating Eqs. (A.2) and (A.3) and making use of Eq. (1.8) yields

$$P(u) = r_o (g - 1) E_{ch} + r_o (g + 1) u^2/2, \qquad (A.4)$$

where u is particle velocity. Equation (A.4) is an expression for the pressure in terms of one unknown, namely the particle velocity. Now, equating the CJ tangency condition

$$dP/du\Big|_{CJ} = P/u \qquad (A.5)$$

and Eq. (A.4) gives

$$dP/du\Big|_{\text{Eq. (A.4)}} = P/u$$

then $P_{CJ} = r_o (g + 1) u$ at the CJ point (A.6)

Equating the CJ pressure [Eq. (A.6)] to the general P(u) Hugoniot expression [Eq. (A.4)] gives

$$P_{CJ} = 2 r_o (g - 1) E_{ch} \qquad (A.7)$$

Equation (A.7) gives an approximate solution for CJ pressure assuming the initial density r_o and chemical energy release E_{ch} are known. Again, assuming g = 3.00 has been shown to be a good estimate for the artificial specific heat ratio.

As an example, consider HMX which has a crystalline density of r_o = 1.9 g/cc and a value of E_{ch} = 5.84 MJ/kg. Equation (A.7) then yields

$$P_{CJ} = 2\ (1.90\ \text{g/cc})\ (2)\ (5.84\ \text{MJ/kg})$$
$$= 44.38\ \text{GPa}$$

The TIGER equilibrium calculation gives P_{CJ} =36.57 (see Table 5.1).

APPENDIX B

FLOW CHART FOR METHOD OF LINES

The following is a step-by-step outline of the method of lines solution technique applied to the one-dimensional, two-phase flow governing equations. It is assumed that the distance-time (x,t) grid is already defined (see Fig. 4.1).

1.) Initialize all dependent variables at time t^n .

2.) Compute time step Δt^n.

3.) Compute boundary conditions ($x=0, x=L$) at time t^n.

4.) Express x-derivatives at time t^n by finite difference analogs [see Eqs. (4.5)]

5.) Compute mass, momentum and energy transfer terms at time t^n . [see Eqs. (4.6)]

6.) Advance solution to time t^{n+1} by ODE solver. [see Section 4.3]

7.) If $t^N = t^{n+1}$; stop.

8.) Set $t^n = t^{n+1}$

9.) Repeat steps 2-8 .

Boundary Conditions for DDT-Case 1

mass

$$dr_1/dt\Big|_{j=1} = -(r_1 u_g)\Big|_{j=2}/\Delta x + G\Big|_{j=1} \qquad dr_1/dt\Big|_{j=J} = -(r_1 u_g)\Big|_{j=J-1}/\Delta x + G\Big|_{j=J}$$

$$dr_2/dt\Big|_{j=1} = (r_2 u_p)\Big|_{j=2}/\Delta x - G\Big|_{j=1} \qquad dr_2/dt\Big|_{j=J} = (r_2 u_p)\Big|_{j=J-1}/\Delta x - G\Big|_{j=J}$$

momentum

$$d(r_1 u_g)/dt\Big|_{j=1} = 0 \qquad d(r_1 u_g)/dt\Big|_{j=J} = 0$$

$$d(r_2 u_p)/dt\Big|_{j=1} = 0 \qquad d(r_2 u_p)/dt\Big|_{j=J} = 0$$

<u>energy</u>

$$d(r_1 E_g)/dt\Big|_{j=1} = -(r_1 u_g E_g + P_g u_g \phi_g)\Big|_{j=2}/\Delta x + \dot{Q}_{j=1} + GE_{ch\ j=1}$$

$$d(r_1 E_g)/dt\Big|_{j=J} = -(r_1 u_g E_g + P_g u_g \phi_g)\Big|_{j=J-1}/\Delta x + \dot{Q}_{j=J} + GE_{ch\ j=J}$$

$$d(r_2 E_p)/dt\Big|_{j=1} = (r_2 u_p E_p + P_p u_p \phi_p)\Big|_{j=2}/\Delta x - \dot{Q}_{j=1}$$

$$d(r_2 E_p)/dt\Big|_{j=J} = (r_2 u_p E_p + P_p u_p \phi_p)\Big|_{j=J-1}/\Delta x - \dot{Q}_{j=J}$$

APPENDIX C

HOT SPOT DECOMPOSITION

Shock to detonation transition (SDT) in a porous reactive material is a complex process. For simplicity, one can describe the SDT as three independent events. First, the shock wave compresses the reactive material, raising the bulk temperature T. At the same time, a small fraction [Eq. (2.5)] of the shocked material is heated to a 'hot spot' temperature T_H. In our model T_H is calculated assuming a partition of energy based on the volume fraction of voids prior to shock heating [Eq. (2.4)]. Following the shock compression, the hot spots decompose over a delay time t^*. The final step is decomposition of the bulk solid.

This appendix has been included to clarify Step 2, hot spot decomposition. For simplicity, the hot spot decomposition is modeled using first order Arrhenius kinetics. This is given as,

$$dW/dt = -Z\ W \exp(-E^*/\hat{R}T_H) \tag{C.1}$$

where E^* is the activation energy, W is the mass fraction of unreacted explosive, Z is the frequency factor, $\hat{R}$ is the universal gas constant, and T_H is the hot spot temperature.

No known experimental data exists for the shock initiated decomposition of porous HMX. However, Hayes [29] has performed experiments using a similar porous explosive, HNS. Figure C.1 is taken directly from Hayes [29]. It shows the delay time t^* plotted as a function of the hot spot temperature T_H . Also shown in Fig. C.1 are calculated delay times assuming extrapolated low temperature Arrhenius kinetics (straight line), for which Hayes [29] used an activation temperature of T^*=15300 K and a frequency factor Z=0.153 x 10^{10} s^{-1} [79]. As shown in the figure, the measured delay times are considerably lower than those calculated using Arrhenius kinetics. In fact, if an attempt is made to fit the observed delay times with a thermal explosion model, hot spot temperatures far in excess of those calculated by Eq. (2.4) would have to be assumed. In addition, the experimental data also shows that for a hot spot temperature of 561 K, no decomposition occurred, but decomposition did occur for T =619 K.

Using the assumption of low temperature kinetics in the DDT code caused unrealistically slow reaction rates. For example, hot spot temperatures as high as 1132 K (for a_o= 1.2667) were not initiating reaction in the DDT code. It was therefore decided to fit the hot spot decomposition model used in the DDT code directly to Hayes' experimental data. This data represents the most reliable information available. The delay-time curve in Fig. C.1 was found to be a parabolic function of hot spot temperature

$$\log(t^*) = -0.6744\ (1000/T_H)\ + 2.2482\ (1000/T_H)\ -1.9132 \qquad \text{(C.2)}$$

where t^* is in μs, and T_H is in K . A temperature of 600 K was arbitrarily chosen as a lower limit at which to apply this new model. That is, we are assuming no decomposition will occur until the hot spot temperature reaches 600 K. This is again consistent with the reported data. Using the delay time calculated from Eq. (C.2), the apparent activation temperature is calculated using Eq. (C.1).

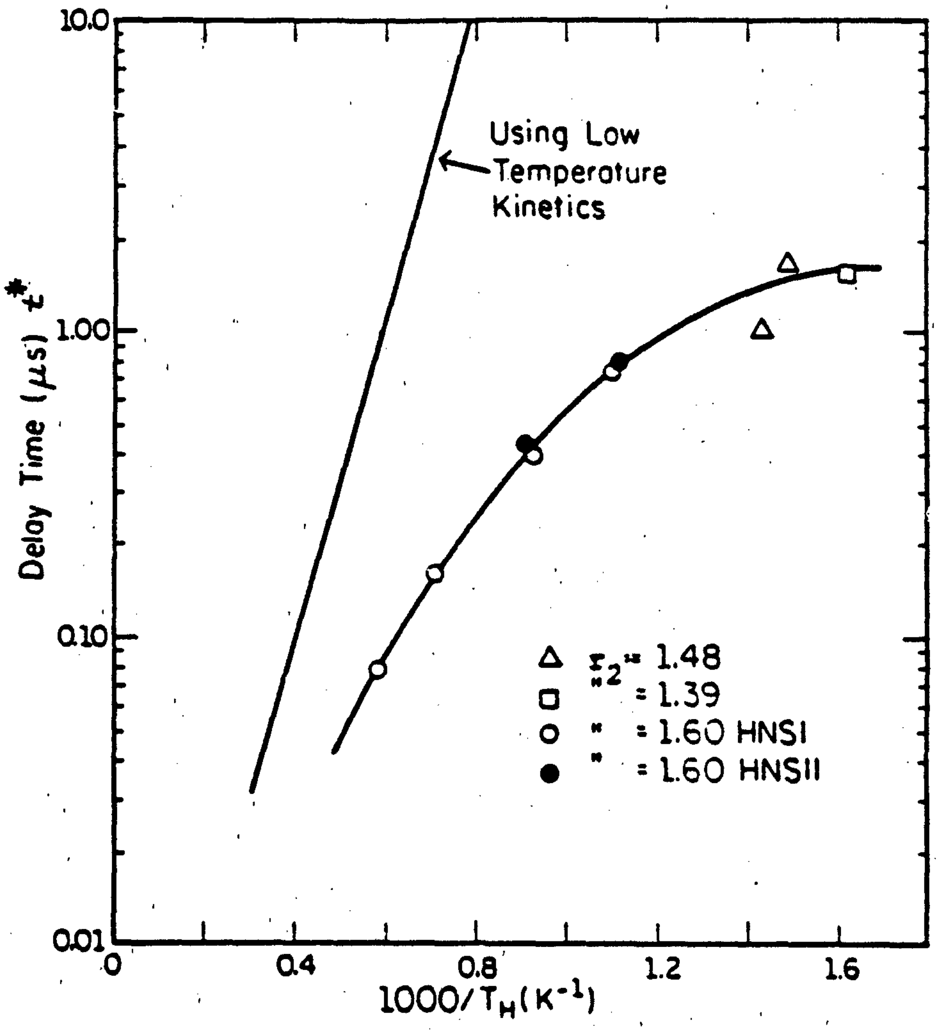

Fig. c.1 Hot spot decomposition times assuming Arrhenius kinetics and from experimental data.

REFERENCES

1.) Butler, P. B., M. L. Lembeck, and H. Krier, "Modeling of Shock Development and Transition to Detonation Initiated by Burning in Porous Propellant Beds," Combustion and Flame 46, (1982).

2.) Sutton, G. P., and D. M. Ross, Rocket Propulsion Elements, John Wiley and Sons, New York, (1976).

3.) Setchell, R. E., "Effects of Precursor Waves in Shock Initiation of Granular Explosives," Combustion and Flame 54, (1983), 171-182.

4.) Campbell, A. W., "Deflagration-To-Detonation Transition in Granular HMX," Seventh Symposium on (Intl.) Detonation, Annapolis, MD, (1981).

5.) Dick, J. J., "Measurement of the Shock Initiation Sensitivity of Low Density HMX," Combustion and Flame 54, (1983), 121-129.

6.) Bernecker, R. R., H. Sandusky, A. Clairmont, "Deflagration to Detonation Transition Studies of Porous Explosive Charges in Plastic Tubes," Seventh Symposium (Intl.) on Detonation, Annapolis, MD, (1981), 119-138.

7.) Price, D., and R. R. Bernecker, "Sensitivity of Porous Explosives to Transition from Deflagration to Detonation," Combustion and Flame 25, (1975), 91-100.

8.) Bernecker, R. R. and D. Price, "Studies in the Transition from Deflagration to Detonation in Granular Explosives. II. Transitional Characteristics and Mechanisms Observed in 91/9 RDX/wax," Combustion and Flame 22, (1974), 119-129.

9.) Boggs, T. L., C. F. Price, A. I. Atwood, D. E. Zunn, and R. L. Derr, "Role of Gas Phase Reactions in Deflagration to Detonation Transition," Seventh Symposium (Intl.) on Detonation, Annapolis, MD, (1981), 216-224.

10.) Van Tassel, W. F. and H. Krier, "Combustion and Flame Spreading Phenomena in Gas-Permeable Explosive Materials," International Journal of Heat and Mass Transfer 18, (1975), 1377-1386.

11.) Butler, P. B., and H. Krier, "Analysis of Deflagration to Shock to Detonation Transition (DSDT) in Porous Energetic Solid Propellants," AGARD Conference Preprint No. 367, paper No. 5, Lisse, The Netherlands, (1984).

12.) Hoffman, S. J., and H. Krier, "Fluid Mechanics of Deflagration to Detonation Transition in Porous Explosives and Propellants," AIAA Journal 19, (1981).

13.) Krier, H., P. B. Butler, and M. F. Lembeck, "Fluid Dynamics of the Unsteady Two-Phase Processes Leading to Detonation," Proc., 1980 JANNAF Propulsion Systems Hazards Meeting, CPIA Publication No. 330, (1980), 131-145.

14.) Cudak, C. A., H. Krier, and P. B. Butler, "Transition to Detonation from Rapid-Compression (Ramp-Waves) Generated in a Burning Porous Bed," 1984 JANNAF Propulsion Systems Hazards Meeting, CPIA Publication, (1984).

15.) Baer, M. R., and J. W. Nunziato, "A Theory for Deflagration-to-Detonation Transition (DDT) in Granular Explosives," SAND Report, SAND82-0293, (1983).

16.) Baer, M. R., J. W. Nunziato, and R. J. Gross, "A DDT Model for CP," Sandia National Laboratories Report, (1982).

17.) Boggs, T. L., C. F. Price, and R. L. Derr, "Transient Combustion: An Important Consideration in Deflagration-to-Detonation Transition," AGARD Conference Preprint No. 367, Paper No. 12, Lisse, The Netherlands, (1984).

18.) Private Communication with Dr. R. Bernecker, Naval Surface Weapons Center, White Oak, MD.

19.) Kuo, K. K., M. Summerfield, "High speed combustion of mobile granular solid propellants: Wave structure and the equivalent Rankine-Hugoniot relation," Fifteenth Symposium (Intl.) on Combustion, The Combustion Institute, Pittsburgh, PA, 515-525, (1974).

20.) Gough, P. S., and F. J. Zwarts, "Theoretical model for ignition of gun propellant", Report SRC-R-67, Final Report, Part II, Space Research Corporation, North Troy, Vermont, (1972).

21.) Kuo, K. K., and M. Summerfield, "Theory of Steady State Burning of Gas-Permeable Propellants," AIAA Journal 12, No. 1, (1974), 49-56.

22.) Bernecker, R. R., "The DDT Process for High Energy Propellants," AGARD Conference Preprint No. 367, Paper No. 14, Lisse, The Netherlands, (1984).

23.) Macek, A., "Transition from Deflagration to Detonation," J. Chem. Phys. 31, (1959), 162-167.

24.) Butler, P. B., "Shock Development and Transition to Detonation Initiated by Burning in Porous Propellant Beds," Masters Thesis, University of Illinois, Urbana, Illinois, (1981).

25.) Fickett, W., and W. C. Davis, Detonation , University of California Press, (1979).

26.) Shapiro, A., H., The Dynamics and Thermodynamics of Compressible Fluid Flow ,Volume 1, The Ronald Press Company, New York, (1954).

27.) Zel'dovich, Ta. B., and Yu. P. Raizer, Physics of Shock Waves and High Temperature Hydrodynamic Phenomena , Academic Press, New York and London (1966).

28.) Coyne, D. W., P. B. Butler, and H. Krier, "Shock Development From Compression Waves Due to Confined Burning in Porous Solid Propellants and Explosives," AIAA Paper No. 83-0480, Reno, Nevada, (1983).

29.) Hayes, D. B., "Shock Induced Hot-Spot Formation and Subsequent Decomposition in Granular, Porous, Hexanitrostiblene Explosive," Detonation Physics Symposium, Minsk, Russia, (1981).

30.) Howe, P., R. Frey, B. Taylor, and V. Boyle, "Shock Initiation and the Critical Energy Concept," Sixth Symposium (Intl.) on Detonation, Coronado, CA, August 24-27, (1976).

31.) Griffiths, N., and J. M. Groocock, "The burning to detonation of solid explosives," J. Chem. Soc. , 4145, (1960).

32.) Bernecker, R. R., and D. Price, "Studies in the Transition from Deflagration to Detonation in Granular Explosives-I Experimental Arrangement and Behavior of Explosives Which Fail to Exhibit Detonation," Combustion and Flame 22, (1974), 111.

33.) Bernecker, R. R., D. Price, J. O. Erkman, and A. R. Clairmont, "Deflagration to Detonation Transition Behavior in Tetryl," Sixth Symposium (Intl.) on Detonation, White Oak, MD, (1976), 426-437.

34.) Bernecker, R. R., H. W. Sandusky, and A. R. Clairmont, "Deflagration to Detonation Transition Studies of Porous Explosive Charges in Plastic Tubes," Seventh Symposium (Intl.) on Detonation, Annapolis, MD, (1981) 119-138.

35.) Sulimov, A. A., B. S. Ermolaev, A. A. Borisov, E. I. Korotkov, B. A. Khasainov, and V. E. Khrapovsky, "On the Mechanism of Deflagration to Detonation Transition in Gas-Permeable High Explosive," Sixth Symposium (Intl.) on Detonation, White Oak, MD, (1976), 250-257.

36.) Korotkov, A. I., A. A. Sulimov, A. V. Obmenin, V. G. Dubovitskii, and A. I. Kurkin, "Transition from Combustion to Detonation in Porous Explosives," Combustion, Explosion, and Shock Waves , 5, (1969), 317.

37.) Ramsay, J. B.,and A. Popaloto, "Analysis of Shock Wave and Initiation Data for Solid Explosives," Fourth Symposium (Intl.) on Detonation, (1965).

38.) Krier, H. and Kezerle, J. A., "A Separated Two-Phase Flow Analysis to Study Deflagration-to-Detonation Transition (DDT) in Granulated Propellant," Seventeenth Symposium (Intl.) on Combustion , The Combustion Institute, Pittsburgh, PA, (1979).

39.) Krier, H. And Gokhale, S. S., "Modeling of Convective Mode Combustion Through Granulated Propellant to Predict Detonation Transition," AIAA Journal 16 (2), (1978), 177.

40.) Pilcher, D. T., M. W. Beckstead, L. W. Christensen, and A. J. King. "A Comparison of Model Predictions and Experimental Results of DDT Tests," Sixth Symposium on Detonation, White Oak, MD, August 22-27, (1976), 258-266.

41.) Key, S. W., Sandia Laboratories, Albuquerque, NM, "HONDO-A Finite Element Computer Program for the Large Deformation Dynamic Response of Axisymmetric Solids," (1972), SLA-72-0039.

42.) Kooker, D. E., and R. D. Anderson, "A Mechanism for the Burning Rate of High Density, Porous, Energetic Materials," Seventh Symposium (Intl.) on Detonation, Annapolis, MD, June 16-19, (1981).

43.) Forest, C. A., "Burning and Detonation," Seventh Symposium (Intl.) on Detonation, Annapolis, MD, June 16-19, (1981).

44.) Tarver, C. M., T. C. Goodale, R. Shaw, and M. Copperthwaite, "Deflagration-to-Detonation Transition Studies for Two Potential Isomeric Cast Primary Explosives," Sixth Symposium (Intl.) on Detonation, Coronado, CA, August 24-27, (1976).

45.) Jacobs, S. J., comment in Sixth Symposium (Intl.) on Detonation, p249.

46.) Walker, F. E., and R. J. Wolsey, Explosivstoffe , 17, No. 1, (1969).

47.) Walker, F. E., Discussion on Shock Initiation and P-squared - t, Sixth Symposium (Intl.) on Detonation, White Oak, MD, (1976), 82-84.

48.) Cowperthwaite, M., Discussion on Shock Initiation and P-squared - t, Sixth Symposium (Intl.) on Detonation, White Oak, MD, (1976), 84-85.

49.) Frey, R., and P. Howe, Discussion on Shock Initiation and P-squared - t, Sixth Symposium (Intl.) on Detonation, White Oak, MD, (1976), 85-87.

50.) Bowden, F. P., and A. D. Yoffe, Initiation and Growth of Explosions in Liquids and Solids , Cambridge University Press, (1952).

51.) Mader, C. L., Numerical Modeling of Detonations , University of California Press, Berkeley, (1979).

52.) Wallis, G., One-Dimensional Two-Phase Flow , McGraw-Hill, New York, (1969).

53.) Nunziato, J. W., and E. K. Walsh, "On Ideal Multiphase Mixtures with Chemical Reactions and Diffusion," Arch. Rational Mech. Anal. 73, (1980).

54.) Truesdell, C., Rational Thermodynamics , McGraw-Hill, New York, (1969).

55.) LASL Shock Hugoniot Data , edited by S. P. Marsh, University of California Press, Berkeley, (1980).

56.) Hyman, J. M., "A Method of Lines Approach to the Numerical Solution of Conservation Laws," Los Alamos Report, LA-UR 79-837, (1979).

57.) Chao, B. T., W. T. Sha, and S. L. Soo, "On Inertial Coupling in Dynamic Equations of Components in a Mixture", International Journal of Multiphase Flow 4, (1978), 219-223.

58.) Crowe, C. T., "On Soo's Equations for the One-Dimensional Motion of Single-Component Two-Phase Flows," International Journal of Multiphase Flow 4, (1978), 225-229.

59.) Kuo, K. K., and C. C. Nydegger, "Cold Flow Resistance Measurement and Correlation in a Packed Bed of WC-870 Spherical Propellants," Journal of Ballistics 2, (1978).

60.) Denton, W. H., "The Heat Transfer and Flow Resistance for Fluid Flow Through Randomly Packed Spheres," ASME Transactions , (1951), 351.

61.) Johnson, J. N., Hayes, D. B., and J. R. Asay, "Equations of State and Shock-Induced Transformations in Solid 1-Solid 2-Liquid Bismuth," J. Phys. Chem. Solids 35, (1974), 501-515.

62.) Coperthwaite, M., and W. H. Zwisler, "TIGER' Computer Code Documentation," Report PYV - 1281, Stanford Research Institute, (1974).

63.) Goodman, M. A., and S. C. Cowin, "A Contiunnm Theory for Granular Materials," Arch. Ratinal. Mech. Anal. 44, (1971), 249-266.

64.) Carroll, M. M., and A. C. Holt, "Static and Dynamic Pore-Collapse Relations for Ductile Porous Materials," Journal of Applied Physics 43, (1972), 1623-1635.

65.) Herrman, W., "Constitutive Equation for the Dynamic Compaction of Ductile Porous Materials," Sandia Report, SC-R-69-1185, (1969).

66.) Gear, C. W., Numerical Initial Value Problems in Ordinary Differential Equations , Prentice - Hall, Englewood Cliffs, New Jersey, (1971).

67.) Forsythe, G. E., M. A. Malcolm, and C. B. Moler, Computer Methods for Mathematical Computations . Prentice - Hall, New Jersey, (1977).

68.) UOILIB Computer Library, University of Illinois, Urbana, Illinois, 1984.

69.) IMSL Math Library, University of Illinois, Urbana, Illinois, 1984.

70.) Sod, G. A., "A Survey of Several Finite Difference Methods for Systems of Nonlinear Hyperbolic Conservation Laws," Journal of Computational Physics 27, (1978), 1-31.

71.) VonNeumann, J., and R. D. Richtmyer, "A Method for the Numerical Calculation of Hydrodynamic Shocks," Journal of Applied Physics 21, (1950), 232-237.

72.) Hayes, D. B., "Stress Wave Phenomena in Condensed Media," Lecture notes prepared at Sandia National Laboratories.

73.) Dobratz, B. M., "Properties of Chemical Explosives and Explosive Stimulants," Lawrence Livermore Laboratory Report, UCRL - 51315 Rev. 1, (1974).

74.) U.S. Army Engineering Design Handbook, "Principles of Explosive Behavior," AMC Pamphlet, AMCP 706-180, (1972).

75.) Price, D., and R. R. Bernecker, "Effect of Wax on the Deflagration to Detonation Transition of Porous Explosives," Behavior of Dense Media Under High Dynamic Pressures , Commissariat a l'Energie Atomique, Paris, (1978).

76.) Johansson, C. H., and P. A. Persson, Detonics of High Explosives , Academic Press, London, (1970).